5-1997

Geochemical, Petrologic, and Structural Characterization at Multiple Scales of Deformation Associated with the Punchbowl Fault, Southern California

Steven E. Schulz
Utah State University

GEOCHEMICAL, PETROLOGIC, AND STRUCTURAL CHARACTERIZATION AT MULTIPLE SCALES OF DEFORMATION ASSOCIATED WITH THE PUNCHBOWL FAULT, SOUTHERN CALIFORNIA

by

Steven E. Schulz

A thesis submitted in partial fulfillment
of the requirements for the degree

of

MASTER OF SCIENCE

in

Geology

Approved:

UTAH STATE UNIVERSITY
Logan, Utah

1997

ABSTRACT

Geochemical, Petrologic, and Structural Characterization at Multiple Scales of Deformation Associated with the Punchbowl Fault, Southern California

by

Steven E. Schulz, Master of Science

Utah State University, 1997

Major Professor: James P. Evans
Department: Geology

Three traverses across the exhumed trace of the Punchbowl fault zone in the Pelona Schist, southern California, were examined at the millimeter to kilometer scales to determine the morphology, deformation mechanisms, and geochemistry of the fault zone in schistose rocks. The Pelona Schist is predominantly a quartz-albite-muscovite-actinolite schist with associated minor metabasalts. The Punchbowl fault zone, which is exhumed 2-4 km, has 44 km of right lateral slip, and is composed of a fault core enveloped by a damaged zone.

The fault core is a region of extreme slip localization that records most fault displacement. Deformation in the fault core is dominated by grain-size reduction accompanied by fluid-dominated alteration, in contrast to the damage zone, where deformation is dominated by brittle and semi-brittle fracturing, cataclasis, and slip. Portions of the Punchbowl fault have multiple fault cores, with each fault core less than 10 cm thick. The thickness of a fault depends upon the type of deformation measured and the scale of observation. Mesoscopic fractures begin 50 m from the fault core, whereas the onset of

fault-related microfractures occurs at approximately 40 m from the fault core. A geochemical signature based on whole-rock geochemistry suggests a fault thickness of less than 10 m. Grain-size reduction occurs over a 10 m thick region and mineralogic changes occur over a region 20-30 m thick. Reorientation of preexisting foliation occurs over a zone 30 m thick.

Fault-core morphology and textures are similar to those in the Punchbowl fault to the northwest, where it displaces sedimentary rocks, and the San Gabriel fault, which formed in crystalline rocks. This suggests that the processes that form foliated, fine-grained, cataclasite-dominated fault cores of large displacement faults are similar for diverse lithologies. The composition of the fault core is variable along strike, with little geochemical or mineralogical homogenization. Whereas processes that form fault cores are similar, localized interaction of fluids caused compositional variability within the core. Changes in fault composition and fluid-rock interactions may result in different fault properties and behaviors.

(164 pages)

Dedicated to

Kayleigh

ACKNOWLEDGMENTS

First and foremost, I would like to thank my advisor, James P. Evans. Jim provided the psychological, mental, and financial support that I needed to complete this thesis. His constant guidance and encouragement saw me through the darkest days of thesis writing and prevented me from procrastinating more than I did. He was very willing to help me out whenever it was required, but allowed me the freedom to express my own ideas. A graduate student could not ask for a better advisor. Jim's expertise added much to this thesis; however, I take full responsibility for all inaccuracies.

Research for this thesis was made possible by grants from the U. S. Geological Survey National Earthquake Hazard Reduction Program (Grant #1434-92-G-2184) and the National Science Foundation (Grant EAR# 9205774) awarded to Dr. J. P. Evans.

I would especially like to thank my wife, Paula Breighton, who waited patiently (usually) while I was living in Utah attempting to finish this work. Paula gave me the encouragement to continue and her confidence in me inspired an attempt to look beyond what I had thought possible.

My parents provided me with moral support throughout the long years as a graduate student. They gave me a strong work ethic, which I often chose to ignore, and always led me to believe that anything was possible, if only I would get my hair cut.

Caleb Pollock, who came along as my field assistant, also deserves quite a bit of credit. It was he who kept me on the track and provided the critical comments that kept me from jumping to far too many conclusions. He also cooks a mean pot of chili.

My committee members, Susanne Janecke and Donald Fiesinger, provided good insight and helped me to organize my thoughts and express myself in a clearer, more concise manner. They never lost faith, even when it seemed I would never finish. I

would also like to thank the professors and staff at the Geology Department of Utah State University. The department was always supportive and friendly, and I could not think of a better atmosphere in which to study.

I would also like to thank Drs. Peter Kolasar at the Geology Department, Utah State University, and William Perry at the Department of Geology and Geophysics, University of Utah, for their assistance with the x-ray diffraction. William McManus and Gary Pederson at the Electron Microscopy Facility, Department of Biology, Utah State University, were generous with their assistance and allowed me access to their scanning electron microscope.

Without the friendship and support of many people, I would not have been able to complete this work and still retain my sanity. It is these friends who listened; they tolerated my strange hours and provided me with a sounding board for all of the crazy ideas that I had. Special thanks goes to my roommates, John Mayers, Caleb Thompson, and Michael Coffin, for constant encouragement, assistance with my thesis, and Total Carnage. "They're Everywhere!" The other graduate students at Utah State University also deserve my appreciation, with special thanks to my officemates, who somehow managed to put up with me without resorting to violence.

There are many other people who deserve my thanks, too many to list individually. They gave me constant encouragement and did not let me convince myself that I was never going to finish.

Steven Schulz

CONTENTS

Page

LIST OF TABLES

Table

LIST OF FIGURES

INTRODUCTION

The mechanics and mechanisms of fault zones, especially at depth, are not yet well understood (Hickman, 1991). The processes that are involved during slip of large displacement faults are the topic of much discussion in the structural geology and rock mechanics communities. Fault-zone morphology, and how it influences earthquake wave propagation, is not well understood either, especially at seismogenic depths (e.g., Sibson, 1989). This study examines the Punchbowl fault, an exhumed large-displacement fault in southern California, in order to better understand the physical and chemical characteristics of large-displacement faults and the processes that occur along them.

There is an increasing amount of evidence that some fault zones are weak and slip is produced by low values of shear stress (τ) (Hickman, 1991). Recent studies of the San Andreas fault, including in situ stress measurements, show that the maximum principal stress ($\sigma 1$) direction is close to perpendicular to the fault, and that shear stress is low (Zoback et al., 1980; Mount and Suppe, 1987; Zoback et al., 1987; Jones, 1988). This is contrary to Andersonian fault mechanics, which predicts that a fault will be oriented approximately 30° from the maximum principal stress direction (Anderson, 1951).

Extensive heat-flow measurements made near the San Andreas fault zone, which indicate no significant heat flow anomaly across the fault zone, also suggest a low shear stress (roughly 10-30 MPa) (Brune et al., 1969; Henyey and Wasserburg, 1971; Lachenbruch and Sass, 1980, 1988; Sylvester, 1988). These measurements show little evidence of frictional heating along the fault, and along with the low shear stress, require a weak fault with a coefficient of friction (μ) of less than 0.15 (Turcotte et al., 1980; Sylvester, 1988). Such a low coefficient of friction is incompatible with data from Byerlee (1978), who showed in laboratory experiments that faults have a coeffi-

cient of friction of roughly 0.85. These observations show that the processes operating in fault zones are poorly understood.

Altogether, these data show that the San Andreas fault is weak, not only in an absolute sense, as indicated by the low shear stress, but in a relative sense, with the fault being much weaker than the surrounding crustal rocks (Rice, 1992). This weakness may be due to several factors, such as inherently weak materials in the fault, dynamic weakening processes, or the presence of pore fluids in the fault during rupture.

Montmorillonite has been suggested as a possible candidate to explain the weakness of the San Andreas fault. However, montmorillonite has a μ (0.2-0.3) that is too high to produce the low shear stress on the fault (Byerlee, 1990). Also, montmorillonite is a water-bearing clay that would dewater at temperatures above 200° C, causing frictional strengthening (Rice, 1992). The amount of clay present in fault gouge of large-displacement faults is variable along strike, with some portions showing only small amounts (Anderson et al., 1980; Chester et al., 1993). Chrysotile, a serpentine mineral, may be present in many of the aseismic regions of the San Andreas fault (Moore et al., 1996). A chrysotile-rich gouge can have a coefficient of friction that approaches 0.1 for pressures and temperatures found in the upper 3 km of the fault (Moore et al., 1996). At greater depths, chrysotile is too strong to account for the weak fault.

Fault zones form due to the localization of deformation (Sibson, 1977). With increasing displacement along a fault, the strength of the fault rock may stay constant, or decrease. It is possible that over time, the frictional strength of fault rocks would weaken considerably due to continued slip; however, this is unlikely (O'Neil and Hanks, 1980). It seems that the presence of weak materials is insufficient to fully account for the weak nature of the San Andreas fault.

A dynamic weakening process may occur on the fault during slip, strengthening again after movement has ceased (Heaton, 1990). A dynamic weakening process occurs when the fault strength is reduced during slip by mechanisms such as frictional melting and lubrication, or thermal pressurization of pore fluids. Another mechanism for weakening along the fault is based on the assumption that there are severe stress concentrations at the edges of locked regions in the fault zone (Rice, 1992). If these regions slip-weaken rapidly after an earthquake begins, the stress drops would be much smaller than if there were no stress concentrations. Although these processes may be likely, it is difficult to determine from field observations which, if any, of these dynamic weakening processes operated. As yet there is no direct evidence for dynamic weakening processes along the San Andreas fault, and it is not clear which textures and characteristics indicate the presence of these mechanisms (Evans and Chester, 1995).

The presence of fluids within the fault zone may also help to explain the characteristics of the San Andreas fault (Byerlee, 1993; Chester et al., 1993; Rice, 1992). Elevated pore pressure within the fault zone would allow for low shear stress with materials that have normal friction properties of $\mu = 0.6\text{-}0.9$ (Rice, 1992). Fault zones often act as conduits for water migration, with a heat source inducing convection currents (O'Neil and Hanks, 1980). Water in the upper crust near the San Andreas fault has been documented as deep as 8-10 km (O'Neil and Hanks, 1980), which is within the seismogenic regime of the San Andreas fault (Sibson, 1989). O'Neil and Hanks (1980) found that the stable isotope signatures of rocks located near the San Andreas fault have been altered by low-temperature interaction with groundwater. The rocks located farther from the fault have not been similarly altered, suggesting that the circulation of water was controlled by the fault.

The pore-pressure of fluids trapped within a fault zone will increase as stress on the fault accumulates (Rice, 1992; Chester et al., 1993). An elevated pore-pressure will enable fault slip with relatively low shear stress. This would, however, require a pore-pressure greater than lithostatic or least principal stress, which should cause the surrounding rock to fracture (Rice, 1992), allowing the water to escape and lowering the pore-pressure. Two models have been proposed for maintaining high pore-pressures without fracturing the surrounding rock. Byerlee (1990) stated that a low water-clay ratio within the fault gouge may allow the pressure of water trapped within very small pockets to reach the lithostatic pressure without failure. Rice (1992) proposed that the weak material of the fault will develop a stress state that is different from the stress state in the nearby crust, allowing the pore-pressure to be lower than the least principal stress within the fault zone, yet be high enough to weaken the fault.

Pore fluids may also contribute to fault weakness by inducing nonfrictional processes, such as solution-transport mechanisms (Hickman, 1991). Processes such as transformation-enhanced weakening (Janecke and Evans, 1988; Knipe, 1989), solution creep (Hickman, 1991), fluid-assisted mineral reactions, and crack healing (Zoback and Hickman, 1996) may also weaken the fault. Blanpied et al. (1992) showed that solution weakening produced in laboratory experiments has a definite weakening effect upon the rocks. Although difficult to determine, field data may show evidence of these processes as well (Rutter, 1983; Hippler and Knipe, 1989; Chester et al., 1993). How these mechanisms influence the mineralogy, microstructures, and physical properties of fault-zone materials is unclear, especially at seismogenic depths (Zoback and Hickman, 1996). The importance of these solution processes in faulting, as well as how these reactions may change with different slip rates, is also unknown.

How fault morphology influences slip is not understood either, especially at intermediate depths, from 5 to 15 km. The generation and propagation of earthquake ruptures are affected by the internal structures of the fault (Feng and McEvilly, 1983; Bruhn, 1994). Byerlee (1990) suggested that faults thicken into shear zones with depth. However, recent work (Chester et al., 1993; Chester, 1995; Evans and Chester, 1995) suggests that at depths of approximately 4 km, major faults of the San Andreas fault system are limited to thin, discrete slip surfaces. There may be multiple anastomosing slip surfaces that are confined to a relatively thin zone, outside of which there is little to no fault-related deformation (Chester et al., 1993). Anderson et al. (1983) suggested that faults are thick near the surface, but narrow at deeper, uppercrustal levels. These narrow faults would consist of thin cataclastic rocks, formed in a brittle regime. At greater depths, the faults enter the ductile zone and would again thicken.

The internal structures of faults will affect fluid migration and stress distribution within the fault. Various portions of a fault can either impede or enhance fluid migration through or along a fault zone. Understanding the characteristics of a fault zone will allow for better prediction of processes in groundwater, hydrocarbon, and hydrothermal systems.

The San Gabriel Mountains, located north of the Los Angeles Basin in southern California, have at least two exhumed strike-slip faults of the San Andreas fault system. Both the San Gabriel fault and the Punchbowl fault are ancient traces of the San Andreas fault that have been uplifted by the formation of the mountain range. These two faults provide an opportunity to study fault zones that were formed and active at depths of at least 4 km.

The goals of this study were to determine the physical, chemical, and mineralog-

ic characteristics of the Punchbowl fault in metamorphic rocks. The Punchbowl fault provides data on a large-displacement fault near the top of the seismogenic zone. The spatial variability of these characteristics, both along strike and across the fault zone, will be examined in order to better understand the processes that occur within a fault during seismicity. This study also investigates the effects of lithology on the development and characteristics of a large displacement fault.

To accomplish these goals, the Punchbowl fault was examined at multiple scales from mesoscopic (outcrop) to microscopic (petrographic and scanning electron microscopes). The spatial variability of various deformation structures, such as fractures, veins, and small faults, were documented across the fault zone. These data provide insight into the thickness of the fault zone, the spatial distribution of various structural elements in the fault, and the distribution of slip within the fault zone. The geochemical and mineralogical variations within the fault zone were also evaluated. These variations will show how fluids interact with the rocks of the fault zone and their effect on the formation and subsequent slip of this large-displacement fault.

The San Andreas Fault Zone Drilling Project, proposed to be sponsored by the National Science Foundation, is being undertaken to understand more about how faults work by drilling into the fault zone to depths of 5-10 km (Zoback and Hickman, 1996). Three main components of the study are being planned, including sampling the fault-zone material and fluids, running downhole and surface-to-borehole geophysics, and monitoring the microseismicity and interseismic fault zone processes. The project proposes to drill a shaft near the San Andreas fault in Parkfield, California, where the San Andreas fault juxtaposes Tertiary marine sediments overlying granitic basement against the Franciscan melange (Zoback and Hickman, 1996). From this shaft, angled holes

will be drilled to intersect the fault and hopefully remove continuous core from the entire fault zone. The mineralogy and deformation microstructures will be examined to determine the composition of fault rocks, determine the dominant deformation mechanisms, and assess the effects of fluid-rock interaction.

Examining the Punchbowl fault will provide an early understanding of what the drilling project may encounter in the San Andreas fault. The Punchbowl fault zone is an analog to the San Andreas fault, as both of these faults were formed at similar depths and cut metamorphic rocks. The type and spatial distribution of macroscopic and microscopic structures associated with the Punchbowl fault offer an indication of the fault-zone characteristics that will be found and provide clues to potential difficulties.

An overview of the general structures and geometries of fault zones is presented, followed by a brief review of previous studies that examine large-displacement strike-slip faults in the San Gabriel Mountains. This is followed by a general overview of the San Gabriel Mountain geology, with emphasis on the study region.

The data collected in this study are separated into several sections based on the scale of the observations. First, the mesoscopic-, or outcrop-scale characteristics of the Punchbowl fault are examined, after which the microscopic characteristics of the fault-zone are described. The microscopic analysis was performed using both a petrographic and a scanning electron microscope. The geochemical and mineralogical variation across the fault zone are then discussed. A comparison between previous work and this study is given in the discussion section, which is then followed by conclusions.

FAULT ZONE STRUCTURE

On the mesoscopic scale, a fault zone is defined as the portion of the surrounding host rock that shows a greater intensity of brittle deformation than is typically present (Chester and Logan, 1986). Faults can be divided into three distinct zones: the fault core, the damaged zone, and the relatively undeformed protolith or host rock (Fig. 1; Chester et al., 1993). The fault core is usually composed of gouge or cataclasite, and may contain a central ultracataclasite layer surrounded by a foliated zone (Chester et al., 1993; Caine et al., 1996). No scalar relationship is implied between the components of a fault zone. The relative shapes and sizes of each of these structural components will vary from fault to fault and within a fault system, and it is not necessary to have each component present in any given fault zone. Figure 2 is a conceptualization of how these components may vary along strike and down dip in a fault. The thickness of each structural zone can vary both along strike and down dip, and there may be multiple, and

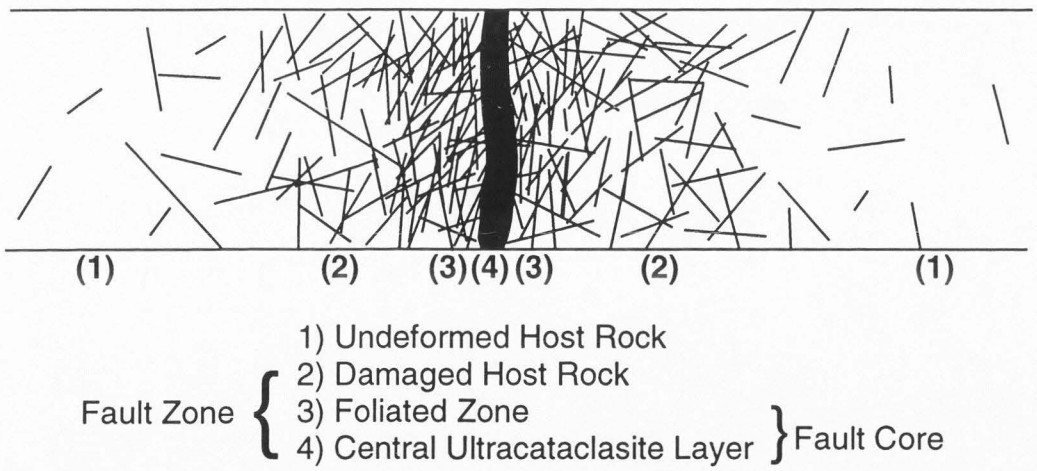

Fig. 1 Illustration of the spatial position of various structural zones that may comprise a fault (after Chester et al., 1993). Drawing is not meant to imply any scale. Boundaries between zones may vary from sharp to gradational (Caine et al., 1996).

often anastomosing, fault cores (Chester and Logan, 1987; Chester et al., 1993; Evans and Chester, 1995; Caine et al., 1996). In this study, the rocks located between strands of the fault core will be referred to as the 'intrafault' damage zone.

The central gouge or cataclasite layer, which makes up the fault core, is a zone of localized slip (Engelder, 1974; Chester and Logan, 1986) and is formed through a process of cataclasis and grain-size reduction (Engelder, 1974). Engelder (1974) suggested that the thickness of a gouge layer of a fault is dependent upon the displacement of the fault, but it has an upper limit of roughly 5 cm.

Definitions of fault geometries that will be used in the thesis are indicated in Figure 1. The length of the fault is defined as the maximum dimension of the fault

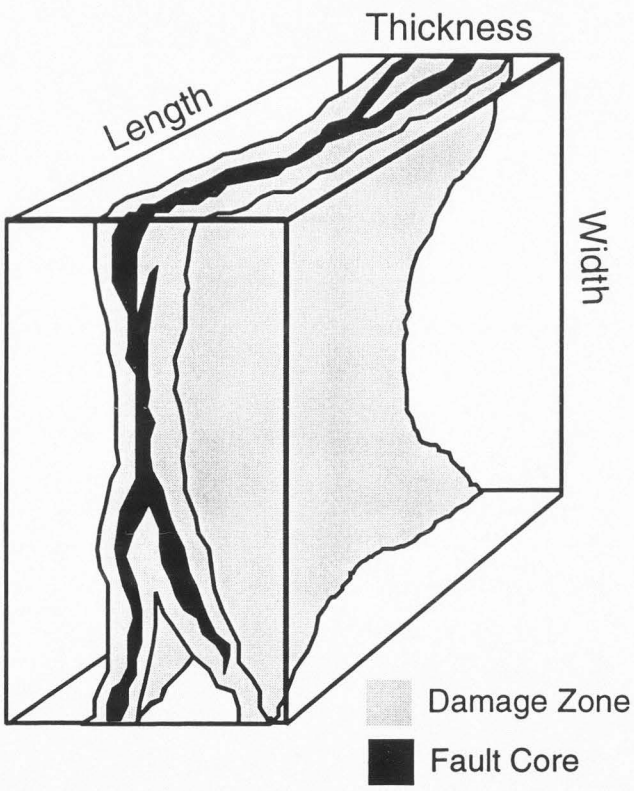

Fig. 2 Illustration of the three-dimensional geometries of a fault zone. Drawing is not meant to imply any scale (after Chester and Logan, 1986 and Smith et al., 1990).

plane in the slip direction and the width is the maximum dimension of a fault plane in the direction normal to the slip direction (Walsh and Watterson, 1988). The thickness of the fault is measured normal to the fault plane. In a strike slip fault, which is what the Punchbowl fault is, the length is the map distance of the fault, the width is how deep the fault extends, and thickness is the distance normal to the fault plane, which is this study's main focus. Often, measurements of fault zone thickness will be made from the fault core to the protolith, and will be designated as a half-thickness. This is not precisely a half-thickness, as the fault core is not necessarily the center of the fault zone.

PREVIOUS WORK

Anderson et al. (1980) conducted traverses across the northwestern end of the Mojave segment of the modern San Andreas fault zone in order to study the petrography of the fault gouge. The fault is bounded by crystalline rocks in this location and contains minor amounts of kaolinite. Fault zones that formed at depth and were later exhumed have also been studied. Anderson et al. (1983) examined cataclastic rocks from the San Gabriel fault zone in the western San Gabriel Mountains. Here, the fault cuts Precambrian and Mesozoic granitic and gneissic rocks. There was almost no clay developed in the San Gabriel gouge. No quantitative analysis of the deformation associated with the faults were made with either study, nor was the extent of deformation away from the main fault trace noted.

Two studies characterize large-displacement fault zones of the San Andreas fault system in granitic rock. Chester et al. (1993), examining the San Gabriel fault, documented slip localization and particulate flow in the ultracataclasite zone in the fault core. Evans and Chester (1995) further examined the San Gabriel fault zone using whole-rock geochemistry.

Chester and Logan (1986, 1987) examined the macroscopic and microscopic structures of the Punchbowl fault and the surrounding host rock. They concentrated their investigation in the Devil's Punchbowl County Park, where the fault places Tertiary Punchbowl Formation in contact with the Mesozoic Pleasant View Metamorphic Complex.

Most of the modern structural petrography, mineralogy, geochemistry, and structural analysis on the San Andreas fault system were done in granitic rocks and sandstones. This study examines the Punchbowl fault in a metamorphic terrain; this is

important when comparing the Punchbowl fault to the San Andreas fault, as the San Andreas cuts metamorphic rock in much of California.

LOCATION AND GEOLOGIC SETTING

The San Andreas fault is a right lateral strike-slip fault that is part of a system of faults that forms the boundary between the Pacific and North American plates. Portions of the fault formed 20 to 17 Ma as a transform fault between the Pacific and North American plates that has been relocated onto the continent (Powell and Weldon, 1992). Movement along the fault system is due to the relative motion of the two plates (Atwater, 1970; Powell and Weldon, 1992). The San Andreas fault extends from Cape Mendicino in the north to the Gulf of California in the south, with an orientation of NNW-SSE. The fault is nearly straight along its entire length, except for north of the Traverse Ranges, where the fault changes to more NW-SE orientation.

In the area north of the Transverse Ranges, the San Andreas fault has a large bend, commonly referred to as the "big bend." Over time, the San Andreas fault has migrated eastward in this area, possibly due to reorientation of the plate margin. As it migrated, the fault system left behind traces of what were previously active fault traces. Two of the larger and better exposed inactive traces are the San Gabriel and Punchbowl faults, which lie south of the Mojave segment of the San Andreas fault, which ruptured during a large earthquake in 1857 (Dibblee, 1968; Sieh, 1978). The San Gabriel fault was active from 12 Ma to 5 Ma and had a total displacement of 42 to 45 km (Powell and Weldon, 1992). The Punchbowl fault, which was active from 4 Ma to 1 Ma, has a total displacement of 44 km (Dibblee, 1968; Ehlig, 1981). These displacements are well constrained, as distinctive rock units are offset by the faults.

The San Gabriel and Punchbowl faults are located in the San Gabriel Mountains, in the central part of the Transverse Ranges, south of the San Andreas fault (Fig. 3). Uplift of the San Gabriel Mountains began 5 Ma along the Sierra Madre and

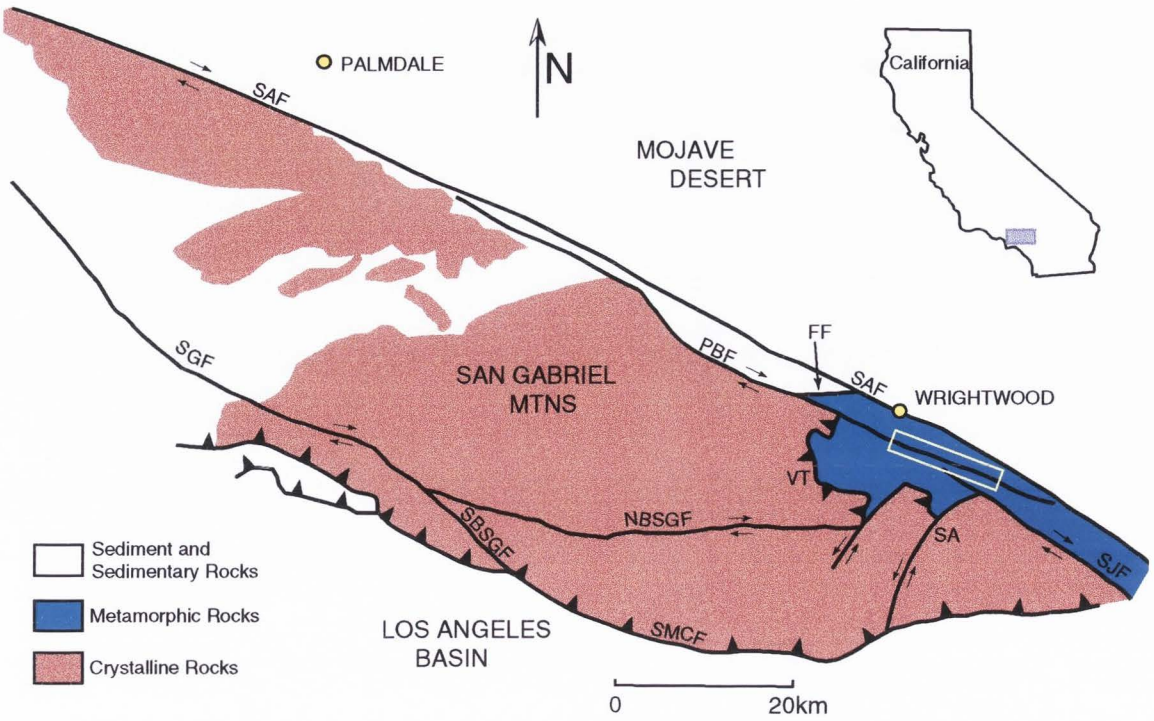

Fig. 3 Location map of the study region in the San Gabriel mountains, southern California. Box indicates the portion of the Punchbowl Fault that was investigated. Major faults are labeled; SAF - San Andreas fault, PBF - Punchbowl fault, SGF - San Gabriel fault, NBSGF - north branch of the San Gabriel fault, SBSGF - south branch of the San Gabriel fault, SMCF - Sierra Madre Cucamonga fault, SA - San Antonio fault, FF -Fenner fault, SJF - San Jacinto fault, VT - Vincent Thrust.

Cucamonga thrust faults (Fig. 3; Anderson et al., 1983; Ehlig, 1981). The thrusting is thought to be the result of a compressive stress state caused by the bend in the San Andreas fault system (Ehlig, 1981). The maximum uplift of the Transverse Ranges is between 4 to 9 km (Morton and Baird, 1975). The San Gabriel fault was exhumed 2 to 5 km (Anderson et al., 1983) and the Punchbowl fault 2 to 4 km (Chester and Logan, 1986).

The study area along the Punchbowl fault near Wrightwood, California (Fig. 4) extends from Devil's Punchbowl County Park in the west to Cajon Pass in the east.

Northwest of the study region, the fault juxtaposes the Tertiary Punchbowl Formation against older crystalline basement rock. Here, the fault strikes 294° with a dip of 70°SW on average, with a variation of 15° in strike and 26° in dip over a distance of roughly 6 km (Chester and Logan, 1987). Slip on the Punchbowl fault is right-lateral, with a slip direction that rakes 30° SE (Chester and Logan, 1987).

Noble (1954) mapped the San Jacinto fault as south of and parallel to the Punchbowl fault, with a 500-m-thick zone of crushed basement rock in between. This zone consists primarily of a white aplite composed of microcline and albite-orthoclase that intruded the Pleasant View Metamorphic Complex prior to faulting. Later mapping (Ehlig, 1987) does not show the San Jacinto fault this far northwestward, so it is not shown in Figure 4. It is likely that the crushed rock mapped by Noble were deformed by the Punchbowl fault.

In much of the study area, the Punchbowl fault has at least two main traces (Fig. 4; Jacobson, 1980; Dibblee, 1987; Ehlig, 1987; Weldon, 1987). Between the traces, there are slices of a wide variety of rocks (Dibblee, 1987); however, in the study area, the inter-trace rocks are limited to the Punchbowl Formation, Pelona Schist, and an unidentified aplitic unit. Much of the south trace is covered, especially along the Prairie Fork River (Fig. 4). In the middle portion of the field area, along the North Fork of Lytle Creek, the Punchbowl fault has been mapped as only a single strand (Noble, 1954; Ehlig, 1981). However, the fault in this area is not well exposed, and more than one major strand may be present. In the eastern end of the study area, Weldon (1987) has mapped the Punchbowl fault as consisting of multiple strands (Fig. 4). East of Interstate Route 15, the Punchbowl fault is covered. It is not certain what happens at the eastern end of the fault, but it most likely merges with the San Andreas fault system 3.5 km

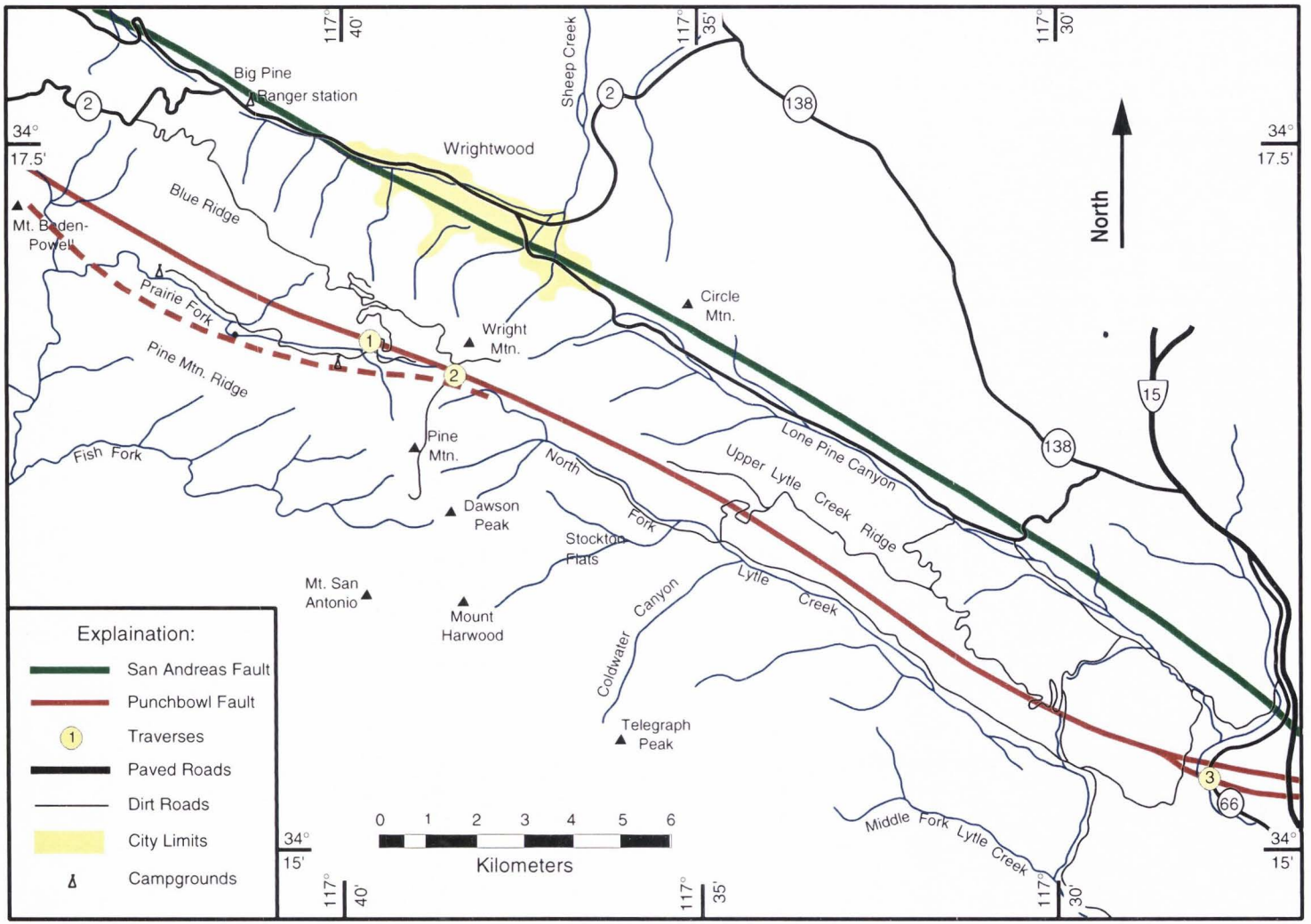

Fig. 4 Locations of the three traverses along the Punchbowl fault. The entire length of the fault shown was examined for locations that provided continuous exposure across the entire fault. The three study sites provide the most complete traverses.

southeast of Route 15, near Pitman Canyon (Dibblee, 1987).

The Pelona Schist is predominantly grey, quartzofeldspathic schist commonly referred to as metagreywacke (Ehlig, 1958; Jacobson, 1980; Haxel et al., 1986, 1987; Jacobson et al., 1988). Locally, there are minor amounts of greenschist, metabasalt, metacherts, and marble (Haxel et al., 1986). The principal mineral constituents of the Pelona Schist are albite, quartz, and muscovite, with minor epidote, graphite, and chlorite (Jacobson, 1980). The age of metamorphism of the Pelona Schist was previously thought to be Tertiary, but it is now known to be Late Cretaceous (Haxel et al., 1986).

In the study area, the Punchbowl fault divides the Pelona Schist into two blocks, the northern Blue Ridge block and the southern San Gabriel Mountain block (Dibblee, 1967; Ehlig, 1981). The Blue Ridge block is referred to as greyschist, with small occurrences of greenschist and minor beds of marble and quartzite (Dibblee, 1967). The Blue Ridge block also contains local masses of coarse actinolite and rare masses of talc schist, but there are no granitic, aplitic, or diabasic dikes. The San Gabriel Mountain block contains more biotite than the north block, with no marble, actinolite, or talc schist. There are, however, numerous dikes of aplitic to granophyric quartz monzonite.

Three traverses along the Punchbowl fault were examined in detail for this study (Fig. 4). The traverses were selected for their quality of exposure. The ideal traverse site would have the entire fault exposed, especially the fault core. It also requires that the host rock be exposed for at least 100 m on both sides of the fault. Most of the Punchbowl fault in the study region was searched, and such an ideal exposure was not found. The three sites chosen all have at least one fault core exposed and have reasonably good exposure of the fault zone and the host rock. Traverse 1 and 2 are located in areas where the Punchbowl fault has been mapped by Ehlig (1987) as having two main

branches. These branches are here identified as the north branch and the south branch. Between traverse 2 and 3, it is not known whether multiple branches are present because the fault is poorly exposed in this area. At traverse 3, the fault has multiple branches (Weldon, 1987).

Traverse 1 is the northwesternmost exposure studied. The exposure is along a dirt road that connects the top of Blue Ridge to the north with the Prairie Fork Valley to the south (Fig. 4). Beyond the fault exposure, there is a 180° bend in the road to the north, which provides a second exposure of the fault. The north branch of the Punchbowl fault is exposed at traverse 1, along with the intrafault rocks from between the two main fault branches (Fig. 4). The southern branch of the fault is not exposed. It lies roughly 1.2 km to the south of the north branch, and is located in the bottom of the Prairie Fork Valley (Ehlig, 1981). There is good exposure of the north branch of the fault to the northwest of traverse 1. Whenever the fault crosses a drainage, the fault is exposed on at least one canyon wall. These exposures, however, are not continuous, and therefore were not studied. The exposure at traverse 1 is continuous from 30 m north of the fault core to 150 m south of the fault core. The protolith exposure farther north of the fault core is less continuous, but still good.

Traverse 2 is located on a saddle between Wright Mountain and Pine Mountain along a hiking trail 2 km southeast of traverse 1 (Fig. 4). Both branches of the Punchbowl fault are exposed in this location. The two branches are 153 m apart and the exposure between them is almost continuous. The fault core of the north branch is not exposed, but its location can be determined to within 5 m by a change in rock units. The southern-branch fault core, initially buried, was exposed by digging. The protolith north of the northern branch of the fault core is well exposed for over 100 m. The rocks

south of the southern-branch of the fault core are poorly exposed, but the limited outcrop enables some analysis of the rocks.

Traverse 3 is located 12 km southeast of traverse 2, along Route 66 (Fig. 4), where a large road cut exposes the Punchbowl fault at the south end and the San Andreas fault at the north end. The Punchbowl fault splits into several branches northwest of traverse 3 (Weldon, 1987). The roadcut exposes over 100 m of continuous, undeformed Pelona Schist south of the Punchbowl fault with the southern branch of the Punchbowl fault exposed near a large drainage pipe. The rest of the fault zone to the north is also well exposed, both in the road cut and in the drainage walls below the train tracks along Cajon Creek. North of the southern branch of the Punchbowl fault, the rocks are intensely deformed. It is difficult to determine the source of the deformation due to the close proximity of the San Andreas fault. Barriers along Route 66 made it difficult to study the fault-related damage in this area, limiting the work at traverse 3 to the southern branch of the Punchbowl fault and the undeformed rocks to the south, even though the entire fault is exposed.

Between traverse 2 and 3 the Punchbowl fault is poorly exposed. The only two possible sites for traverses across the fault zone were at road cuts along the dirt road that connects Stockton Flats with the Upper Lytle Creek Ridge. These exposures are extremely weathered, and showed little of the undamaged host rock around the fault.

The following sections describe the deformation associated with the fault at a variety of scales. Mesoscopic, or outcrop-scale, deformation was determined by measuring the abundance of fractures, veins, and small faults at various locations across the fault zone. Deformation on a microscopic scale was also observed along the Punchbowl fault using both petrographic and scanning electron microscopes. The geochemical vari-

ability associated with the fault was determined by analyzing the changes in whole rock geochemistry and x-ray diffraction patterns of the rocks collected across the fault zone.

MESOSCOPIC DEFORMATION

Introduction

The physical characteristics and deformation associated with the Punchbowl fault were determined at the mesoscopic (outcrop) scale. The approach used assumes that the deformation associated with the fault zone consists mainly of alteration, foliation reorientation, and damage elements, which include fractures, slip surfaces, and veins. This deformation is distributed across the damage zone and fault core (Fig. 1).

The spatial variation of deformation across the fault zone was documented at each traverse. The deformation was defined both qualitatively, using descriptive variations in the amount of deformation, and quantitatively, where the change in deformation was measured. Deformation with respect to the distance from the fault core was recorded at numerous stations along each traverse. The stations are located at selected points along each traverse, beginning 100 m from the fault core, and extending through the damage zone and fault core. Previous studies of the San Gabriel and Punchbowl faults (Chester and Logan, 1986; Chester et al., 1993; Evans and Chester, 1995) have shown that all of the deformation associated with large strike-slip faults in this area occurs well within 100 m of the fault core.

Chester et al. (1993) and Evans and Chester (1995) noted that the greatest amount of the deformation associated with the Punchbowl and San Gabriel faults is localized within 10 m of the fault core. They also showed that the greatest change in the relative amounts of deformation occurs within this 10 m. Farther from the fault core, the density and amount of change in the deformation are much lower than in the rocks adjacent to the fault core, but higher than in the undeformed protolith. To record

the changes in deformation both close to the fault core as well as the changes farther from the fault zone, a logarithmic sampling approach to data collection was used. Outcrop exposure permitting, the stations along the traverses were placed every meter for the first 10 m from the fault core, then every 10 m beyond until a distance of 100 m beyond the fault core was reached. When there was no exposure at one of these predetermined locations, the nearest outcrop was used. In a few instances, the available outcrops were too weathered to provide a reliable measure of fault-related deformation.

Generalized cross sections of the three traverses are shown, with the locations of individual stations along each traverse indicated (Figs. 5, 6, and 7). The cross sections show the major branches of the Punchbowl fault and large subsidiary faults. Subsidiary faults contain a gouge layer and are continuous throughout the exposure, although they are not considered main branches of the Punchbowl fault because the gouge layer is not as well developed as the gouge of the main branches. The subsidiary fault located outside the fault zone in traverse 2 does not have much associated deformation in the adjacent host rock.

The exposure at traverse 1 (Fig. 5) does not extend across the entire fault zone. As shown in Figure 4, the Punchbowl fault has two main branches in this location (Ehlig, 1981), which are over 1 km apart. The traverse begins 100 m north of the north branch and ends 125 m south of the north branch. There is a subsidiary fault 55 m south of the fault core that is subparallel to the main trace of the Punchbowl fault (Fig. 5).

Traverse 2 crosses both the north and the south branch of the Punchbowl fault (Fig. 6). The two branches are 153 m apart, with good exposures allowing for a traverse across the entire fault zone. Fifty meters north of the north branch there is a subsidiary

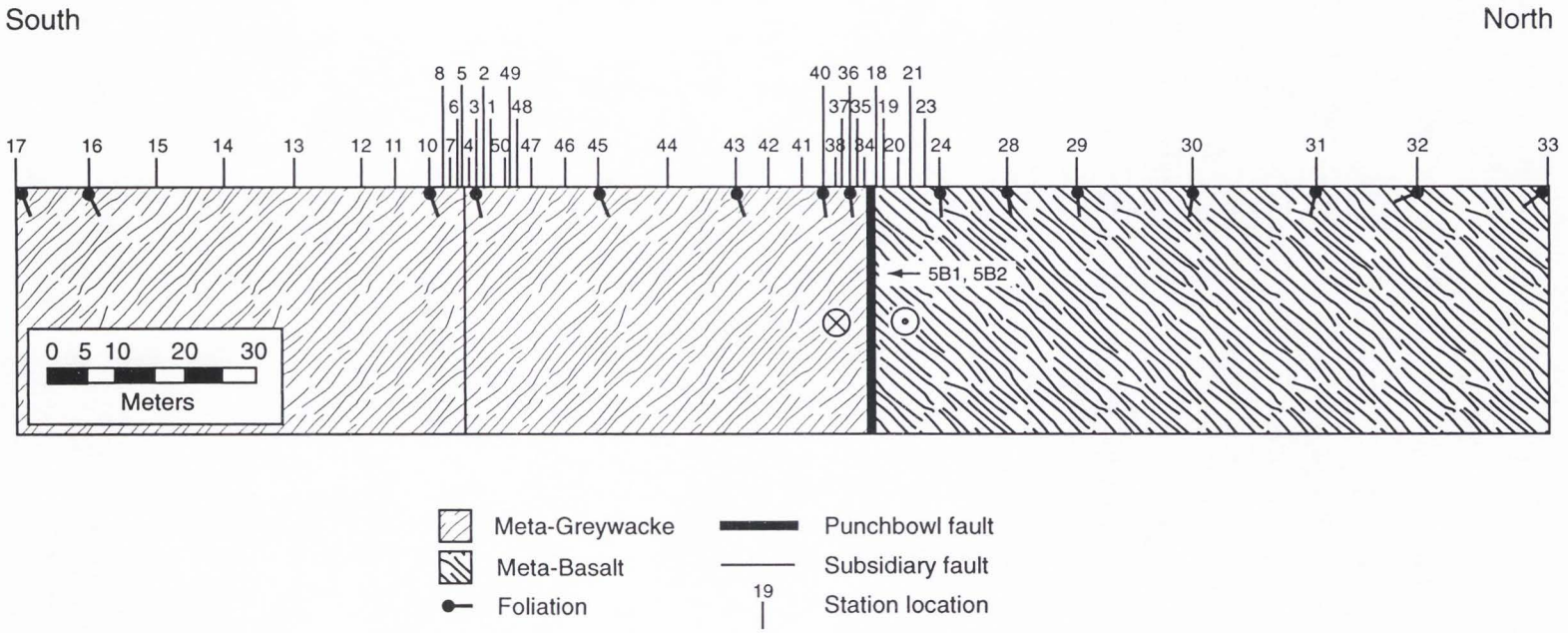

Fig. 5 Generalized cross section of traverse 1, from north to south. Numbers indicate the stations along the traverse where measurements were made. Subsidiary faults are large faults that do not appear to have as much associated deformation as the main branches of the Punchbowl fault. Tadpoles indicate the apparent dip of the schistose foliation in the Pelona Schist.

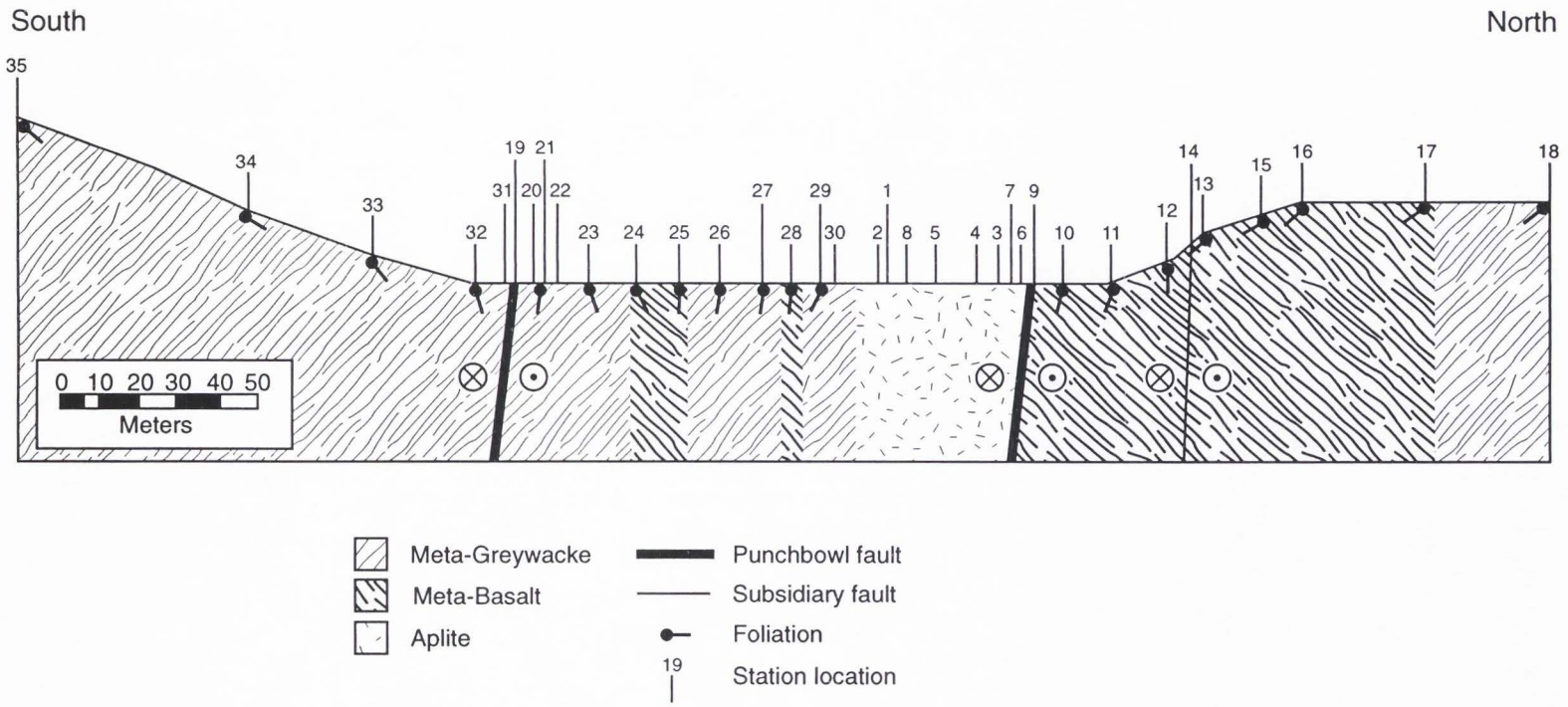

Fig. 6 Generalized cross section of traverse 2, from north to south. Numbers indicate the stations along the traverse where measurements were made. Subsidiary faults are large faults that do not appear to have as much associated deformation as the main branches of the Punchbowl fault. Tadpoles indicate the apparent dip of the schistose foliation in the Pelona Schist.

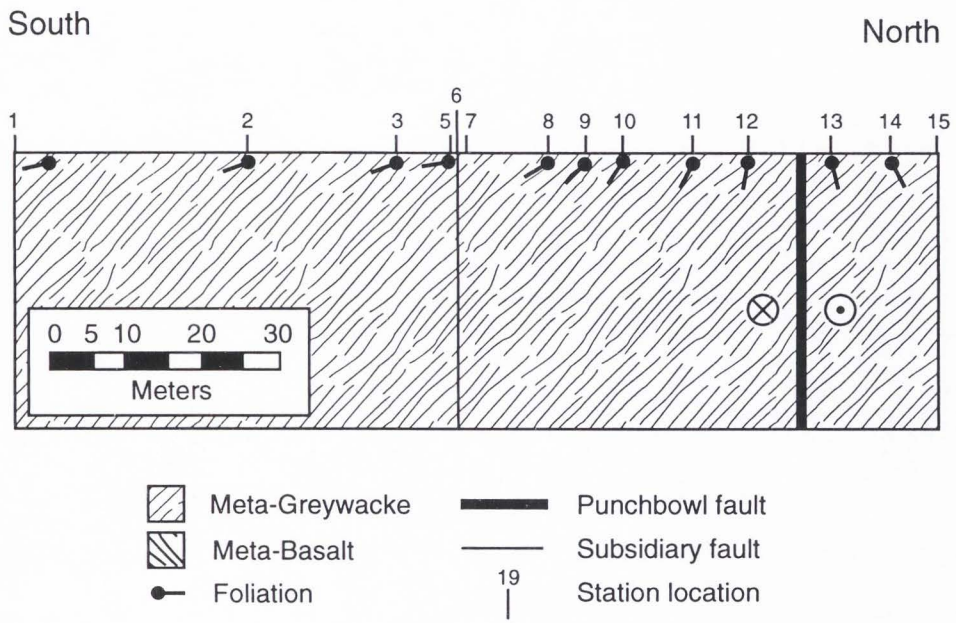

Fig. 7 Generalized cross section of traverse 3, from south to north. Numbers indicate the stations along the traverse where measurements were made. Subsidiary faults are large faults that do not appear to have as much associated deformation as the main branches of the Punchbowl fault. Tadpoles indicate the apparent dip of the schistose foliation in the Pelona Schist.

fault of unknown displacement subparallel to the Punchbowl fault. Figure 8 is a photograph of the saddle containing traverse 2 taken from traverse 1, which is located roughly 2 km to the west.

The third traverse is near the junction of the Punchbowl fault and the San Andreas fault (Fig. 4). The traverse begins 100 m south of the Punchbowl fault and extends 30 m north of the southern branch of the Punchbowl fault (Fig. 7). The traverse was not carried out any farther north beyond the southern fault core, because the rocks are deformed continuously from here to the San Andreas fault. The close proximity of

Fig. 8 Traverse 2 located in a saddle between two mountain peaks, southeast of traverse 1. The north and south branches of the Punchbowl fault are indicated. The distance between the north and south branches is 133 m.

the San Andreas fault to the Punchbowl fault may result in an overlap of fault-related deformation.

In the following, I present qualitative descriptions of the rocks at each of the three traverses, indicating how they alter in appearance throughout the fault zone. I will also describe the main fault core as well as the major subsidiary faults. The quantitative data that were collected at the mesoscopic scale will then be discussed. This will include the change in the density of damage elements throughout the fault zone, as well as orientations of the various structures.

Qualitative Description of Deformation

Qualitatively, the schist in traverse 1 appears relatively undeformed up to roughly 30 m from the fault trace, where the rock changes from a thinly foliated, grey, quartz-mica schist to a green-grey altered rock (Fig. 9). The schist has a well-defined foliation 80 m north of the fault core and it is unaffected by the Punchbowl fault (Fig. 9a). Nearer to the fault core, the rock becomes more altered and deformed. Fracture density intensifies and fractures are commonly oriented subparallel to foliation (Fig. 9b). Foliation becomes less closely spaced and more difficult to distinguish at roughly 30 m north of the fault core, where the rock becomes increasing more deformed (Fig. 9c). Note that the rock is much more fractured here than farther from the fault core. There is also a general increase in the number of slip surfaces and veins closer to the fault trace. Within 8 m of the fault core, the rocks become extremely fractured and friable (Fig. 10a).

The fault core at all locations in this study is a dark, fine-grained, and often foliated gouge. The fault core of the north branch of the Punchbowl fault at traverse 1 is

a)

b)

Fig. 9 Rock outcrops north of the fault core at traverse 1. a) Pelona Schist 80 meters north of the Punchbowl fault. The schist is undeformed, with little fracturing along the foliation. b) Exposure 47 meters north of the Punchbowl fault. The schist is more deformed than in the previous photo, with increased fracturing along foliation. c) The schist 30 meters north of the Punchbowl fault is strongly deformed and the schistose foliation is difficult to identify.

c)

Fig. 9 Continued.

less than 10 cm thick, with a brecciated zone roughly 15 cm thick on the south side of the fault core that is continuous across much of the outcrop (Fig. 10b). This breccia zone is not part of the fault core, as it is parallel to foliation but truncated by the fault core, and may reflect a localized lithological response to the deformation mechanisms occurring in the damage zone adjacent to the core. Breccia zones parallel to the fault core were not found at any of the other areas examined in this study, although the rock adjacent to the core at traverse 3 did have some brecciated regions. The core is dark, fine-grained, and slightly foliated. The foliation surfaces are oriented along strike of the fault core, and commonly contain slicken-lines that are oriented within 20° of horizontal.

South of the fault core at traverse 1, between the two branches of the Punchbowl fault, the rocks are a green-brown altered schist (Fig. 10c). The schistose foliation is not always apparent, whereas fractures and slip surfaces are prevalent. There is a small

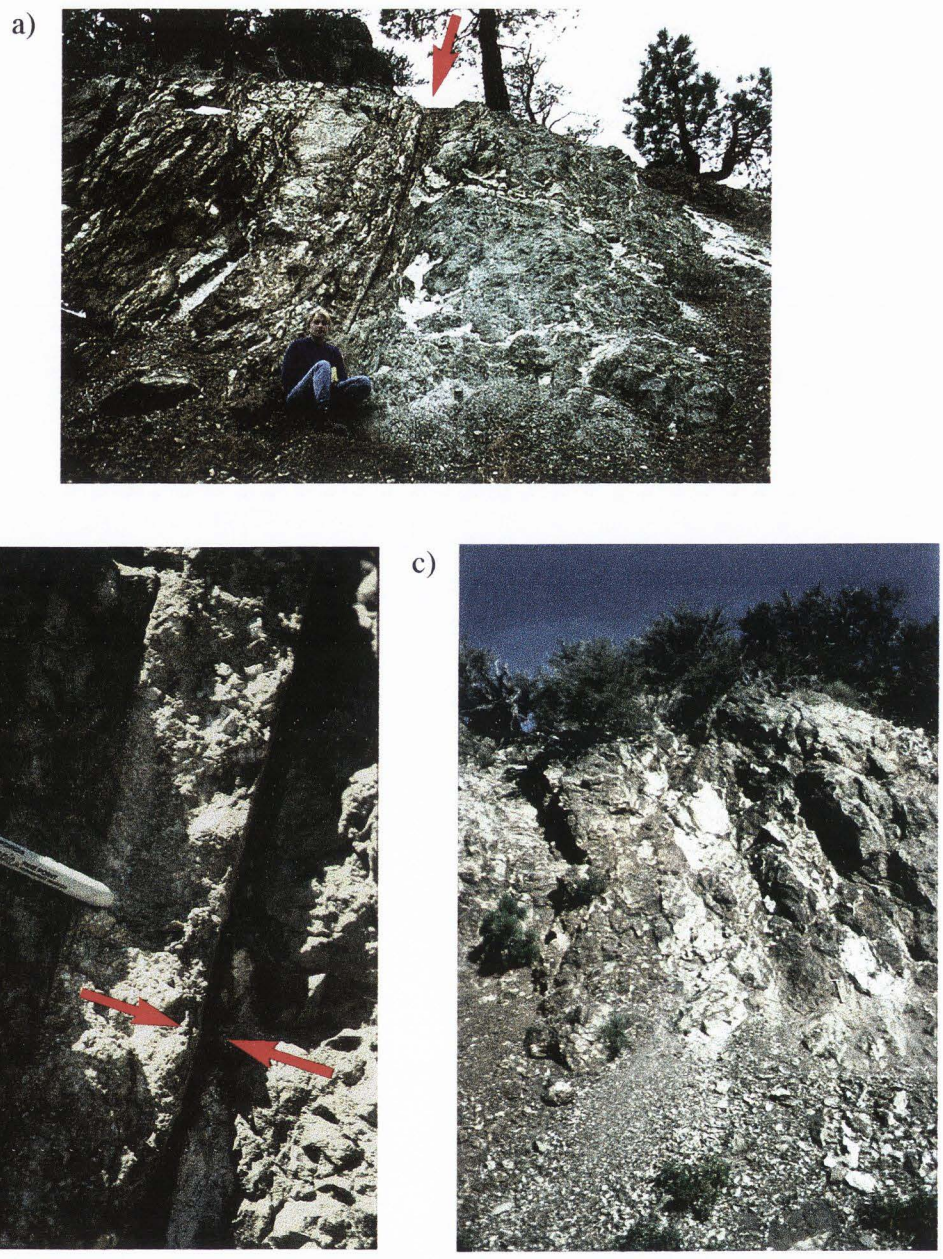

Fig. 10 The north branch of the Punchbowl fault and the rocks between the two main branches at traverse 1. a) Arrow indicates the trace of the north branch of the Punchbowl fault with the view toward the northwest. Note the damaged rock north of the fault trace shows little foliation; however, the schist south of the fault trace displays a prominent foliation that is sub-parallel to the fault. b) Closeup view of the main trace of the fault shown in Figure 8a. A 15 cm thick breccia zone is located south of the fault core, at the tip of the pen. Red arrows indicate the fault core. c) Rocks located between the two branches of the fault are less damaged than those adjacent to the fault core. View is to the east.

gully 55 m south of the fault core interpreted in the field to be the location of a major subsidiary fault due to an increase in the amount of fractures on both sides of the gully (Fig. 5). No evidence of fault gouge was found at this location, but this may be due to incomplete exposure.

At traverse 2, the schist appears fairly undeformed north of the Punchbowl fault at distances greater than 15 m from the fault core (Fig. 11). At greater than 60 m north of the fault core, the deformation is limited to widely spaced (usually greater than 20 cm apart) fractures (Fig. 11a). At 15 m north of the fault core, the schist becomes more fractured (fracture spacing typically 2 cm) and contains more slip surfaces and veins. Visually, these rocks appear less altered than the deformed host rock adjacent to the fault core at traverse 1. Because the rocks 0 to 10 m north of the north branch of the Punchbowl fault are not well exposed, it is difficult to define the exact extent of deformation adjacent to the fault core. The location of the north branch is inferred by the juxtaposition of different rock types. There is a 30-m-thick zone of aplitic rock which I interpret as a fault-bounded block in the Punchbowl fault zone. The north branch of the Punchbowl fault is mapped between this unit and the Pelona Schist to the north (Fig. 6).

Between the two branches of the Punchbowl fault the amount of alteration and deformation is variable. In the northern portion (stations 2.01-2.08) the rocks are a light-colored aplite that contains some foliated xenoliths of the host rock. This rock is deformed by the Punchbowl fault and contains small slip surfaces coated with red mineralization, probably hematite. What is inferred to be relic Pelona Schist between thick aplite sills has been offset by numerous normal faults (Fig. 12a).

The rocks farthest from the fault cores in the middle of the fault zone (stations 2.26-2.28) are less altered than the rest of the rocks closer to the two branches. These

a)

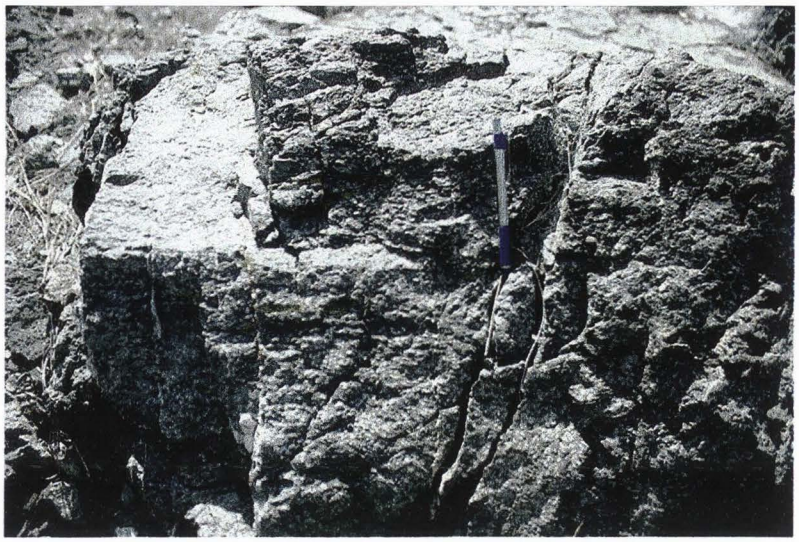

b)

Fig. 11 Rock outcrops north of the Punchbowl fault along traverse 2. a) 60 meters north of the fault. Although the rock is not intensely deformed, schistose foliation is not easily identified. b) 24 meters north of the fault. Large hornblende crystals appear to be a primary mineral of the Pelona Schist, and are unlikely to be related to deformation caused by the Punchbowl fault.

rocks are still identifiable as schist and have a well-developed schistose foliation, but they are more fractured than the schist found outside the fault zone. The schist was intruded by small (1-2 m thick) pods of aplitic rock before faulting. The intrusive rock is much more fractured than the schist (Fig. 12b) because much of the deformation in the schist is along foliation, which in this location is oriented roughly parallel to the Punchbowl fault. This pervasive foliation in the Pelona Schist may mask the amount of deformation the schist has undergone. The contrasting deformation in the two units shows that the lithology of the damage zone controls the amount, style, and orientation

a)

Fig. 12 Outcrops between the two branches of the Punchbowl fault at traverse 2. a) Intrusive rock that shows relic Pelona Schist (PS) between thick aplite sills, that has been offset by small faults. b) The light colored aplite appears much more fractured than the Pelona Schist. The fracturing in the Pelona Schist is predominantly foliation parallel. c) Close to the southern fault core, the Pelona Schist becomes more altered in appearance and the foliation contains small folds.

b)

c)

Fig. 12 Continued.

of the mesoscopic deformation.

The rocks in the southern portion of the intrafault damage zone are more massive and altered in appearance than the rest of the rocks between the two branches at traverse 2. The rocks are green-grey with a less well-developed foliation (Fig. 12c), which can be defined by thin (up to 6 cm) white bands and locally appears to be gneissic. The foliation close to the southern branch of the Punchbowl fault contains small (1 m) folds (Fig. 12b) which are absent at all other locations studied. The core of the south branch has a central cataclasite zone that is surrounded by an extremely deformed damage zone that extends roughly 2-5 m on either side (Fig. 13a). The core is a dark, fine-grained cataclasite with a distinct, nonplanar boundary. The core is 3-4 cm thick, and is moderately foliated along strike. The foliation surfaces commonly have slicken-lines, with dip-slip (up to 30° from horizontal) geometries.

South of the Punchbowl fault, the outcrop is not continuous. Close to the southern fault core, the rocks are deformed with an identifiable foliation to within 5 m of the fault core. The next good outcrop is over 25 m south of the fault core. There the rock is mostly undeformed, with most of the deformation limited to widely spaced fractures (Fig. 13b).

The qualitative observations of the rocks at traverse 3 are similar to those in traverse 2. The rocks show little alteration beyond 15 m from the fault core (Fig. 14a). The deformation that was observed is mainly an increase in fractures. Within 15 m of the fault zone, the rocks are much more altered in appearance (Fig. 14b). The rocks within 5 m of the fault core show little foliation and are very friable. There is also a slight increase in the density of slip surfaces close to the fault core, as well as locally abundant veining.

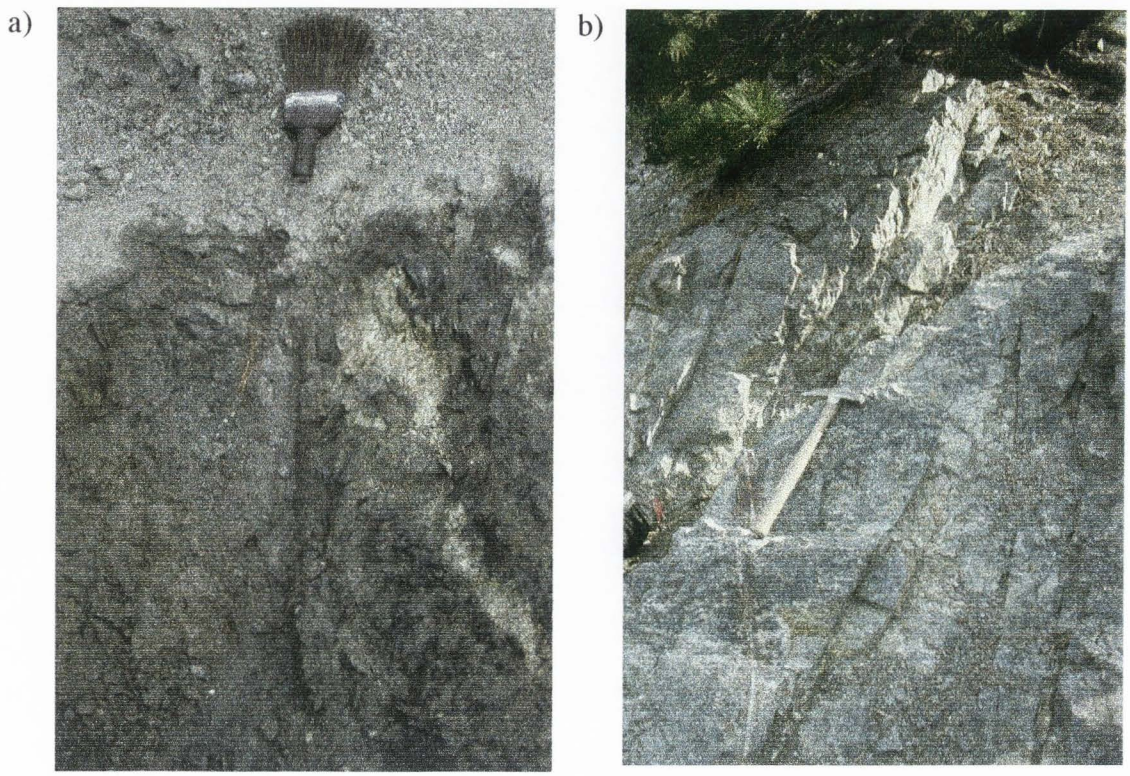

Fig. 13 The southern fault core at traverse 2 and an outcrop south of the fault. a) the southern fault core, located below the brush handle. View is toward the west of the southern fault core. b) Undeformed protolith 59 meters south of the southern branch of the Punchbowl fault. View is toward the northeast.

The fault core of the southern branch of the Punchbowl fault at traverse 3 does not consist of a single strand, but consists of a group of anastomosing gouge, and locally cataclasite, layers (Fig. 14c). The gouge layers are typically less indurated than the fault cores at traverse 1 and 2, and are also thinner, with each less than 2 cm thick. Typically, the gouge layers are not very foliated and are bounded by slip planes that usually show distinct slicken lines indicating strike-slip motion (less than 10° from horizontal). The rock surrounding the gouge layers is fine-grained, friable, and locally foliated, with a few areas that are brecciated. The brecciation at traverse 3 is irregular, unlike that documented at traverse 1, where the breccia zone is elongated parallel to foliation and has a

a)

b)

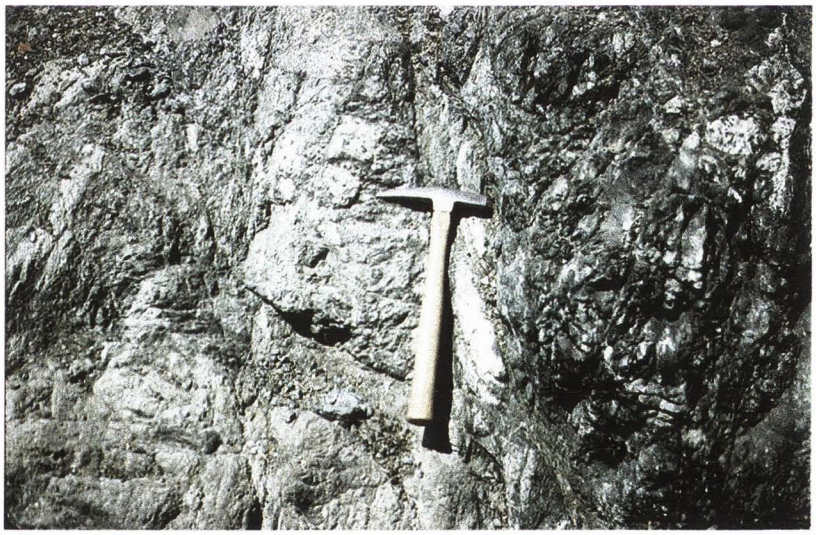

Fig. 14 Rock outcrops along traverse 3. a) Undeformed Pelona Schist 100 meters south of the fault core. b) Pelona Schist 5 meters south of the fault core. The rock is very deformed and heavily altered. c) The fault core of the southern branch of the Punchbowl fault consists of several anastomosing cataclasite bands. These bands are indicated with arrows. The rock adjacent to the cataclasite bands is very fractured.

c)

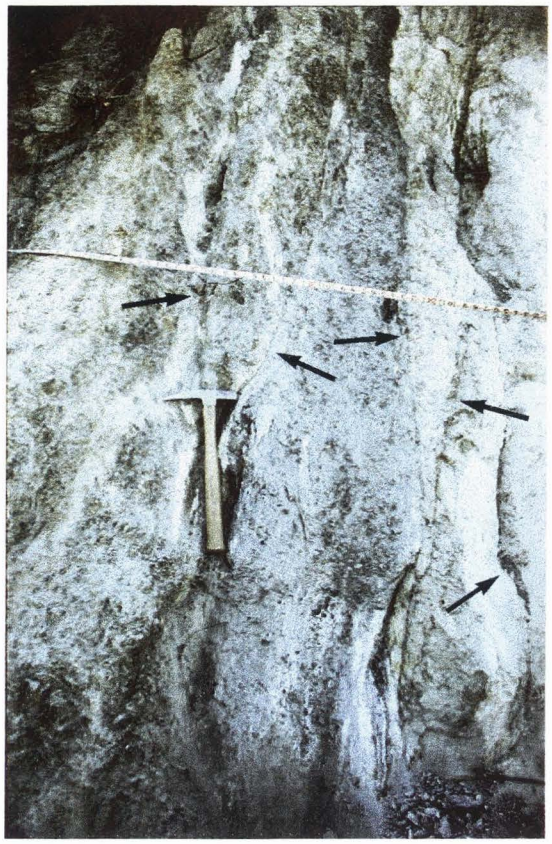

Figure 14 Continued.

relatively constant thickness. North of the fault core, the rocks have a schistose foliation and are less deformed than the rock adjacent to the core, although they show a much greater abundance of fractures and slip surfaces than the undeformed host rock south of the fault core.

Qualitative observations of the rocks at all three exposures indicate that the majority of the deformation associated with the Punchbowl fault occurs within 50 m of the fault core, with the most intense alteration and deformation concentrated within roughly 15 m of the fault core. The next section presents a quantitative assessment of the spatial distribution of the deformation at the mesoscopic scale.

Quantitative Description of Deformation

Quantitatively, the amount of mesoscopic deformation was determined by using a line intersection method, in which the numbers of features that intersect a scan line are counted. At individual stations across each traverse, the numbers of fractures, slip surfaces, and veins that intersected a 70 cm scan line were counted. Four scan lines were used at each station, two vertical and two horizontal, to reduce the effect of local variations in each outcrop on the results.

To determine the density of damage elements, the numbers of fractures and slip surfaces that intersected scan lines at each station were counted. There are fewer slip surfaces than fractures at all stations, which may be due in part to the difficulty distinguishing slip surfaces from schistosic foliation in the field. This problem is discussed later in this section. The data from the two vertical transects were averaged, then added to the average of the two horizontal transects to determine the number of damage elements, and then plotted in relation to the distance from the fault core (Fig. 15). The densities for macroscopic deformation are given as the number of damage elements per meter. The vein density is highly variable and was analyzed separately from the other damage elements. At all three traverses, the density of damage elements increases as the fault core is approached, reaching a value maximum adjacent to the fault core. A best fit line or curve was not plotted, as constraining the data to a formula is not justified. However, the increase in deformation in all damage zones does appear to be logarithmic, with the largest change in the intensity of deformation occurring near the fault core.

In all three traverses, the increase in deformation occurs gradually as one moves from the protolith, through the damage zone, and towards the fault core, making it difficult to determine the exact location of the contact between the damage zone and pro-

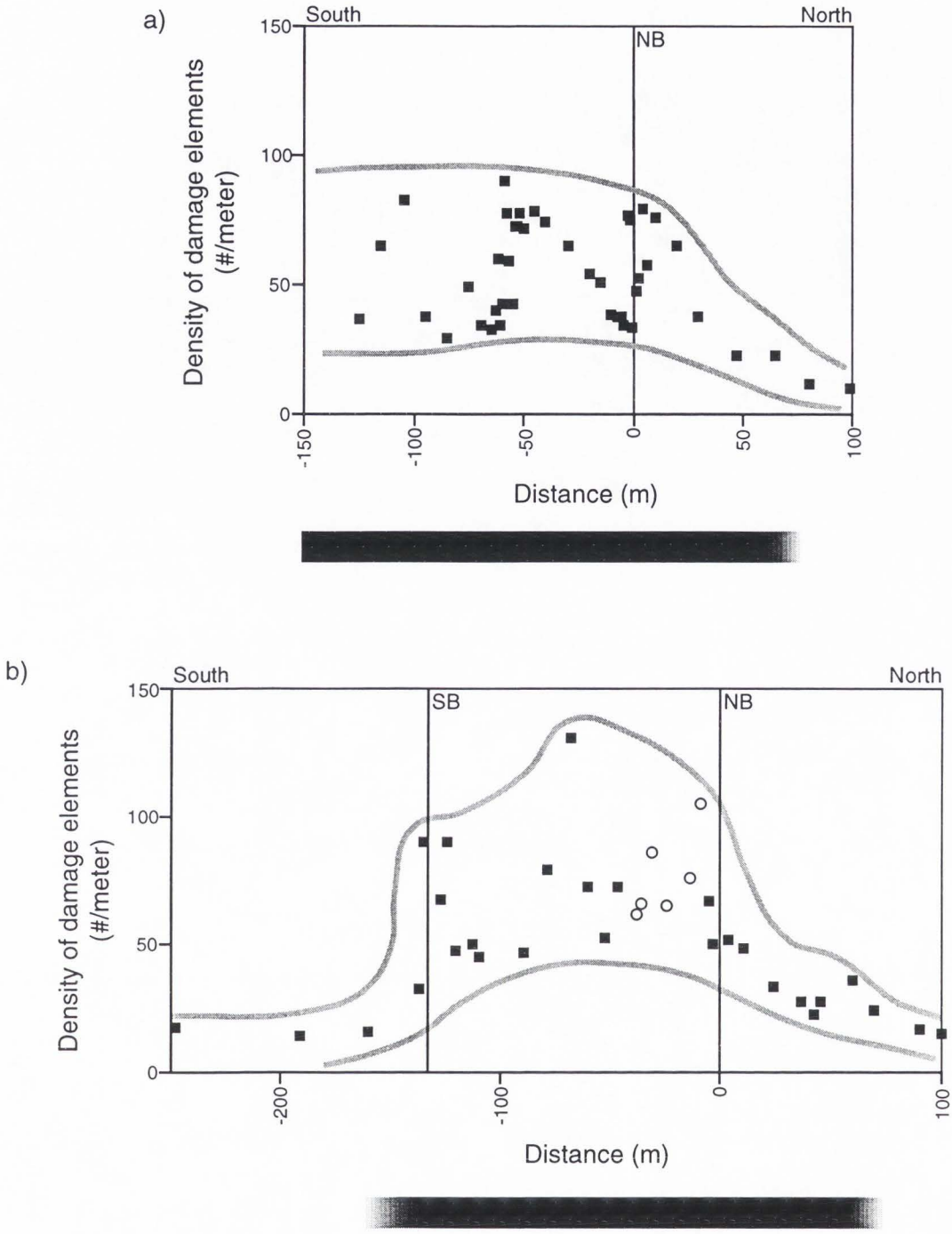

Fig. 15 Densities of mesoscopic damage elements plotted with respect to the distance from the fault core. Open circles are in the aplite and closed squares in the pelona schist. Solid lines indicate the location of fault cores of the major strands of the Punchbowl fault. Subsidiary faults are indicated by dashed lines. Grey lines outline the maximum and minimum deformation ranges measured. The bar beneath each graph shows the extent of the damage zone. a) Traverse 1. b) Traverse 2. c) Traverse 3.

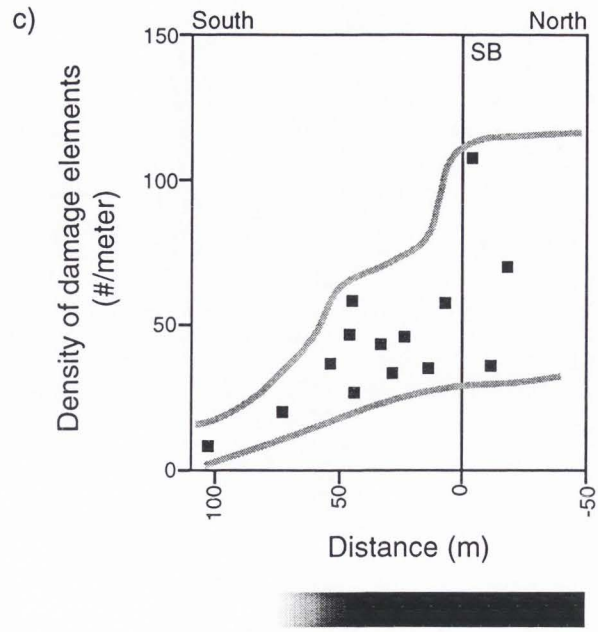

Fig. 15 Continued.

tolith (Fig. 1). The location of this contact can be estimated by determining the distance from the fault core where the density of deformation appears to be greater than the usual background deformation density normally associated with the protolith.

The increase in the density of damage elements begins roughly 50-70 m from the fault core at traverse 1 (Fig. 15a). The rocks near the fault core show a damage element density of about 10 times greater than the rocks 100 m from the fault core. The rocks directly south of the fault core at traverse 1 show an apparent decrease in the number of damage elements. This decrease may not accurately reflect the intensity of deformation because the rocks are so intensely deformed it is difficult to isolate individual fractures and slip surfaces (Fig. 10a). South of the fault core, there is a second peak in the density of damage elements within the fault zone. This peak occurs 55 m south of the fault core and corresponds to a subsidiary fault (Fig. 5). This local increase in the

density of damage elements is possibly an indication of slip localization within the fault zone.

The increase in macroscopic deformation at traverse 2 begins roughly 70 m north of the Punchbowl fault (Fig. 15b). The increased density of damage elements adjacent to the fault core is roughly four times that of the density of the protolith. The density of damage elements between the two strands of the Punchbowl fault is quite variable, but it is always greater than the density in the undeformed protolith. The highest density of damage elements within the intrafault damage zone occurs within 10 m of the fault core.

A small increase in the deformation density 60 m north of the northern fault core is associated with a subsidiary fault (Fig. 15b). South of the southern branch of the Punchbowl fault, the increase in deformation within the damage zone appears to begin closer to the fault core than what is seen north of the fault. However, with the limited exposure south of the Punchbowl fault, it is difficult to determine the protolith-damage zone contact with much certainty.

At traverse 3, the macroscopic density of damage elements is lower in the damage zone than at the other two traverses (Fig. 15c). The deformation associated with the Punchbowl fault begins to increase at about 50 m from the fault core. A small increase in the density of damage elements 45 m south of the fault core corresponds to a subsidiary fault (Fig. 7). The density of the damage elements south of the fault core is variable, but generally greater than the undamaged protolith.

The mesoscopic analysis shows that the deformation associated with the Punchbowl fault is greatest near the fault core. It increases from the relatively undeformed protolith to maximum levels at the regions of slip localization. It is around these

regions of slip localization that most of the deformation is concentrated. For all three traverses, the increase in the density of damage elements begins 50-70 m from the fault core. Fractures, faults, and veins become pronounced roughly 20 m from the fault core. The density of damage elements between the two branches of the Punchbowl fault shows a large amount of variability in both traverse 1 and 2, but is generally lower than the densities at the fault core and greater than the density of the undeformed rock over 50 m north of the fault core. The density data may underrepresent the actual amount of macroscopic deformation, as the schistose foliation masks fractures and slip surfaces in the Pelona Schist.

The vein density was measured utilizing the same methods as the other macroscopic damage elements. The veins are mainly filled with quartz, calcite, and minor laumontite and are thin (less than 2 cm) and 5 to 100 cm long. Figure 16 shows the vein density with respect to the distance from the fault at all three stations. Whereas there appears to be a general increase in vein density close to the fault cores, the locations of increased vein density are sporadic and do not follow the trends seen in the other deformation structures, especially in traverse 2.

In traverse 1, veins become abundant 20 m from the fault core; at distances greater than 20 m north of the core, veins are mostly absent. The number of veins south of the fault core at traverse 1 is highly variable, ranging from 0 to greater than 20. North of the fault core of traverse 2, the vein densities are sporadic, and do not increase close to the core. Between the two fault cores, the vein densities are also sporadic, similar to what is seen at traverse 1. The greatest vein density in traverse 2 occurs at the southern fault core. However, this intensely veined region is adjacent to a region almost devoid of veins. In traverse 3, there is a general increase in vein densities close to the

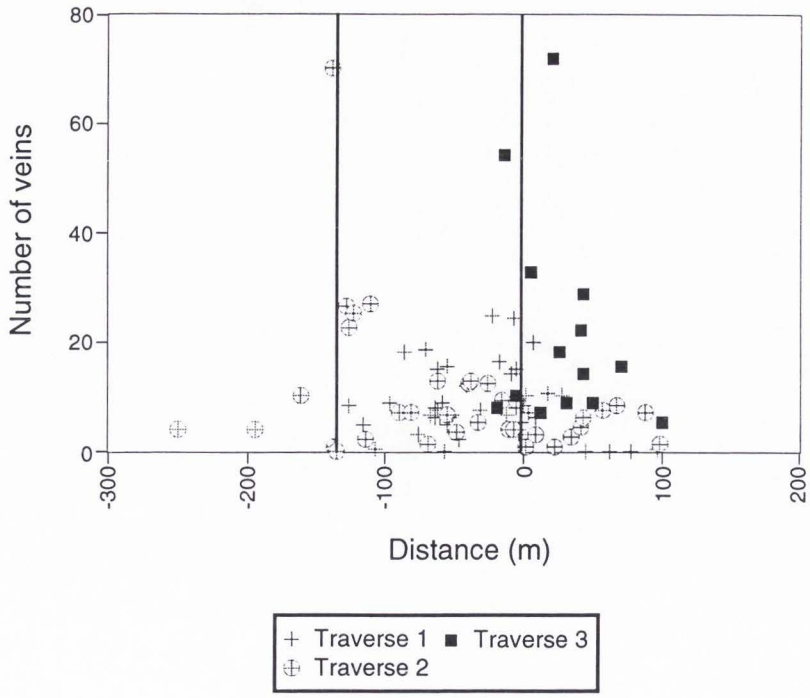

Fig. 16 Spatial distribution of veins along the three traverses. Positive distances are all outside of the fault. The distance of 0 m is the north branch of the Punchbowl Fault at traverse 1 and 2 and the south branch at traverse 3. All of the negative distances are between branches of the fault, except for traverse 2. The southern branch at traverse 2 is located at 133 m, so everything beyond this point is outside of and south of the fault.

fault core, but as in the other traverses, there is a large variability in the data. The localized regions of veins may be an indication of the continual formation and destruction of veins within a complex system and the variability in the presence of fluids across the fault zone.

Structural Analysis

The orientations of the fault core vary among the three traverses (Fig. 17). The fault cores at traverses 2 and 3 strike northwest, whereas the fault core at traverse 1 strikes more westerly. They are steeply dipping, with dips that range from 80°S at traverse 1 to 79°N at traverse 3 (Figs. 18, 19, and 20). The fault core is a nonplanar, anas-

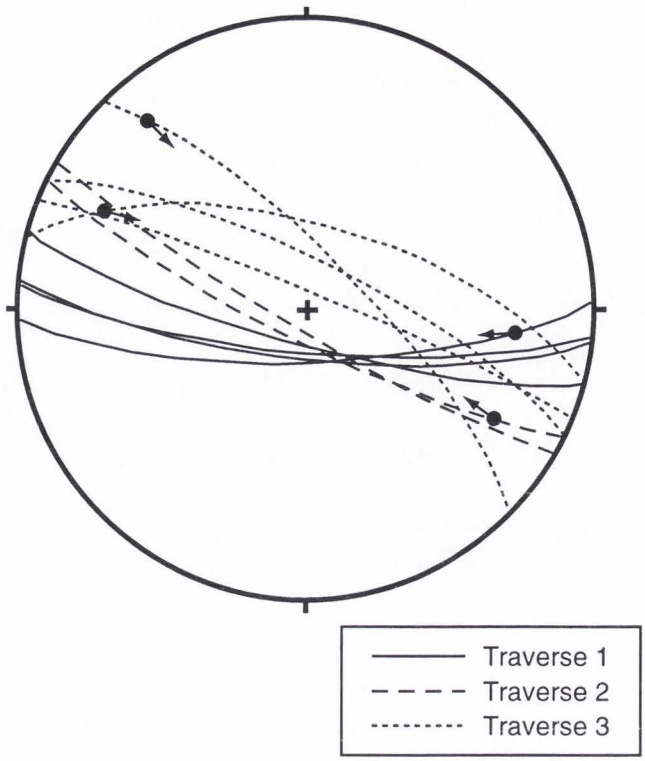

Fig. 17 Lower hemispheric stereographic projections of the fault core orientations at the three traverses. Slip vectors, which are included for slip surfaces where they were obtainable, show that the slip sense is right-lateral.

tomosing structure within the entire fault zone.

Deformation of preexisting structures can be used to estimate the fault structure, thickness, and strain distribution adjacent to the fault. In this area the foliation of the Pelona Schist provides a regional marker to determine the effects of the fault on the protolith.

The cross sections of the three traverses in Figures 5, 6, and 7 show that the apparent dip of the schistose foliation steepens near the fault at all three traverses. At traverse 1, the dip of the foliation steepens 45°-50° at roughly 50 m north of the fault core and remains close to vertical throughout the damage zone. The foliation dip is also nearly vertical between the two strands of the Punchbowl fault. The strike of the folia-

tion rotates roughly 45°, becoming subparallel to the north branch of the Punchbowl fault within 50 m of the fault core along traverse 1 (Fig. 18). In between the two branches, the foliation orientation is subparallel to the fault core.

The foliation 100 m from either side of the Punchbowl fault is shallowly dipping in traverse 2 (Fig. 6). The foliation steepens by 40° to nearly vertical within 50 m of the fault core north of the fault and by 30° within 20 m of the fault core south of the fault. Between the two branches of the Punchbowl fault, the foliation ranges in dip from 73° to vertical with the strike subparallel to the fault core. Although the strike of the foliation at 100 m from the fault core at traverse 2 is more nearly parallel to the strike of the fault than that at the other stations, making changes in strike less noticeable at this location than in the other traverses, there is a rotation of greater than 30° (Fig. 19). The schistose foliation between the two strands has more variation in orientation than in traverse 1, with local folding near the southern fault core; however, it is still oriented roughly parallel to the fault core. All of the folds in the schistosity occur in the more deformed rocks (Fig. 12b) just north of the south branch of the Punchbowl fault.

At traverse 3, a reorientation in the strike of the schistose foliation of almost 90° occurs within 10 m of the south trace of the Punchbowl fault (Fig. 20). North of the fault core the foliation is subparallel with the main trace of the Punchbowl fault for a distance of a least 20 m. The dip of the foliation steepens by roughly 30° near the fault. The reorientation of foliation occurs much closer to the fault core at traverse 3 than in the other two traverses.

The data show that the foliation is reoriented subparallel to the main trace of the Punchbowl fault. The changes in the strike of the foliation are not as dramatic as the changes in dip. In all cases, the foliation steepened adjacent to the Punchbowl fault,

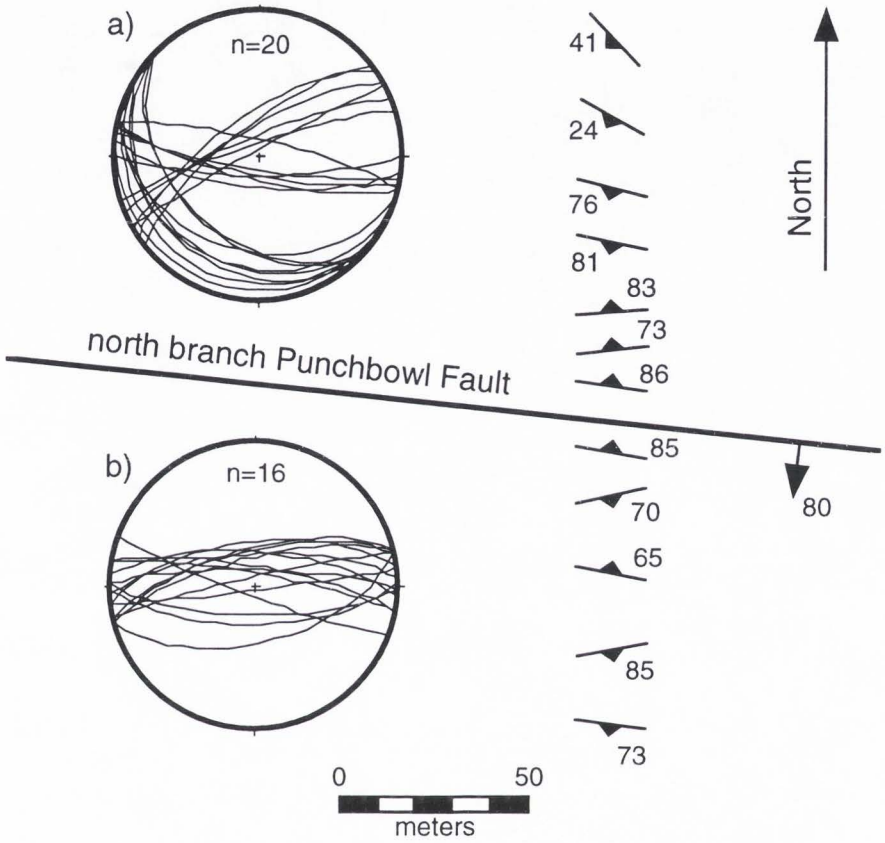

Fig. 18 Map showing lower hemispheric stereographic projections of foliation orientations in the Pelona Schist at traverse 1. Solid line is the main branch of the Punchbowl fault. Dip of the fault is indicated. a) Stereogram of the planes of the foliation north of the fault. b) Stereogram of the planes of the foliation south of the fault. There is a branch of the fault south of the map region. Stereograms of these groups of orientations were plotted using Stereonet 4.6a (Allmendinger, 1988).

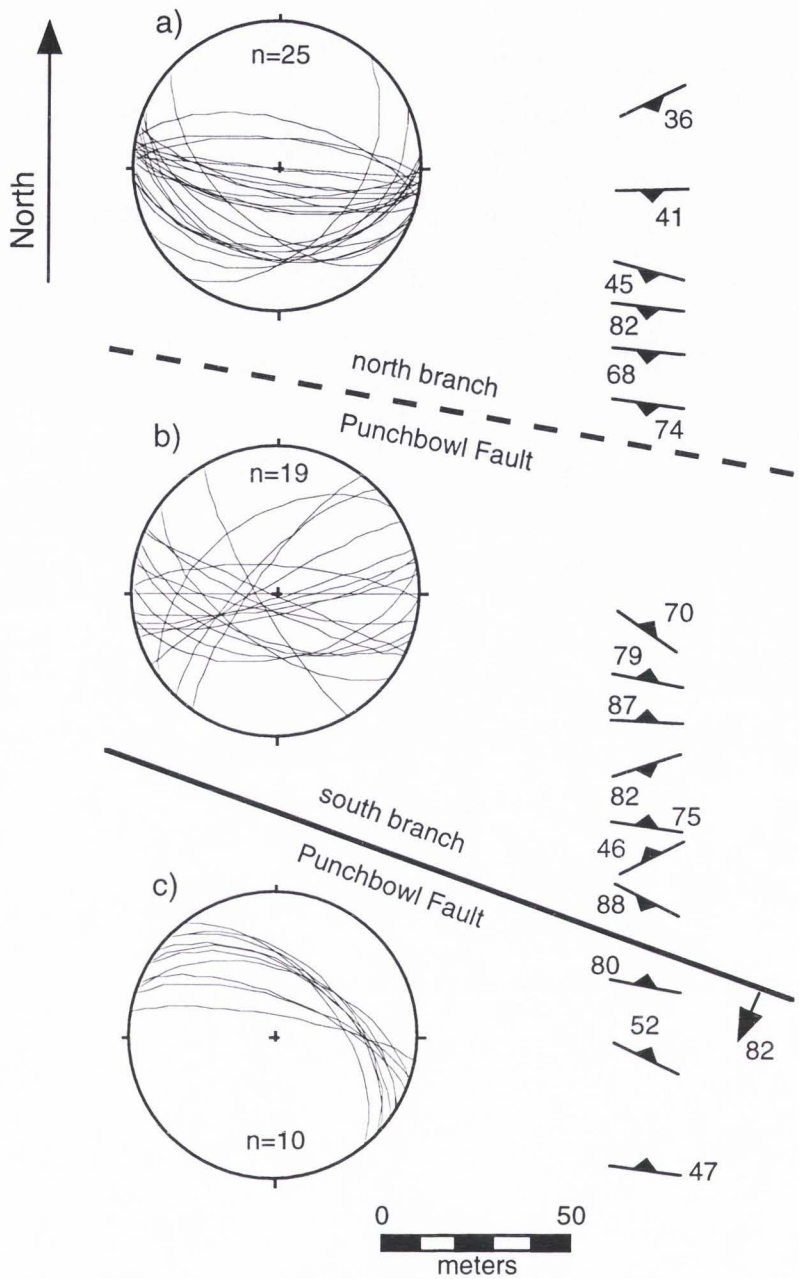

Fig. 19 Map showing lower hemispheric stereographic projections of foliation orientations in the Pelona Schist at traverse 2. The lines are the main branches of the Punchbowl fault, dashed where inferred. Dip of the fault is indicated. a) Stereogram of the planes of the foliation north of the fault. b) Stereogram of the planes of the foliation between the two branches of the Punchbowl fault. c) Stereogram of the planes of the foliation south of the fault. Stereograms of these groups of orientations were plotted using Stereonet 4.6a (Allmendinger, 1988).

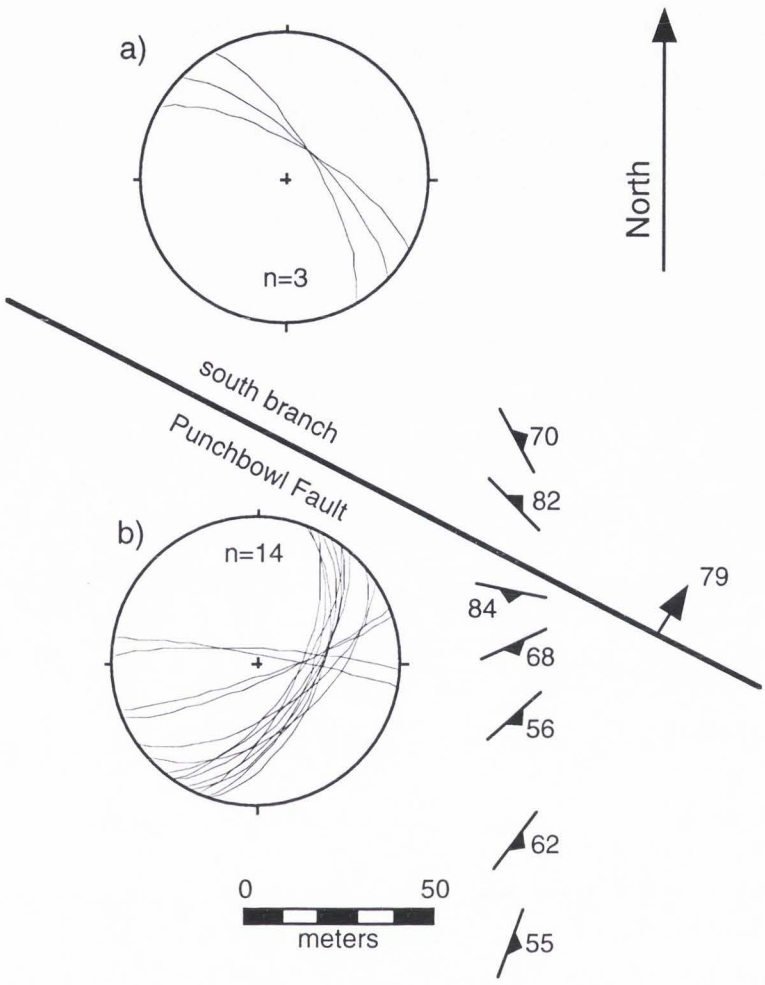

Fig. 20 Map showing lower hemispheric stereographic projections of foliation orientations in the Pelona Schist at traverse 3. Solid line is the main branch of the Punchbowl fault. Dip of the fault is indicated. a) Stereogram of the planes of the foliation north of the fault. There is a branch of the fault north of the map region. b) Stereogram of the planes of the foliation south of the fault. The solid line is the main branch of the Punchbowl fault. Stereograms of these groups of orientations were plotted using Stereonet 4.6a (Allmendinger, 1988).

perhaps in response to movement along the Punchbowl fault. The foliation reorientation may be the result of frictional drag on the Punchbowl fault or rotation due to simple shear in the fault zone. If the damage zone were part of the shear zone associated with the fault, then the foliation would rotate with continuing shear. The 44 km of right-lateral slip on the Punchbowl fault indicates a large amount of simple shear, which would result in almost 90° rotation of markers parallel to the fault. The foliation experienced approximately 90° of rotation at traverse 3 (Fig. 20), but there is less then 45° of rotation of foliation at traverse 1 and 2 (Figs. 18 and 19). Once the foliation was rotated parallel to the fault, no further rotation occurred because further slip could have been taken up along foliation surfaces. This may account for the smaller angles of rotation measured in traverses 1 and 2. The geochemical data presented in a later section show that there may also be a component of pure shear, as well as simple shear. When the foliation is rotated to subparallel with the fault zone, further shear can be accommodated by slip along the foliation, not with further rotation. This is similar to shearing a deck of cards, where the individual cards slid along each other with increased amount of shear. Volume loss would further reduce the amount of mesoscopic reorientation of the foliation.

Although it is possible that the steep foliation predates the Punchbowl fault and is due to normal variations in schistose foliation orientation, this is unlikely because the steepening foliation is consistent at all three traverses and Jacobson (1980) showed that such sharp variations in the regional foliation orientation are not common throughout the Pelona Schist.

The orientations of fractures and slip surfaces at each station were measured along the traverses across the Punchbowl fault. It was not possible to measure the ori-

entation of every fracture at each traverse although the orientations of all the major sets of fractures were measured. Orientations from the less predominant sets of fractures were collected as well. There are fewer slip surfaces than fractures, making it possible to include the measurement of orientation of every identifiable slip surface.

All of these orientations were then placed into groups that were determined by their general location within the fault zone. For instance, the fracture orientations from 0-10 m north of the fault core at traverse 1 were grouped together, whereas all of the fractures north of the fault core are placed into another group. These group stereograms were then placed on cross sections to show how the orientations of these structures vary over the fault zone. The stereograms shown on each cross section plot both the poles to the planes and the Kamb contour of the poles. Full-sized stereograms are shown in Appendix A, where the two plots are separated and the statistics for each stereogram are provided.

At traverse 1, the main fault trace, which is the fault core, strikes 096° and dips 80°SW (Fig. 21). Between the branches of the Punchbowl fault in traverse 1 there is a girdle pattern to the fracture orientations (Fig. 21a, b, and d). For these three plots, the first and second eigenvalues are similar and much greater then the third eigenvalue (Appendix A). If the state of stress in the fault zone were constant, fracture sets would form at specific orientations as a response to the stresses and kinematics of the fault. The girdle pattern between the two branches of the Punchbowl fault suggests that either the stresses within this region are rotating or that the rock rotated during formation of the fractures. North of the fault core the orientations of the poles to fractures are more consistent (Fig. 21c and f). On average, fractures strike 244° and dip 12° NW and lie about 30° counterclockwise from the main fault. This suggests that the stress field was

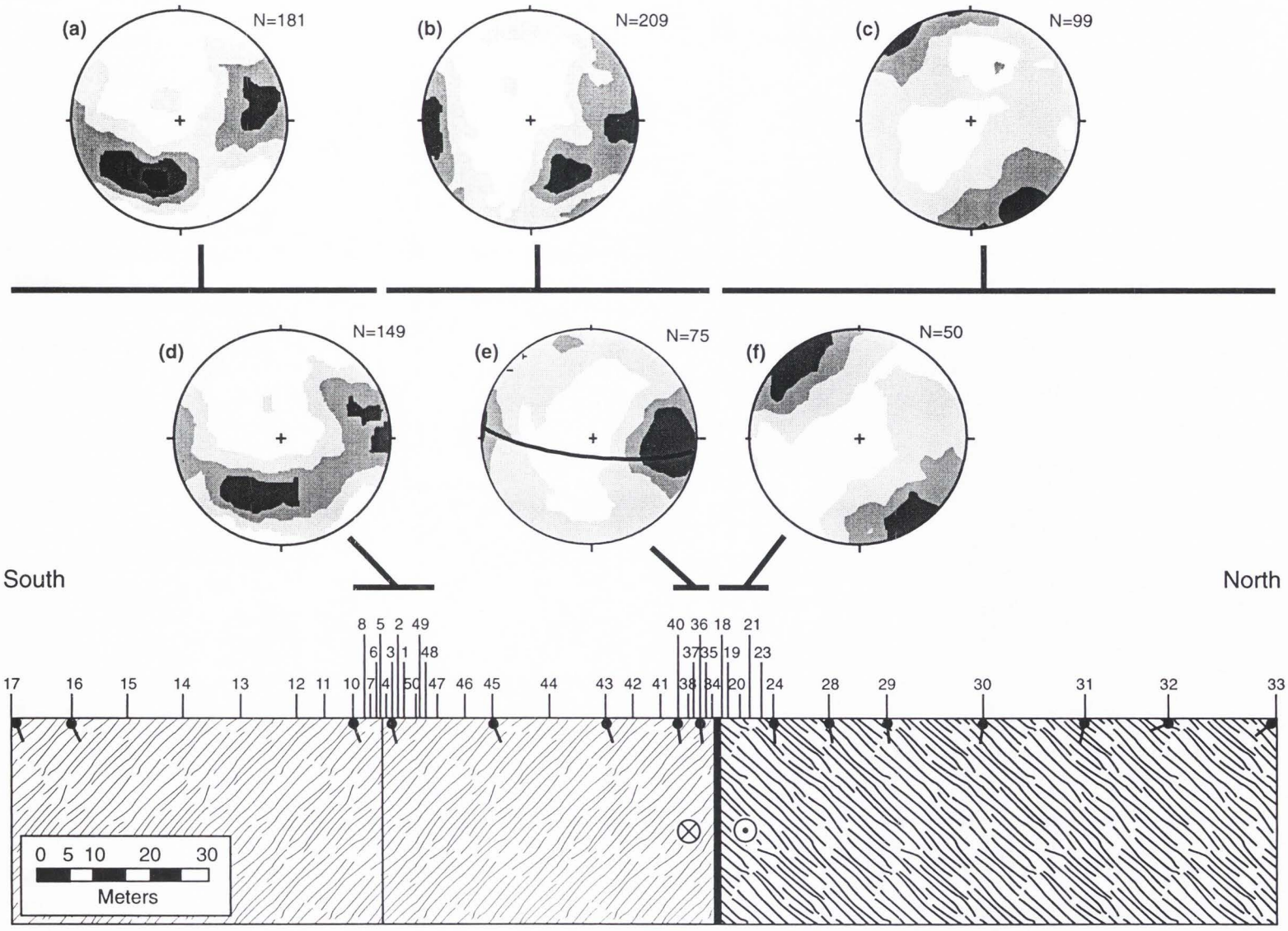
(a)
N=181
(b)
N=209
(c)
N=99
(d)
N=149
(e)
N=75
(f)
N=50
South
North
8 5 2 49
6 3 1 48
40 36 18 21
37 35 19 23
17 16 15 14 13 12 11 10 7 4 50 47 46 45 44 43 42 41 38 34 20 24 28 29 30 31 32 33
0 5 10 20 30
Meters

fairly constant and the distribution of fracture orientations measured between the branches of the fault was caused by block rotation.

The south branch of the Punchbowl fault at traverse 2 strikes 120° and dips 84°SW (Fig. 22). North of the fault at traverse 2, the fracture orientations are scattered, with little preferred orientation. The north branch was not exposed, but appears to strike more east-west than the south branch. There is a strong clustering of subhorizontal fractures between the two branches of the Punchbowl fault (Fig. 22b and e). The stereogram from the intrusive aplitic pod between the two fault branches shows no preferred orientation of fractures (Fig. 22f), with a more uniform distribution of deformation than in the schist. This may be due to the schist being mechanically more heterogeneous than the igneous rock. South of the south branch of the Punchbowl fault at traverse 2, the fractures are oriented similarly to the fractures between the two branches of the fault (Fig. 22a and d). Close to the fault core there are too few data points to define the geometries of the damage elements (Fig. 22d and g).

The south branch of the Punchbowl fault at traverse 3 strikes 297° and dips 75°NE (Fig. 23). There are two main concentrations of fracture orientations south of the fault at traverse 3 (Fig. 23a). This is similar to the girdle distribution seen in the intrafault damage zone at traverse 1 (Fig. 21a and d), although there is a significant scatter to the data. North of the fault, the fracture orientations are scattered (Fig. 23).

Figure 24 shows the stereograms of slip surfaces across traverse 1. There is a distinct clustering of slip surfaces in the rocks south of the north branch of the Punchbowl fault. Eigenvalues obtained for these stereograms (Appendix A) also suggest that there is a strong concentration of slip surface orientations with an average strike of 054° and dip of 43°SE. No sense of slip was determined from these data.

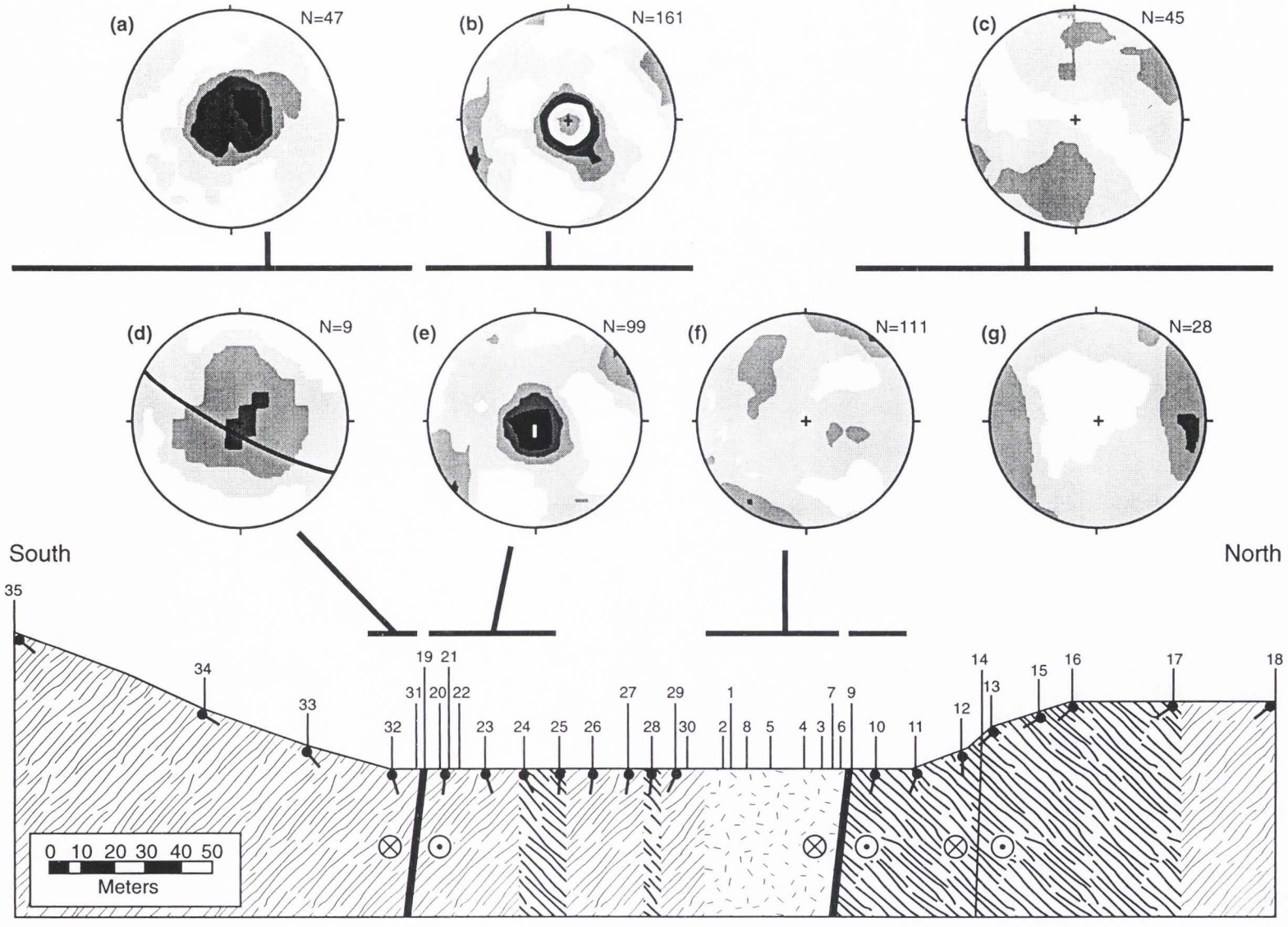
(a)
N=47
(b)
N=161
(c)
N=45
(d)
N=9
(e)
N=99
(f)
N=111
(g)
N=28
South
North
35
34
33
32
19 21
31 20 22
23
24
25
26
27
29
28
30
1
2
8
5
4
3
7 9
6
10
11
12
14
13
15
16
17
18
0 10 20 30 40 50
Meters

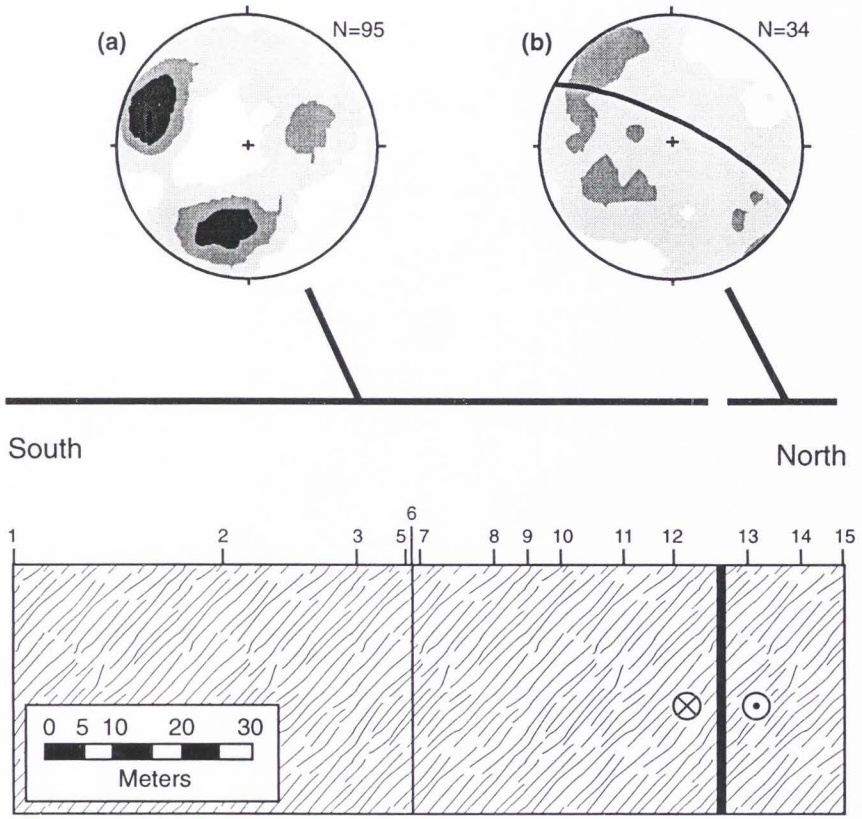

Fig. 23 Lower hemispheric stereographic projections of fracture orientations at traverse 3. Mean orientation of the southern fault core is shown by the great circle in stereogram b). The Kamb contour plots are of the density of the poles relative to a uniform population, with the first contour level at 3 sigma, and a contour interval of 2 sigma. Inverted "T-bars" indicate stations from which stereonets are taken. See Appendix A for enlargements of the stereograms. See Figure 5c for explanation of symbols and patterns. a) Fracture orientations from stations 3.01 through 3.12. b) Fracture orientations from stations 3.13 through 3.15. Stereograms of these groups of orientations were plotted using Stereonet 4.6a (Allmendinger, 1988).

These slip surfaces are highly oblique to the main fault trace, which strikes 097° and dips 77°SW. This orientation may reflect the kinematics of the brittle faults as seen in both field and laboratory experiments (Logan et al., 1981; Petit, 1987). Specifically, they could be P shears of a riedel shear system (Logan et al., 1981).

North of the fault core at traverse 1 the slip surface orientations are also clustered, although not as strongly as those south of the fault core (Fig. 24c and f). These small faults strike 347° and dip 48°E on average, with a high degree of scatter in the data.

The slip surface data for traverse 2 (Fig. 25) are not as well clustered as the data for traverse 1 (Fig. 24). Between the two main fault traces, the orientations are varied and not well clustered, with eigenvalues less the 0.5. North of the north strand of the Punchbowl fault, small faults strike 294° and dip 39°NE on average, which is close to the strike of the main fault although the dips differ by 60° (Fig. 25b). It is possible that these slip surfaces were visible amongst the foliation because they are not dipping as steeply as the foliation. South of the southern strand of the Punchbowl fault, there are too few data points to draw any conclusions (Fig. 25c).

At traverse 3 (Fig. 26), most of the small faults dip moderately to steeply north or northeast (Fig. 26), and there is no significant difference between the orientations of small faults on either side of the southern strand of the Punchbowl fault. Only a small number of faults were measured at traverse 3, making conclusions drawn from these data speculative. These small faults are subparallel to the main Punchbowl fault.

Absent from these fault measurements are a large number of small faults that are subparallel to the main fault trace. As previously discussed, I believe that these small faults exist, but are masked in the field by the foliation in the Pelona Schist. Close to

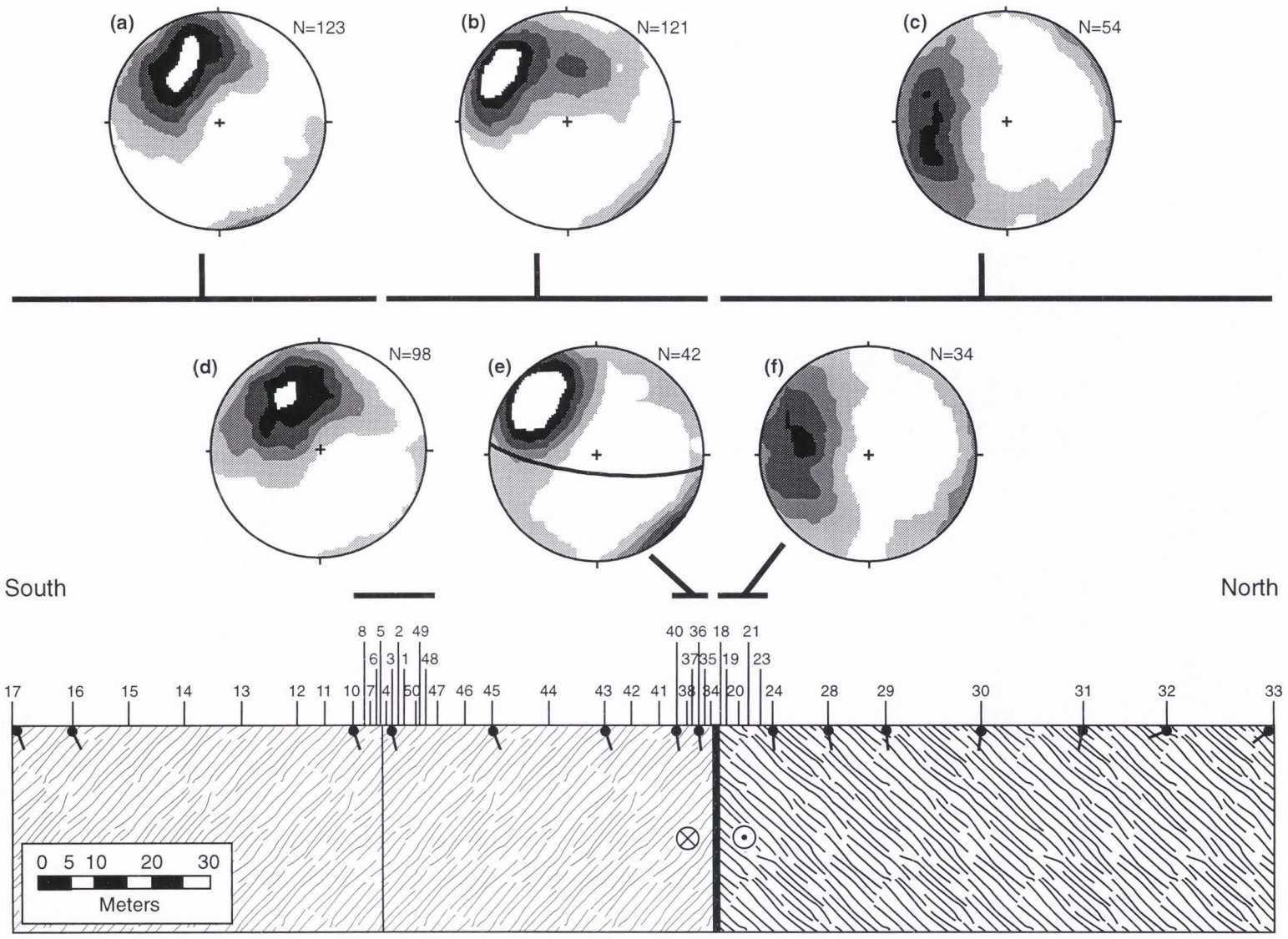
(a)
N=123
(b)
N=121
(c)
N=54
(d)
N=98
(e)
N=42
(f)
N=34
South
North
8 5 2 49
6 3 1 48
40 36 18 21
37 35 19 23
17 16 15 14 13 12 11 10 7 4 50 47 46 45 44 43 42 41 38 34 20 24 28 29 30 31 32 33
0 5 10 20 30
Meters

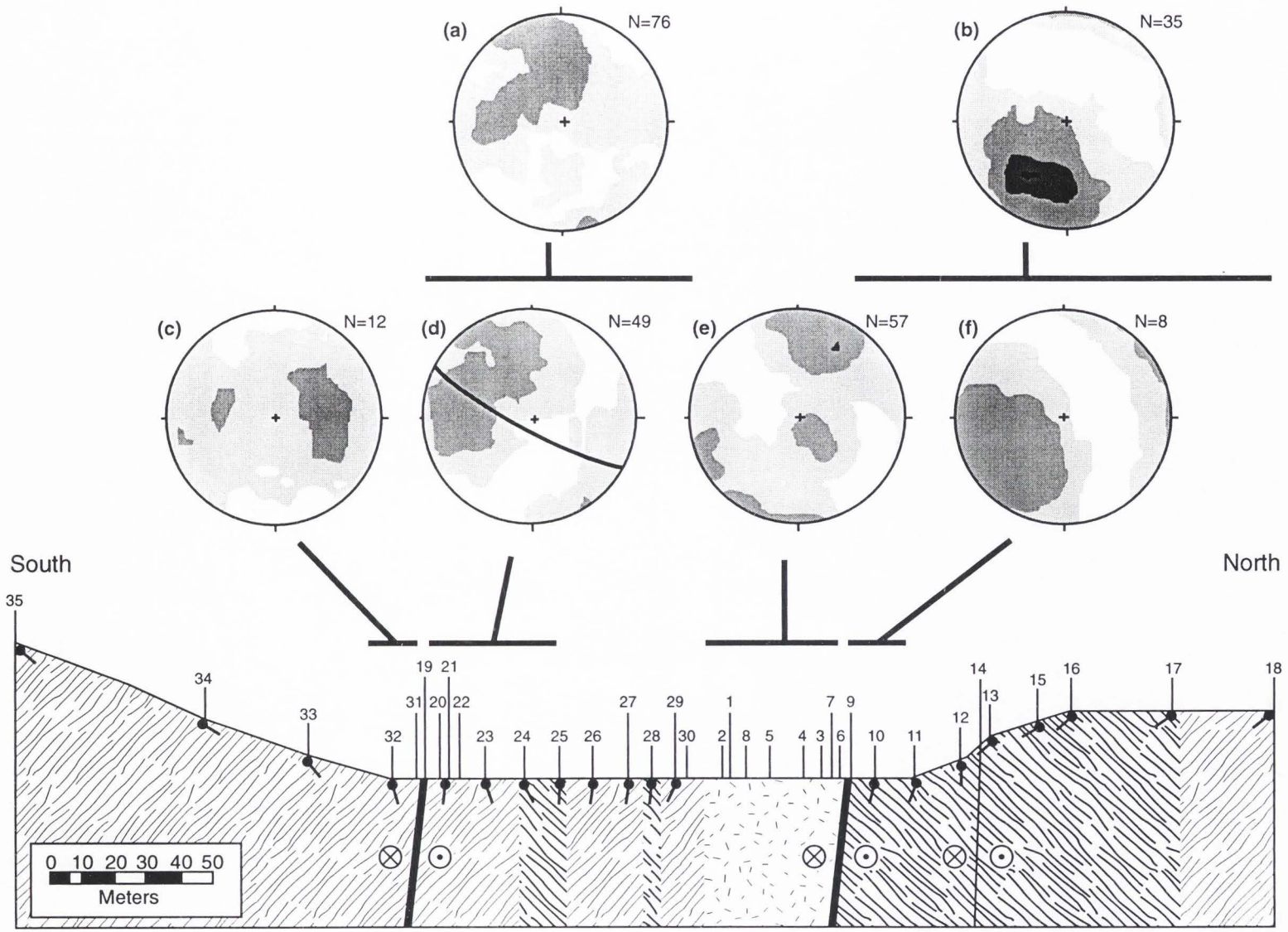
(a)
N=76
(b)
N=35
(c)
N=12
(d)
N=49
(e)
N=57
(f)
N=8
South
North
35
34
33
32
19 21
31 20 22
23
24
25
26
27
29
28
30
1
2
8
5
4
3
7 9
6
10
11
12
14
13
15
16
17
18
0 10 20 30 40 50
Meters

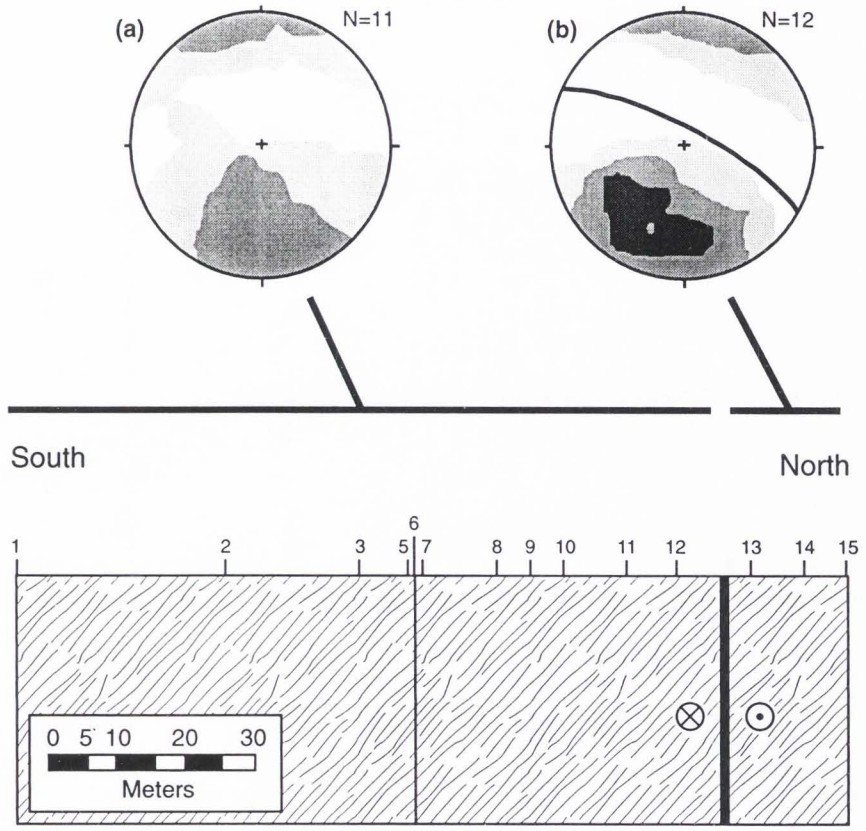

Fig. 26 Lower hemispheric stereographic projections of slip surface orientations at traverse 3. Mean orientation of the southern fault core is shown by the great circle in stereogram b). The Kamb contour plots are of the density of the poles relative to a uniform population, with the first contour level at 3 sigma, and a contour interval of 2 sigma. Inverted "T-bars" indicate stations from which stereonets are taken. See Appendix A for enlargements of the stereograms. See Figure 5c for explanation of symbols and patterns. a) Slip surface orientations from stations 3.01 through 3.12. b) Slip surface orientations from stations 3.13 through 3.15. Stereograms of these groups of orientations were plotted using Stereonet 4.6a (Allmendinger, 1988).

the fault core and in between the two fault branches, the schistose foliation is subparallel to the fault trace, making it difficult to distinguish slip surfaces along foliation. The slip surfaces that are present rarely have good slip indicators and there were few markers to determine offset of these small faults. Most of the slip vector data were determined from examining slickenlines, and these were often of questionable quality. Consequently, the slickenline data that were collected show scattered slip vector directions (Fig. 27). In both of the traverses, much of the slip was seen on faults at a high angle to the main fault trace. A detailed kinematic analysis was not done, as small faults could have been rotated during faulting and there are no constraints on where rotation occurred.

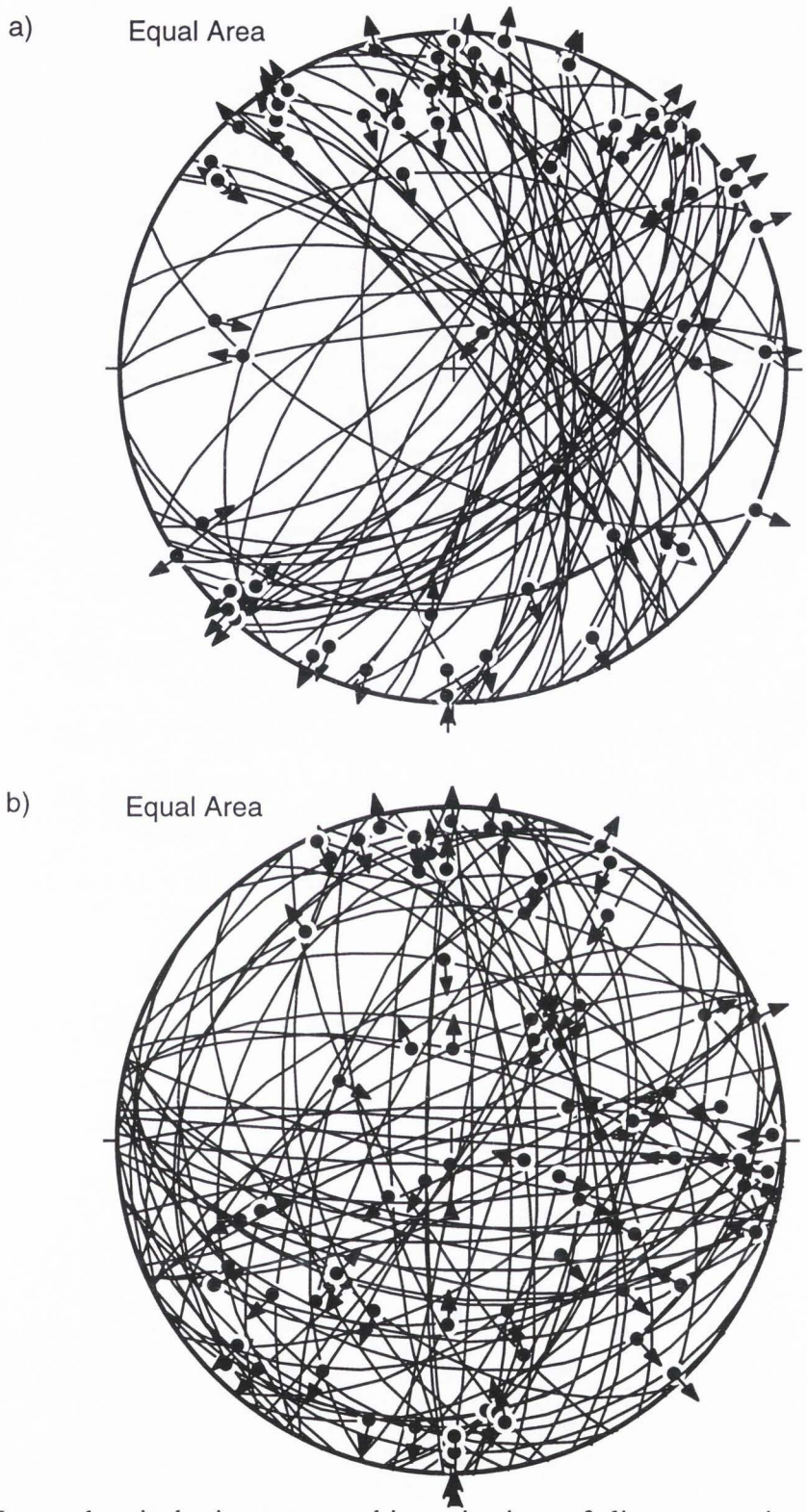

Figure 27 Lower hemispheric stereographic projections of slip vector orientations from small faults. a) Traverse 1. b) Traverse 2.

MICROSCOPIC DEFORMATION

Introduction

The microscopic structures associated with the Punchbowl fault were examined to determine the textures and deformation mechanisms across the fault. Along each of the three traverses across the Punchbowl fault, samples were collected for petrographic analysis, then cut along two planes: one vertical and perpendicular to the fault core and one horizontal. Because the thin sections are oriented perpendicular to the fault core, only the thin sections that are within roughly 30 m of the fault core or between the two fault strands are roughly perpendicular to the foliation. Thin sections further away from the fault core tend to be oblique to the foliation of the Pelona Schist.

At the microscopic scale, the deformation structures associated with the fault and how they varied spatially across the fault zone and in the surrounding protolith were investigated. The textures were examined for each thin section in order to gain insight into the types of deformation and processes involved during faulting. The amount of deformation present in the thin sections was measured, as was the change in grain size across the fault zone, to provide a quantitative estimate of the deformation associated with the Punchbowl fault.

Traverse 1 provided the best samples of the fault core and surrounding rock. Thin sections of the core of the north branch and also multiple thin sections from within 1 m of the Punchbowl Fault were obtained. The southern branch of the fault was sampled in traverse 2, but the next nearest samples are from more than 1 m away from the core. Traverse 3 did not display a single continuous fault core, but consisted of multiple anastomosing strands that were sampled along with the surrounding rock.

Representative thin sections from a particular area are used to describe the deformation at all locations. The thin sections from traverse 1 will be used to describe the characteristics of the fault core and the variability of microstructures in the damage zone adjacent to the core, whereas the thin sections from traverse 2 will be mainly used to illustrate the changes that occur within the entire damage zone, as well as the microstructures present between the two stands of the Punchbowl fault. The thin sections from traverse 3 will only be discussed briefly, because the San Andreas fault may have resulted in overprinting of microscopic structures.

It is possible to use different traverses to demonstrate certain features or characteristics because all three of the traverses were quite similar microscopically. Photomicrographs will be used to display the various textures found in this study. All photomicrographs are with crossed polars and have a long dimension of 2 mm. The microscopic deformation will also be quantified, so as to better explain the spatial variability of the microstructures. The quantitative results will be presented in a manner similar to the mesoscopic deformation presented in the previous section so that a comparison of deformation at both scales can be made. A brief analysis of scanning electron microscope observations is included at the end of this section. The scanning electron microscope was used to assist in determining the textures of the fault core.

Qualitative Description of Deformation

The protolith of the Pelona Schist is a quartz-feldspar-mica-schist (Fig. 28a). The foliation is distinct, with thin (1-2 mm) layers of quartz and feldspar separated by layers of aligned mica sheets. It is not always possible to distinguish foliation from fractures along thin mica sheets. The quartz and feldspar grains contain some fractures,

which are dominantly intragranular, and the quartz grains have an undulatory extinction at greater than 100 m from the fault core. The undulatory extinction is probably a signature of deformation during late Cretaceous metamorphism. In the undeformed region 100 m from the fault core in traverse 3, some intragranular fractures, small faults, and a cataclasite band are observed in the rocks.

Closer to the fault core, the foliation becomes less distinct and fractures increase in intensity (Fig. 28). Microfractures are the most common deformation feature that was measured and it is present throughout the sequence of rocks. In the undeformed Pelona Schist, the fractures are mainly intragranular. At a distance of roughly 50 m from the fault core, the fractures become more pronounced and intergranular fractures become increasingly dominant. Between 35 and 70 m, fracturing is apparent in all grains, with the fractures in the micas and feldspars parallel to cleavage planes (Fig. 28b and c). The undulatory extinction in the quartz grains becomes slightly more pronounced in this region as well.

Within 50 m of the fault core, more veins are apparent in the rocks at a microscopic scale. In some examples, slip has occurred along a calcite vein, which is evidenced by a dark, aphanitic band along one side of the vein (Fig. 28d). The structures within the vein are similar to those seen by Logan et al. (1981), with elongated grains, a prominent fabric oriented along strike of the vein, and evidence of localized deformation. Slip localization along one side of the vein commonly occurs in experimental settings (Yund et al., 1990).

Figure 28e shows evidence of foliation-parallel slip along individual sheets of mica after the injection of small calcite veins. In the middle of the photomicrograph, the mica grain with the largest amount of slip is deformed, possibly illustrating an early

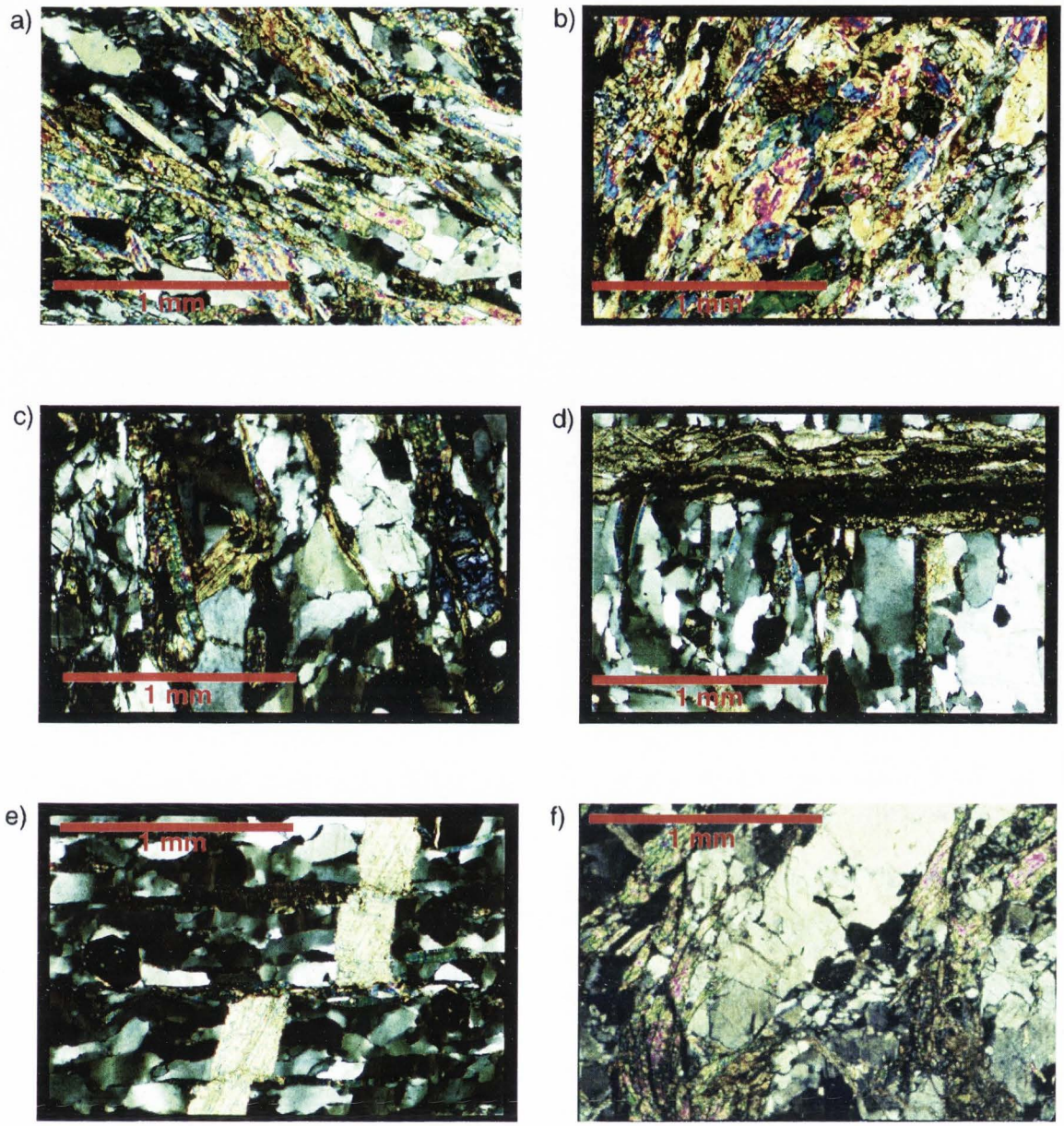

Fig. 28 Photomicrographs from the northern damage zone at traverse 2. Detailed descriptions are given in the text. All photomicrographs are with cross polars. All distances are given in relation to the north branch of the Punchbowl fault a) Undeformed Pelona Schist 101 meters north. b) 60 meters north. c) 37 meters north. d) 24 meters north. e) 24 meters north. f) 11 meters north.

stage of mica cataclasis. On the horizontal thin section, which is not shown, the slip on the mica sheets is predominantly right-lateral. This suggests that the rocks experienced slip after the injection of vein material.

The first strands of cataclasite appear at 60 m from the fault core in traverse 2, and at 50 m in traverse 1. They are thin (< 0.5 mm thick) bands of fine-grained foliated material, with rounded to angular mineral grains, and are mostly oriented sub-parallel to the Punchbowl fault with steep dips. At 20 to 30 m from the fault core, the cataclasite strands become thicker and more developed, comprising multiple anastomosing strands within a fine-grained matrix, although at this distance they are still not abundant. There are many instances where cataclasite zones have formed along veins, usually along the edge (Fig. 28d). Within 10 m of the fault core, the cataclasite zones become abundant. Within a meter of the fault core, cataclasite comprises more than 50% of the rock. The fault core is almost completely cataclasite. Close to the fault core, the cataclasite zones become well developed; they consist of anastomosing, black bands within a zone (0.2-1 mm thick) of crushed and altered rock.

Brittle deformation increases closer to the fault core. At 11 m, the fracturing becomes intense and is pervasive in all minerals (Fig. 28f). Amphibole crystals are a primary phase in the Pelona Schist as evidenced by the habit of the crystals in hand sample as well as in thin section. At 11 m from the fault core, the grain size has not been greatly reduced. Although there is localized grain-size reduction in the cataclasite, the majority of the grains are similar in size to those in the undeformed protolith. In some quartz grains the undulatory extinction is well developed and there appears to be incipient dynamic recrystallization and nucleation of subgrains (Fig. 28f).

Veins of laumontite, calcite, and quartz are quite abundant within 10 m of the

fault core. Further from the core, they are much less common, although there are a few areas of localized veining. There does not appear to be a preferred orientation to the veins. Microscopic vein densities are included with the overall deformation at the microscopic scale. The density of veins is greater in thin section than at the outcrop scale.

The deformation within 5 m to the fault core involves brittle grain-size reduction and alteration. The mica and feldspar present in the host rock begin to show increased amounts of alteration to a fine-grained (less than 0.1 mm), optically unidentifiable brown material. Within 2 m of the fault core, this alteration pervades most of the rock and every mineral, except quartz, is altered.

The greatest amount of the microscopic deformation occurs within 1 m of the fault core, where the rock is mainly a fine-grained (most grains less than 0.1 mm), optically unidentifiable material crosscut by cataclasite bands and veins (Fig. 29). Locally, there are grains of isolated, intensely fractured quartz that are greater than 1 mm (Fig. 29c); however, these are rare. The large quartz grain shown in Figure 29c is brittlely fractured and has a well developed cataclasite zone along its edge.

Within 1 m of the fault core, the cataclasite bands become thicker, more foliated and continuous, and often anastomose (Fig. 29a, b, and c). They contain wispy vein fragments and small clasts of quartz, feldspar, and mica. At 35 cm from the fault core, the majority of the grains are less than 0.3 mm in diameter. The fine-grained matrix appears foliated at the mesoscopic scale, but based on thin section analysis there is often no well developed fabric (Fig. 29a). Twenty-five cm north of the fault core, there is incipient development of a foliated cataclastic texture at a high angle to the mica sheets (Fig. 29b). Fragments of the mica sheets are chipped off, in what appears to be catacla-

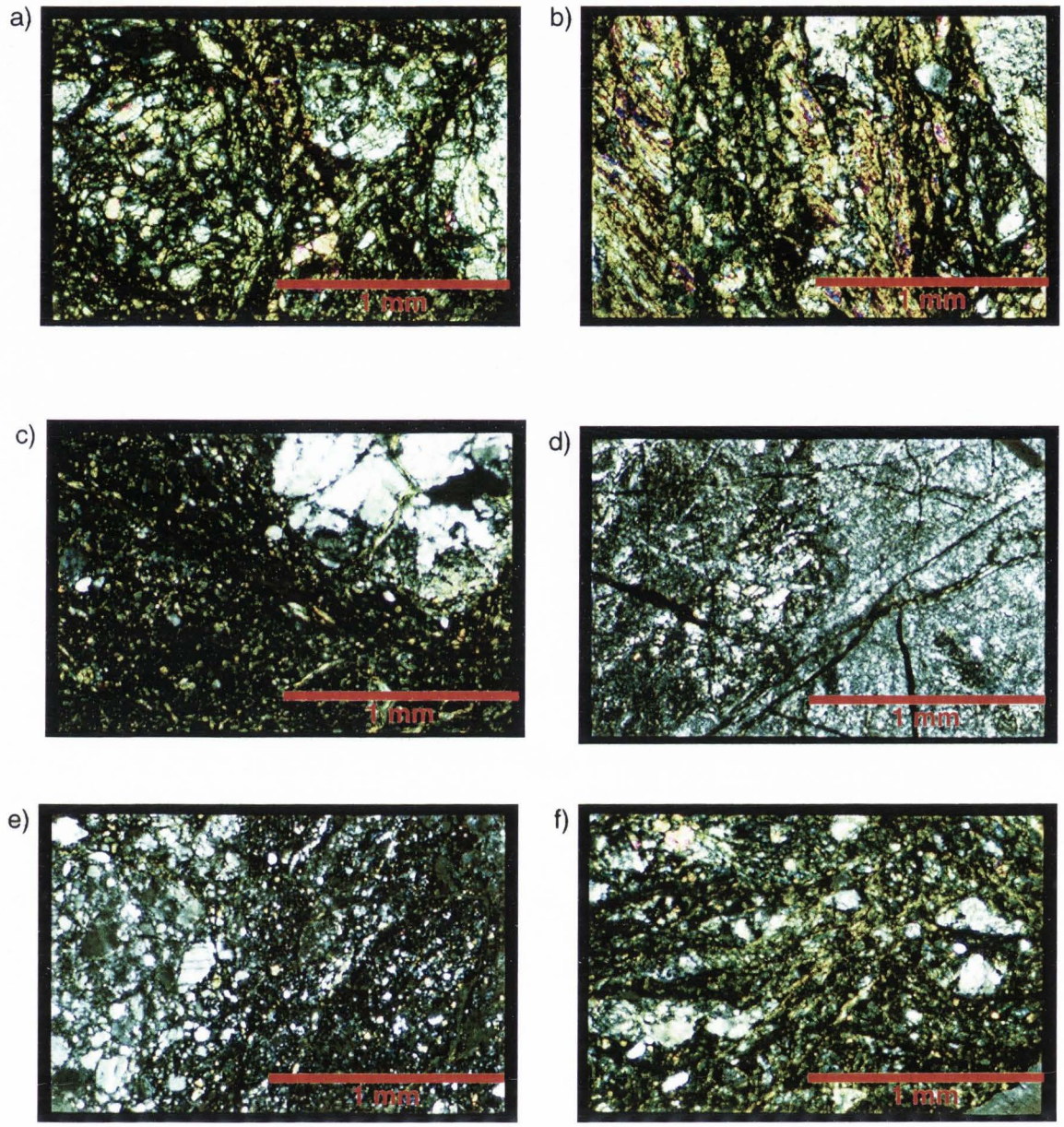

Fig. 29 Photomicrographs from the damage zone within 1 meter of the fault core at traverse 1. Detailed descriptions are given in the text. All photomicrographs are with cross polars. All distances are given in relation to the north branch of the Punchbowl fault. a) 35 cm north b) 20 cm north c) 10 cm north d) Fault core e) Fault core f) 10 cm south.

sis of phyllosilicate minerals along foliation.

None of the grains entrained within the cataclasite bands in the damage zone show evidence of rotation, such as tails, precipitation in the lee parts of grains, or "rollups" around the grains (Fig. 29b and c). This suggests that the rate of cross-sectional flow in the cataclasite is uniform, with little differential entrainment. A smoothly varying simple shear across the cataclasite zone may result in little rotation of clasts within a cataclasite (J.P. Evans, personal communication, 1996).

The fault core is dominated by a very fined-grained ultracataclasite, with few grains larger than 0.2 mm (Fig. 29d and e). The fined-grained matrix in the core appears to be responding as a continuous mass and is fractured much like the individual mineral grains farther from the core (Fig. 29d). The core contains disarticulated veins and cataclasite bands, indicating multiple episodes of deformation (Fig. 29e). No systematic crosscutting relationships exist between veins, fractures, small faults, and cataclasite bands, suggesting that there are multiple periods as well as mechanisms of deformation associated with faulting (Fig. 29e).

The fault core of the south branch at traverse 2 is microscopically similar to the north branch at traverse 1, and typically has a well-developed fabric or foliation, although it is not penetrative (Fig. 30). In Figure 30, photomicrographs are shown along with their inverted images, as this allows for easier recognition of the foliation and internal structures. Many parts of the core show a well-developed, predominant foliation parallel to the slip direction (Fig. 30a and c). However, locally there is some foliation that is oblique to this predominant foliation (Fig. 30b and d). This might suggest rotation of fault core material during slip in some parts of the fault zone, or may reflect formation of a second foliation during simple shear. Whereas the foliation was initially

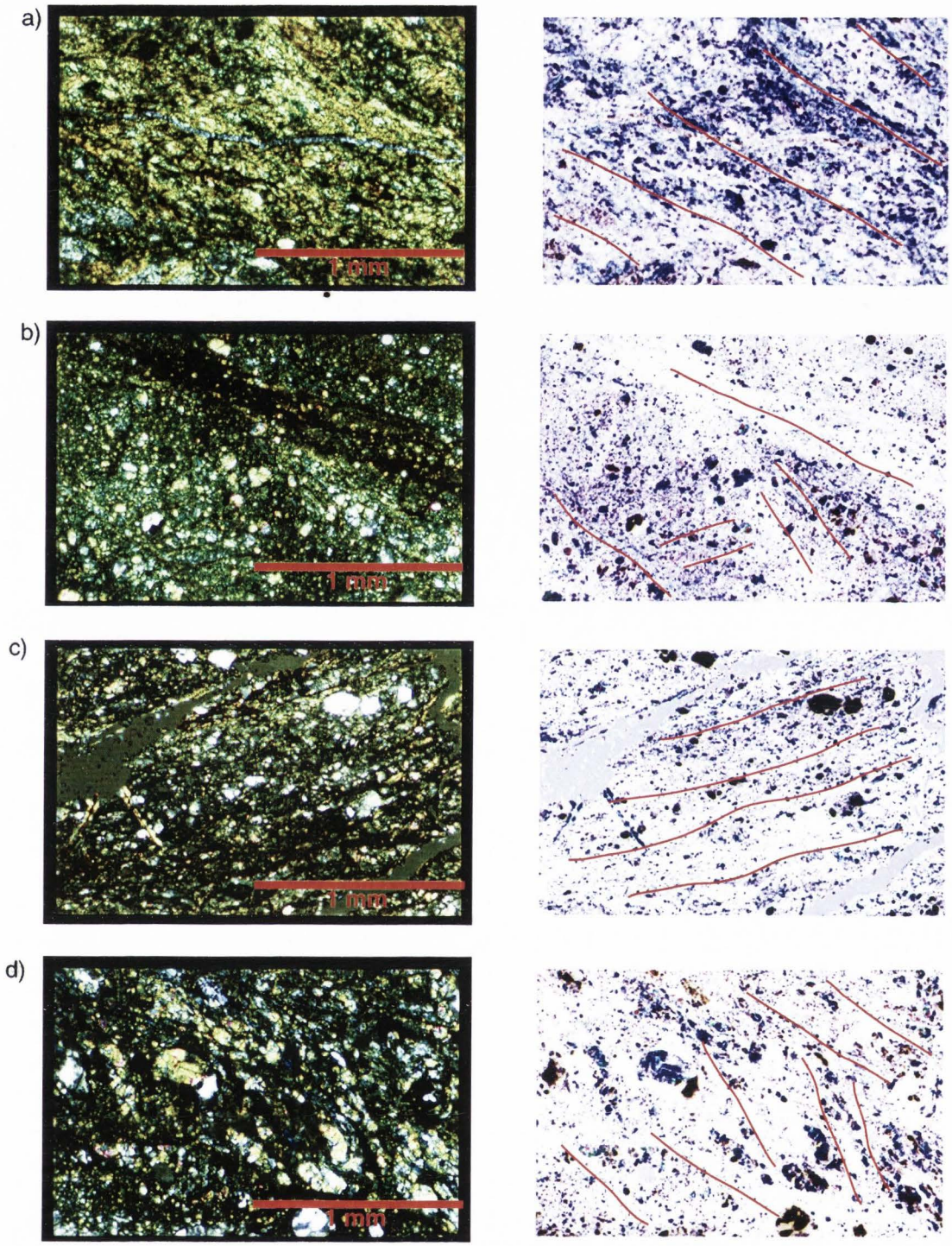

Fig. 30 Photomicrographs of the fault cores of the Punchbowl fault. All photomicrographs are with cross polars. Each photomicrograph is accompanied by a negative image, which allows for easier recognition of foliation. Red lines are drawn on negative images to indicate foliation orientation. a) Predominant, slip-parallel, foliation from traverse 1. b) Reoriented foliation from traverse 1. c) Predominant, slip-parallel, foliation from traverse 2. d) Reoriented foliation from traverse 2.

created parallel to the strike of the fault core by slip localization, rotation of portions of the fault core, possible as a result of simple shear localized elsewhere in the fault core, reoriented the foliation oblique to the predominant slip direction.

Between the two branches of the Punchbowl fault, the amount of deformation, as measured by the amount of fractures, alteration, and cataclasite bands, is greater than that in the undeformed Pelona Schist, but less than in the fault core (Fig. 31). Mica and, to a lesser extent, feldspar grains are altered between the two branches. Most of the deformation occurred by intra- and intergranular fracturing, alteration, formation of cataclasite, and veining (Fig. 31a, b, c, and d). Multiple episodes of veining occur in the rocks between the two branches (Fig. 31d) as well as well-formed cataclasite and ultracataclasite bands, which are sometimes crosscutting (Fig. 31b). The grain size between the two branches is greater than that found directly adjacent to and within the fault core. The alteration and deformation increase closer to the south branch of the Punchbowl fault.

Two meters south of the southern fault core at traverse 2, the rocks are quite deformed, but do not contain as much cataclasite as the fault core of the south branch (Fig. 31e). The rocks 27 m south of the fault core are relatively undeformed Pelona Schist (Fig. 31f). These undeformed rocks are closer to the fault core than the undeformed rocks north of the north branch of the Punchbowl fault.

The deformation is almost entirely brittle at greater than 5 m from the fault core, mainly through fracturing and cataclasite formation. There is little evidence of alteration or plastic deformation farther than 5 m from the core. Micro-faults are also rare and only occur locally at greater than 5 m from the fault core, whereas veining is sporadic and localized. Adjacent to the fault core, there is still evidence of fractures, mostly

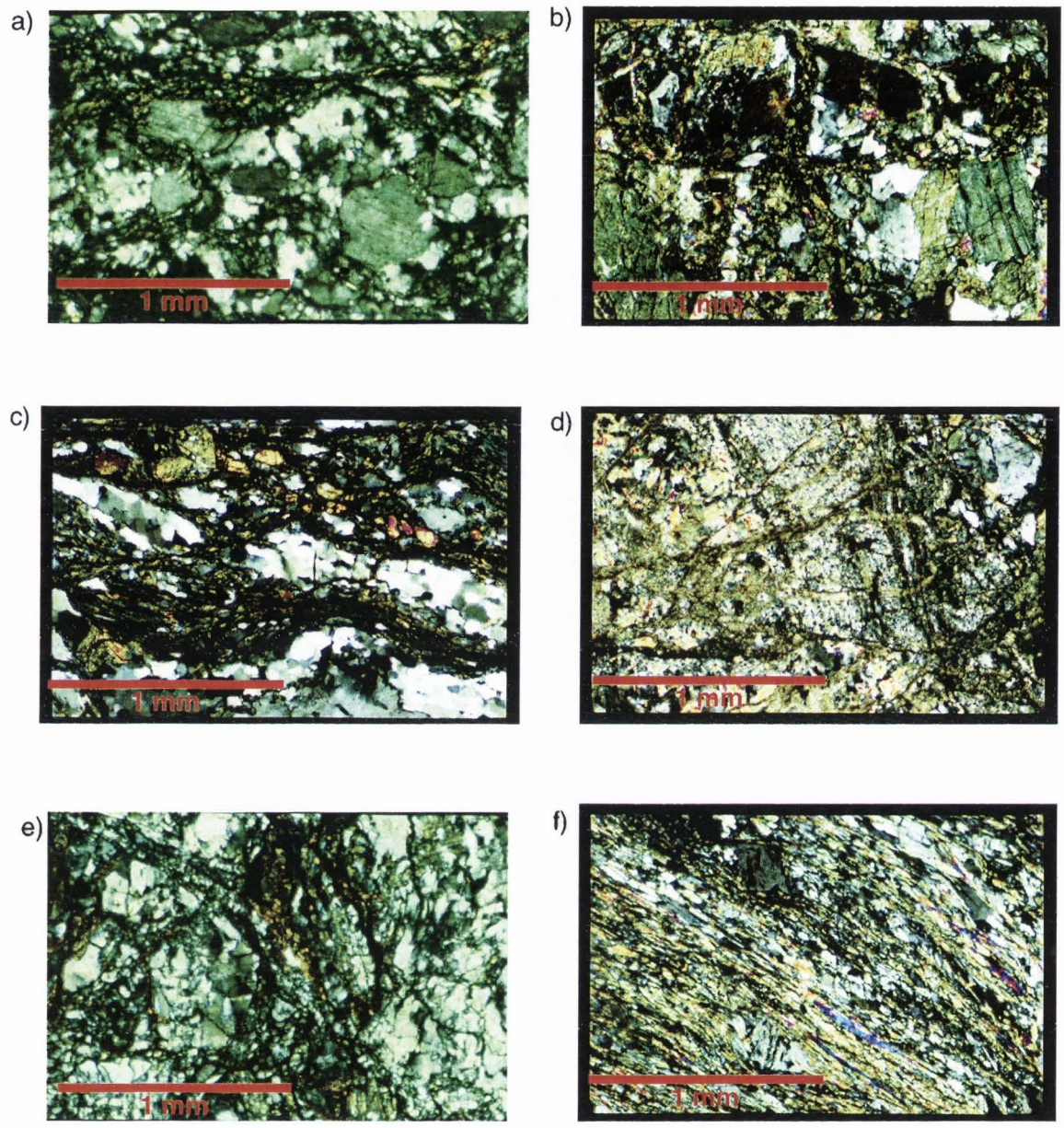

Fig. 31 Photomicrographs from the intrafault region and south of the southern fault core along traverse 2. Descriptions are given in the text. All photomicrographs are with cross polars. All distances are given in relation to the south branch of the Punchbowl fault. a) 54 meters north. b) 23 meters north. c) 9 meters north. d) 6 meters north. e) 2 meters south. f) 27 meters south.

in the quartz grains, as this is the only constituent that has not altered to a fine-grained matrix. The fine-grained matrix close to the core appears to be responding as a continuous mass, and is fractured much like the individual mineral grains farther from the core.

Closer to the fault core, the textures of the samples indicate that fluids are a major factor in the faulting process. This is apparent by the veining associated with the fault core, as well as the increased amount of alteration within 5 m of the fault core. The zones of alteration around the cataclasite bands suggest that these bands may be conduits for fluid migration.

Scanning Electron Microscope Analysis

The microstructures and deformation mechanisms of the very fine-grained ultracataclasites in the fault core were examined by back-scattered scanning electron microscopy. The textures in these high-magnification images (Fig. 32) consist of spaced foliation planes, subparallel alignment of platy grains, irregular tubes (Fig. 32a), and euhedral grains. At high magnification (1000X), subrounded quartz grains approximately 30 mm long embedded in a matrix of < 5 mm platy grains are apparent (Fig. 32b). The zone of platy grains may define anastomosing patterns in places, but other regions of the fault core reveal an amorphous texture (Fig. 32c). The foliated structures revealed at the SEM scale show that brittle fracture and cataclasis may give way to layer-silicate-dominated slip, in which the larger grains are in places mantled by the folia along which slip occurs (Fig. 32c). The amorphous textures may be the result of slip-induced processes, or may be the result of postslip healing (Chester et al., 1993).

a)

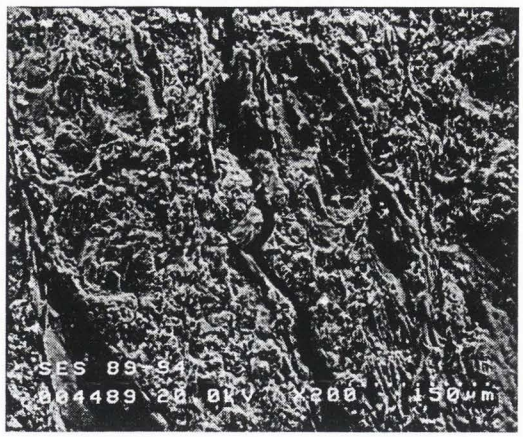

b)

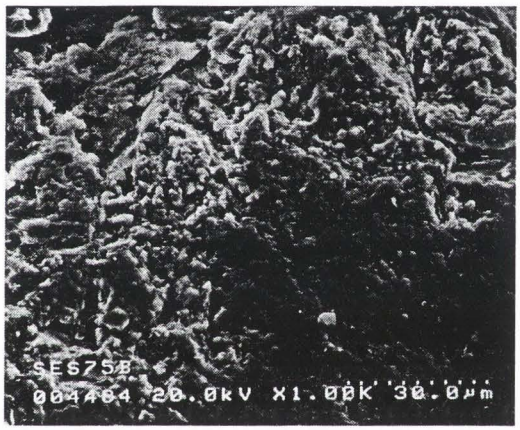

Fig. 32 Scanning electron microscope images of Punchbowl fault core. Samples are from the north branch core exposure in traverse 1. a) Foliated fabric of with platey grains. Magnification is 200X. b) Dark region is a region of increased density, most likely quartz. Magnification is 1000X. c) Stereo-pairs show euhedral quartz grains mantled by platey, fine-grained phyllosilicates.

c) 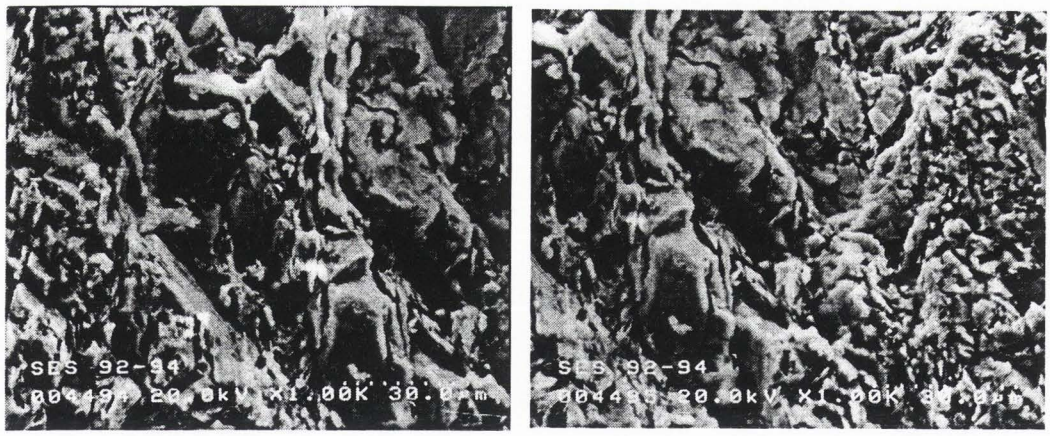

Fig. 32 Continued.

Quantitative Description of Deformation

Microscopic densities of damage elements were quantified by counting the cumulative number of damage elements that intersected the petrographic microscope crosshairs with the 4X objective sampled at 20 random points on the thin section. The random points were generated by using a random number generator to provide coordinates for 20 points on a graduated microscope stage. The densities are all given in number of damage elements per millimeter.

As in the macroscopic observations, the fault zone is divided into three distinct portions: a discrete fault core surrounded by a damaged zone within the undeformed protolith. In all three traverses, the microscopic deformation is low at 100 m from the fault core. As the fault core is approached, there is an increase in deformation (Fig. 33). The microscopic densities that were measured include microfractures, slip surfaces, veins, and cataclasite bands, but not alteration or grain-size reduction. Alteration was not quantified and grain-size reduction is presented separately.

The increase in microscopic deformation begins at roughly 40 m from the fault

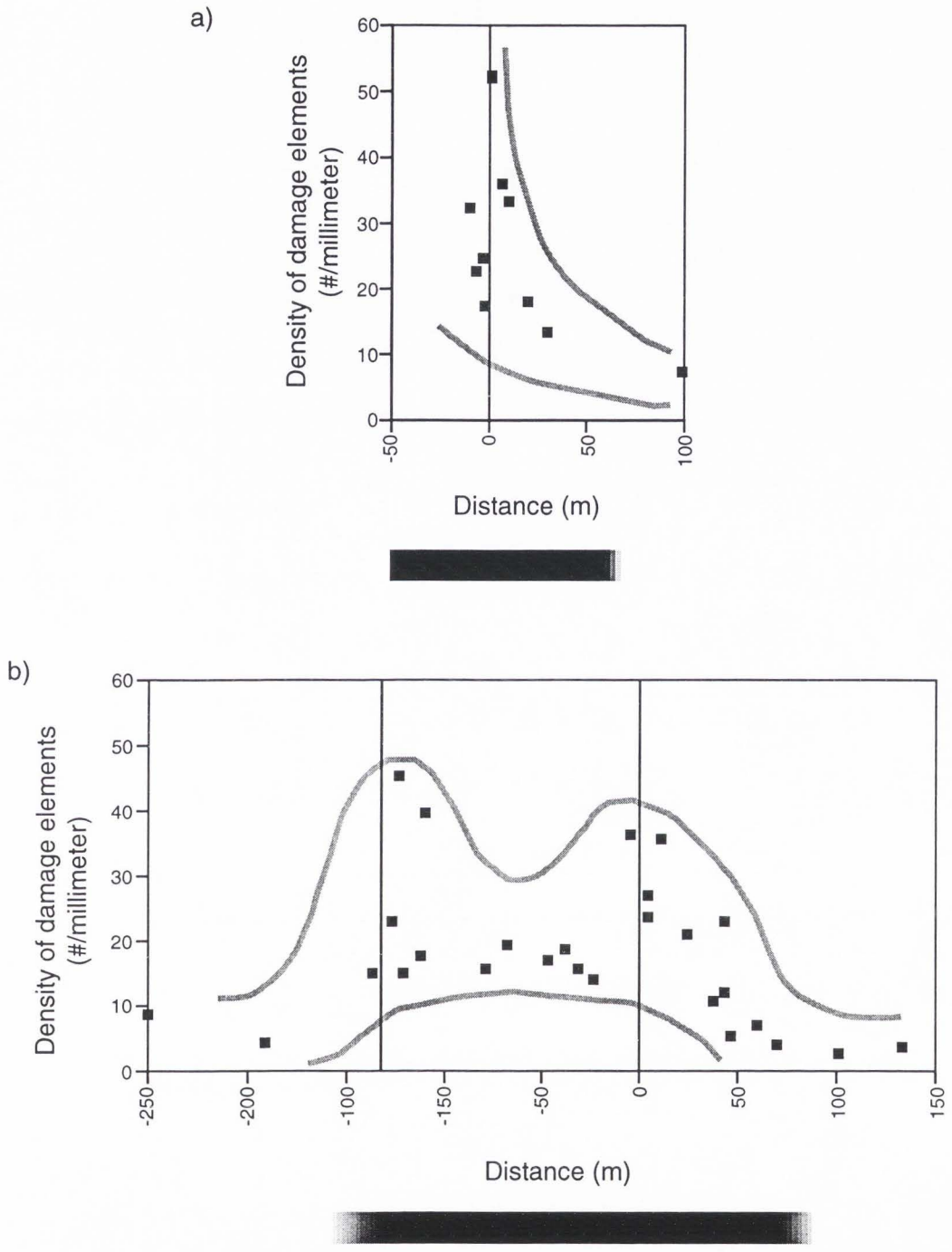

Fig. 33 Densities of microscopic damage elements plotted with respect to the distance from the fault core. Solid lines indicate the locations of fault cores of the major strands of the Punchbowl fault. Subsidiary faults are indicated by dashed lines. Grey lines outline the maximum and minimum deformation ranges measured. The bar beneath each graph shows the extent of the damage zone. a) Traverse 1. b) Traverse 2.

core and the total amount of microscopic deformation near the fault core is on the order of 5 times greater than in the undeformed protolith (Fig. 33). The exact location of the microscopic damage zone/protolith contact is difficult to determine, similar to the macroscopic damage zone/protolith contact (Fig. 15). There is an increase in the microscopic deformation 50 m north of the north branch of the Punchbowl fault at traverse 2 associated with a subsidiary fault (Fig. 33b).

The microscopic deformation between the two strands of the Punchbowl fault is up to 5 times as high as in the undeformed protolith (Fig. 33b). Between the strands of the Punchbowl fault at both traverses, the microscopic deformation is invariably less than it is in the damage zone adjacent to the fault core. Within 1 to 5 m of the fault core, much of the fracturing becomes masked by the other modes of deformation and alteration, which results in an underrepresentation of microscopic deformation adjacent to the fault core (Fig. 33b).

The microscopic deformation in the fault core, primarily a fine-grained cataclasite, is difficult to quantify. The fine-grained matrix that comprises the majority of the fault core appears to have experienced repeated cataclasis and does not display many brittle fractures. Mineral alteration cannot be quantified utilizing the same techniques that were used to describe the damage element density. Therefore, the amount of microscopic deformation that is present in the fault core is probably much greater than shown in Figure 33. Chester et al. (1993) also showed the apparent decrease in deformation at the fault core and suggested that it reflects repeated comminution and alteration.

The average grain size of the Pelona Schist is fairly constant beyond 10 m from the fault core (Fig. 34). Grain size is reduced from a mean value of 0.52 mm ±0.08 mm (95% confidence interval) at 32 m from the fault core to 0.32 mm ± 0.05 mm (95% con-

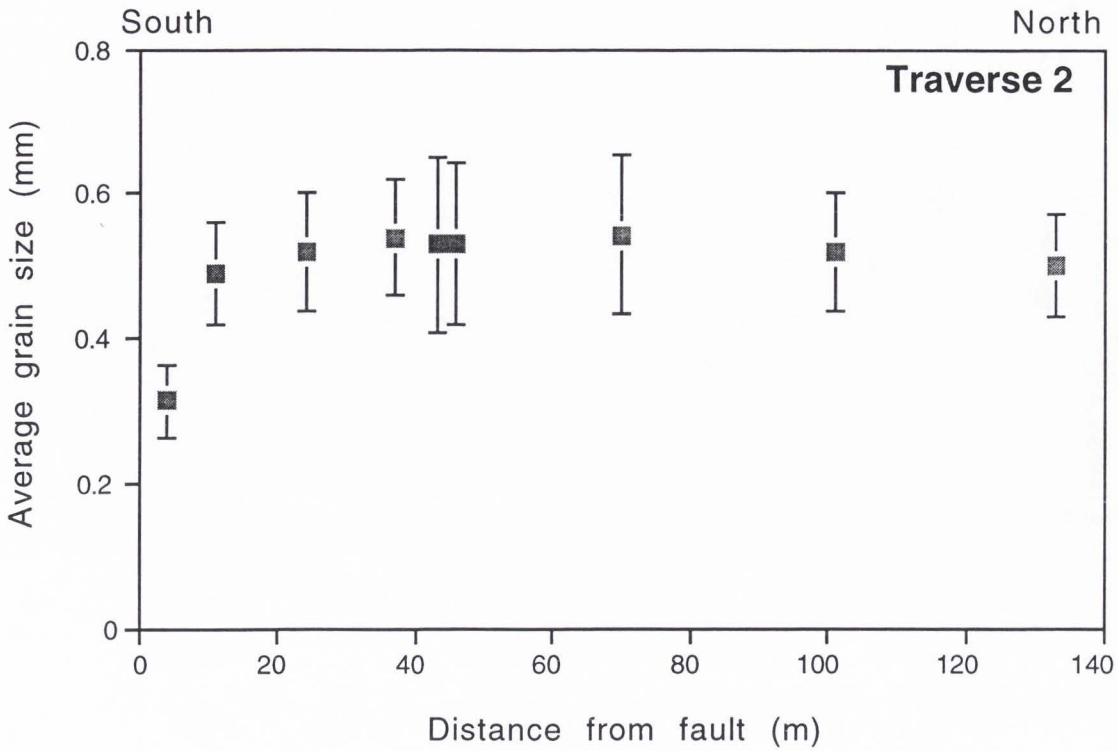

Fig. 34 Variation in grain size across the fault zone at traverse 2. Distances are from the north branch of the Punchbowl fault. Grain size was measured optically with a petrographic microscope. Error bars show one standard deviation of the measurements.

fidence interval) 4 m from the core. These values were obtained by measuring 100 random grains per thin section with a petrographic microscope. Grains smaller than 0.1 mm are not resolvable optically, so very fine-grained material is probably underrepresented and rare large grains (greater than 1 mm) skew the data somewhat. Grain-size reduction by brittle processes is accompanied by the alteration of feldspars and micas to a fine-grained (< 0.1 mm) optically unidentifiable brown material.

Figure 35 shows histograms of the grain sizes at four distances from the north branch of the Punchbowl Fault at traverse 2. Whereas all four histograms show a large dispersion in grain size, there is an increase in the number of grains less than 0.3 mm in

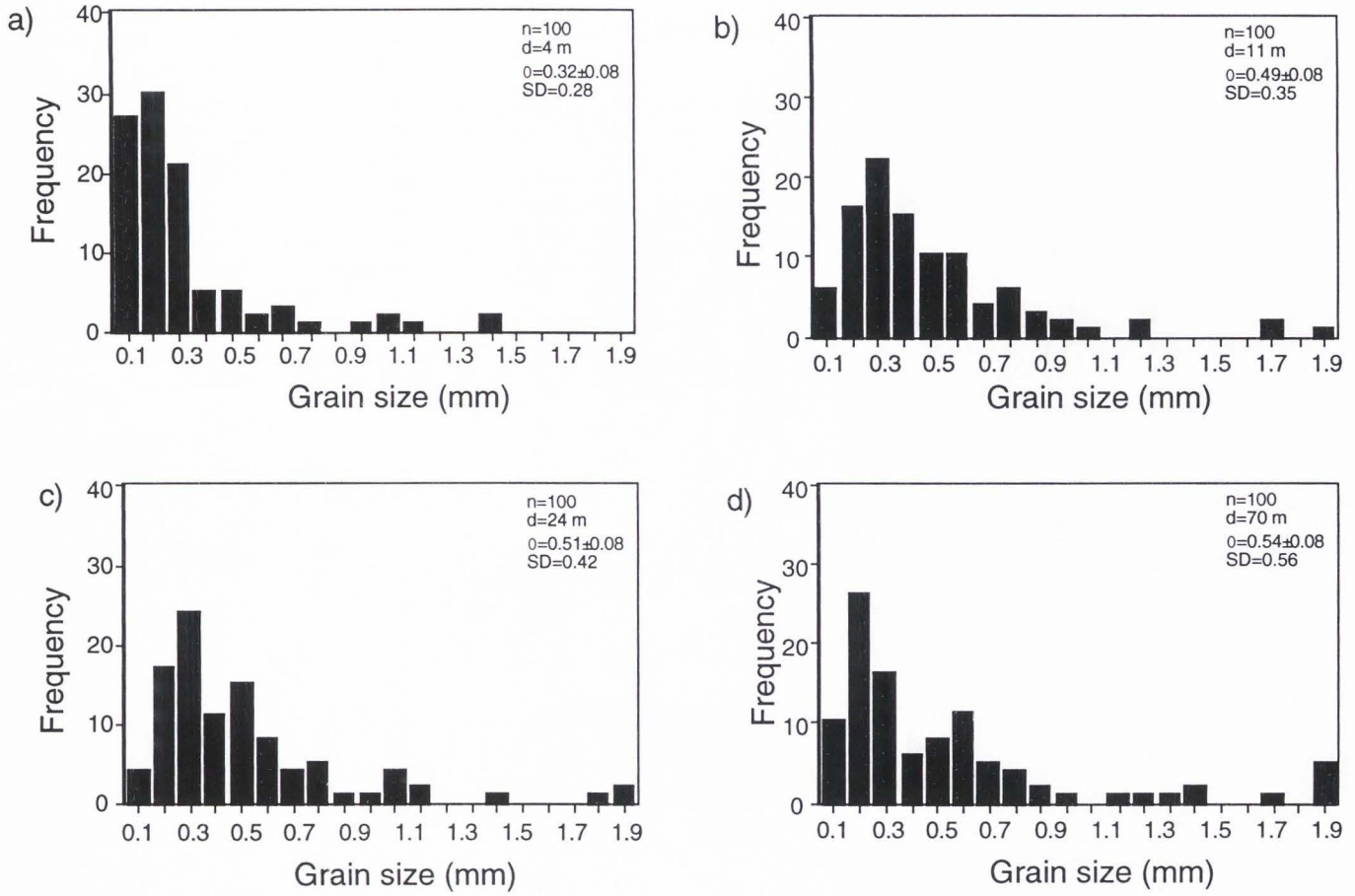

Fig. 35 Histograms of the distribution of grain size in four thin sections located at different distances from the fault core at traverse 2. The distance from the north branch fault core is indicated by the value for d. Grains smaller than 0.1 mm were placed in the 0.1 mm bin.

size within 4 m of the fault core. This increase in fine-grained material makes it difficult to determine the amount of other deformation features present in the thin sections adjacent to and within the fault core. This will lead to an underrepresentation in the amount of microscopic deformation close to the fault core.

GEOCHEMICAL AND MINERALOGICAL ANALYSIS

X-Ray Diffraction Analysis

Standard x-ray diffraction was used to determine the mineralogy of representative fault-related rocks at both traverses 1 and 2. Rocks north of traverse 1 consist of hornblende, albite, and clinochlore (Fig. 36a), consistent with a meta-basaltic composition (Best, 1982). The protolith south of the fault core consists of quartz, albite, and clinochlore (Fig. 36b), suggesting a meta-greywacke. The fault core and rocks immediately adjacent to the fault core consist of quartz, albite, ferroan or chromian clinochlore, ± epidote (Fig. 36c and d). The presence of clinochlore in these rocks is consistent with retrograde reactions of hornblende and actinolite (Laird, 1988). The general reactions suggested by the x-ray diffraction data at traverse 1 are that from a starting assemblage of quartz + albite ± actinolite ± epidote ± hornblende, fault-related reactions result in hydration and alteration of the Fe-Mg minerals, to produce quartz + albite + clinochlore ± epidote.

The x-ray diffraction pattern for fault-core samples at traverse 1 shows an abundance of subclay-sized grains, which is seen by the increased background noise (Fig. 36c and d). This increased background noise is common in clay-hydrous phase-rich rocks and suggests that the fault core at traverse 1 is a complex mixture of hydrous phases and protolith.

Analyses from traverse 2 are for samples across the southern branch of the fault, where the protolith consists of quartz + albite + muscovite ± graphite (Fig. 37a and b). Rocks from the fault core at this site consist of quartz, albite, and clinochlore, ± epidote (Fig. 37c and d). This assemblage in the fault core may occur by the reaction (Wintsch

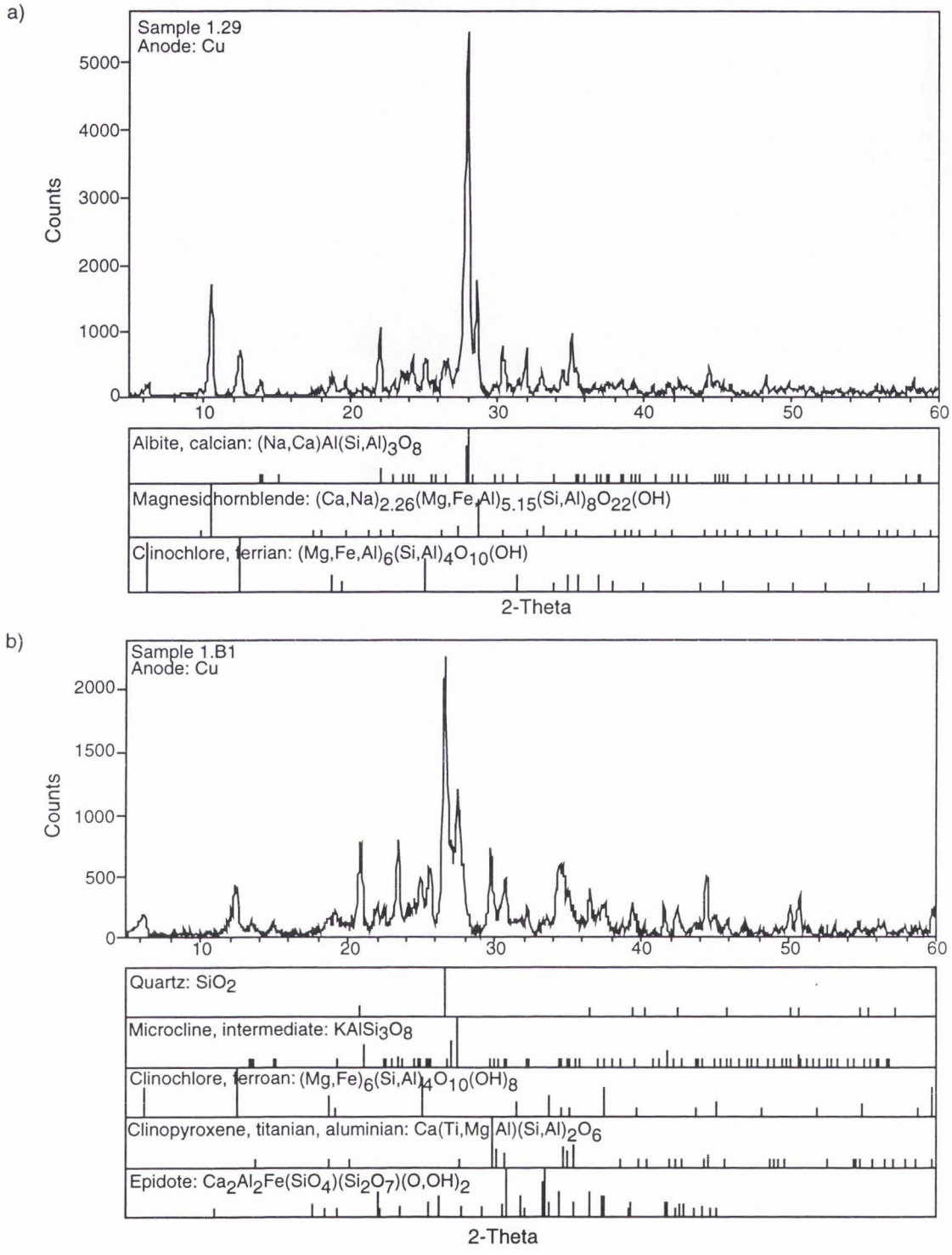

Fig. 36 X-ray diffraction patterns for rocks from traverse 1. The rectangles below the spectra indicate likely mineral matches and there respective peaks. a) 30 meters north of the fault core. b) 2 meters south of the fault core. c) Fault core. d) Fault core.

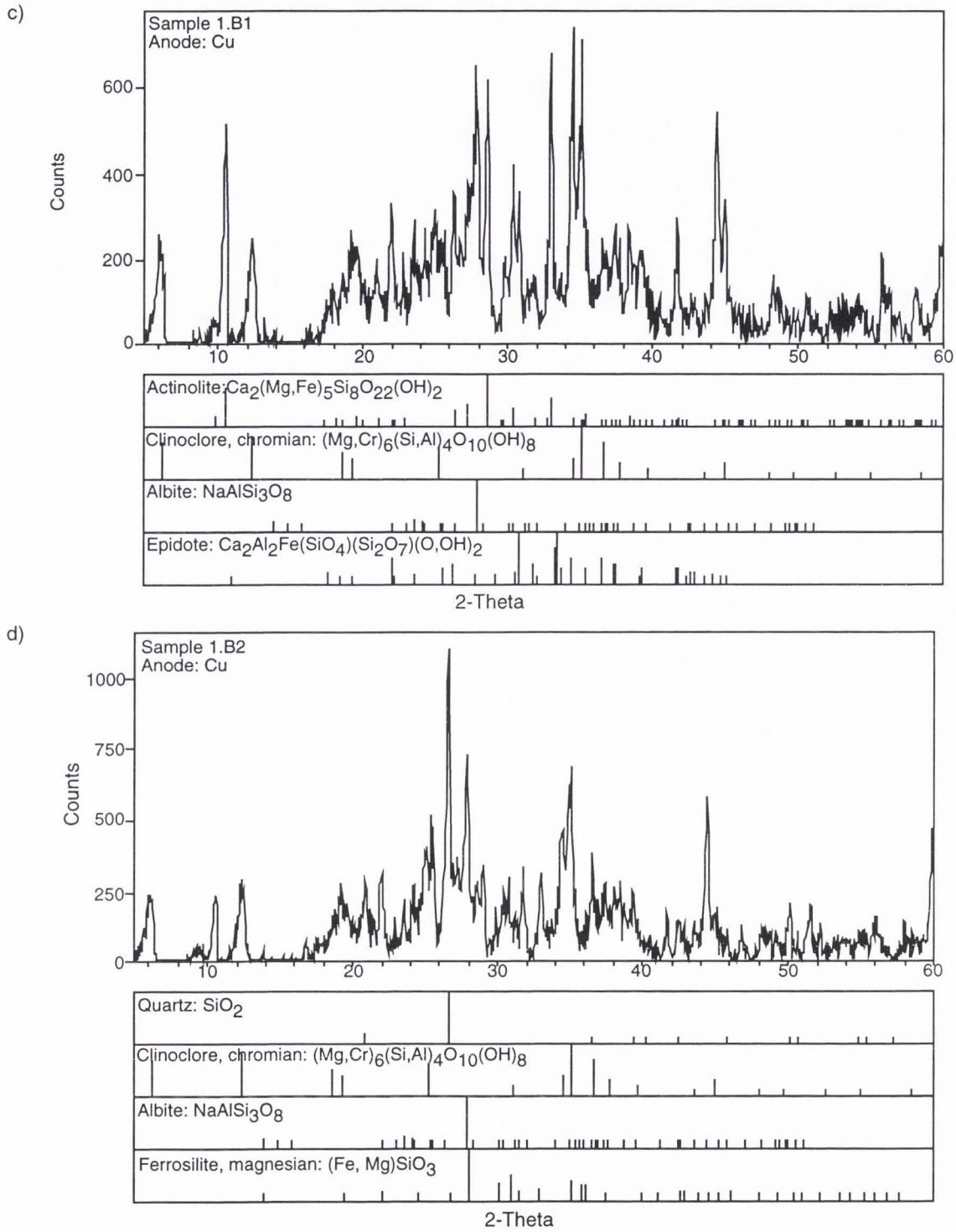

Fig. 36 Continued.

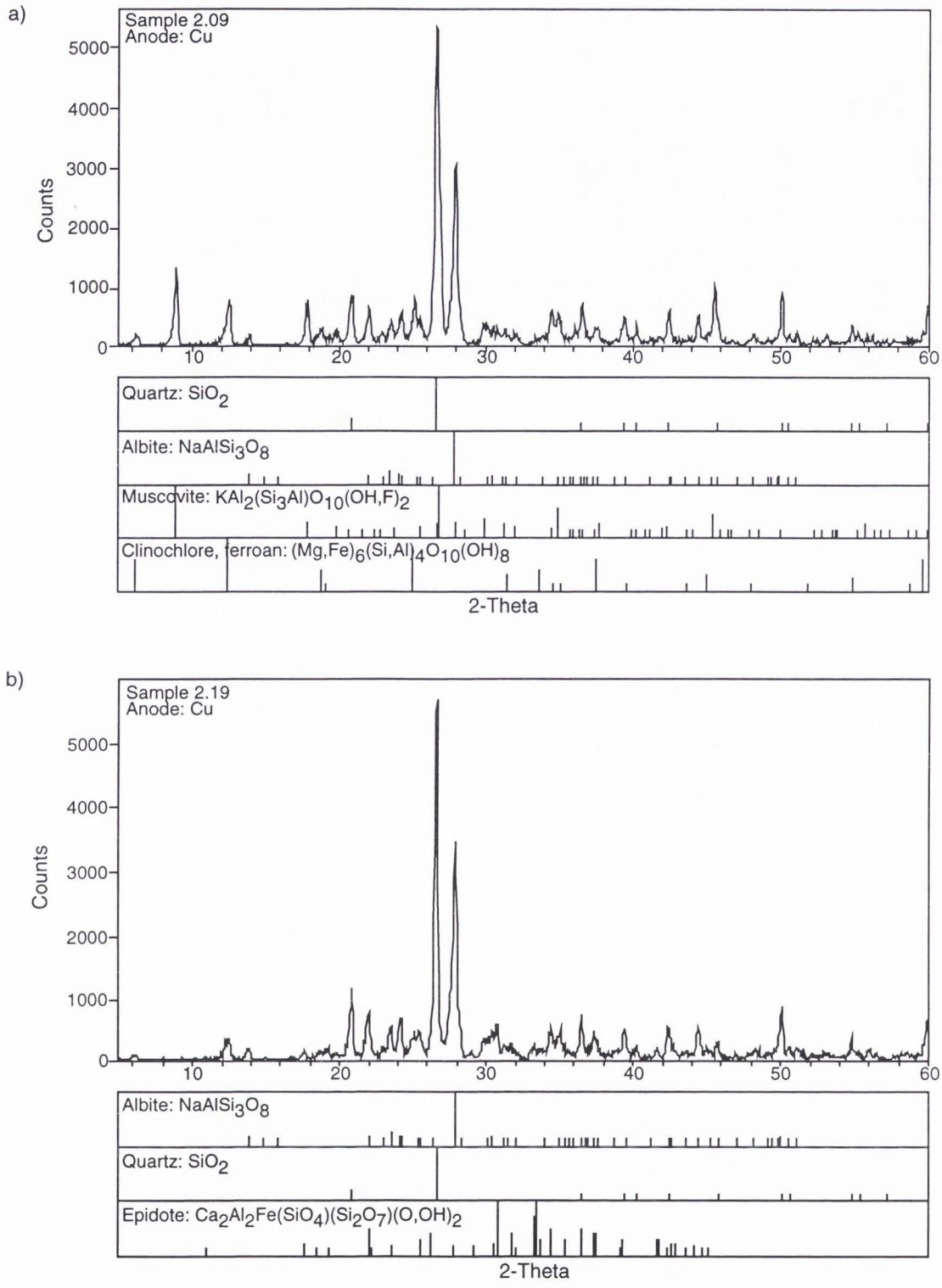

Fig. 37 X-ray diffraction patterns for rocks from traverse 2. The rectangles below the spectra indicate likely mineral matches and there respective peaks. a) Roughly 4 meters north of the northern fault core. b) Southern fault core. c) 2 meters south of the southern fault core. d) 4 meters south of the southern fault core.

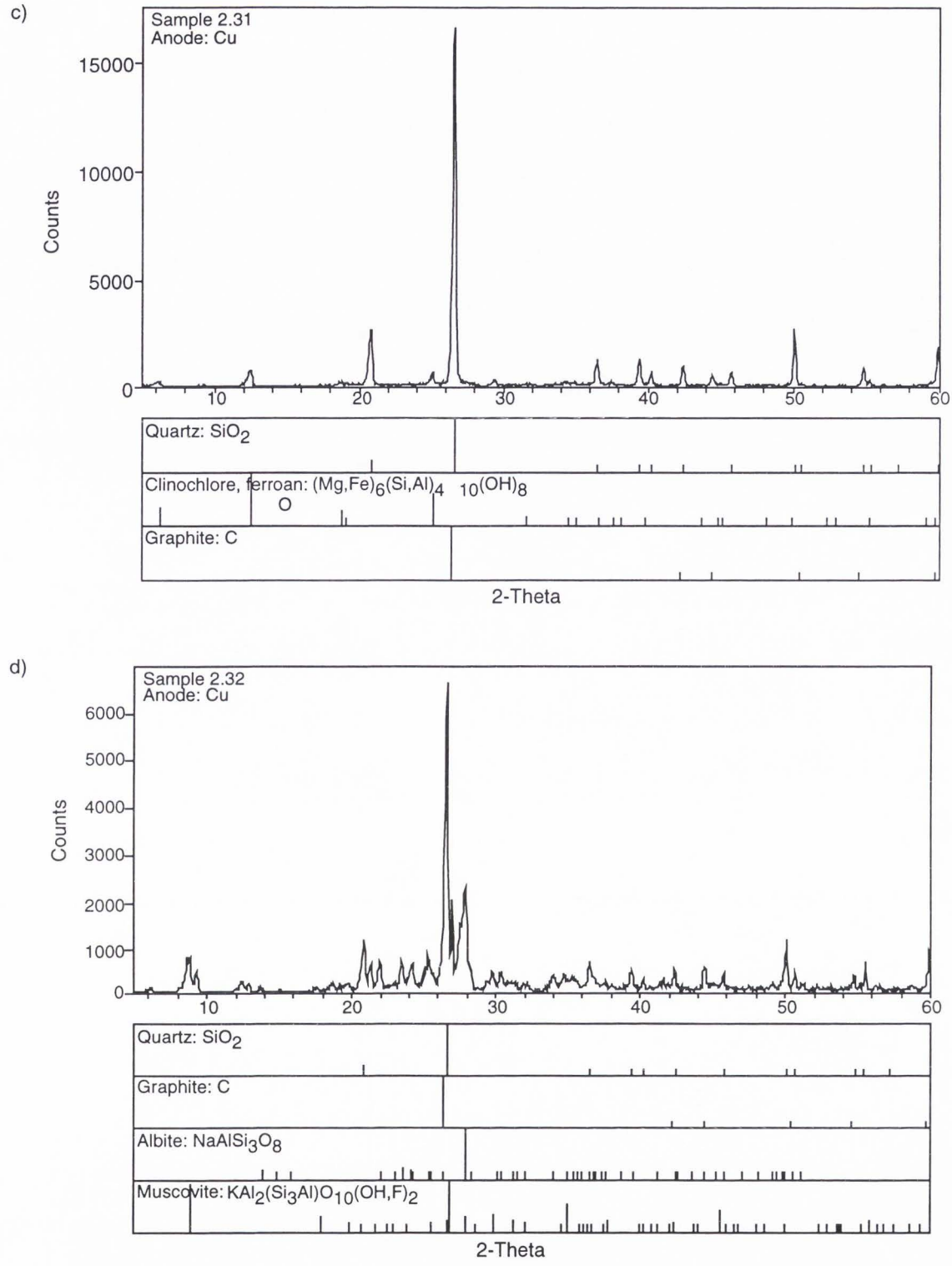

Fig. 37 Continued.

et al., 1995), which requires the addition of H_2O.:

$$2KAl_3Si_3O_{10}(OH)_2+15Mg^{++}+3SiO_2+24H_2O = 3Mg_5Al_2Si_3O_{10}(OH)_8+2K^{+}+28H^{+}$$

muscovite clinochlore

The Mg^{2+} for this reaction may be liberated from the alteration of Fe/Mg horneblendes. Liberated K^{+} in this reaction may be deposited in the damaged zone, as suggested by some of the high K^{+} values reported in the whole-rock analysis, or may reside within the fault core in K bearing amorphous polymers (J. Boettinger, personal communication, 1996). The reaction that produced the clinochlore in the fault zone requires the addition of H_2O to the fault core. This suggests that fluids were added to the rocks, possibly during faulting, to induce alteration.

The diffraction patterns for the fault core and damaged zone rocks at traverse 2 lack the background noise seen in traverse 1, indicating less clay in the fault core at traverse 2 (Fig. 37). If the fault-related processes are similar in the various fault cores, this may indicate that mineralogical or geochemical changes here were accommodated by at least a local transport of hydrous material out of the fault zone, which agrees with the volume losses recorded by the whole-rock analysis.

Whole-Rock Geochemistry

The whole-rock geochemical signature of fault-related rocks is probably the result of integrated processes during the slip history of the fault. Thus, the geochemistry provides insight into the evolution of the fault and the related rocks. Whole-rock analysis were made to determine chemical changes across the fault zone as well as along

strike. Similar analysis of fault zone rocks have been made by Evans and Chester (1995) and Goddard and Evans (1995).

The geochemical variations in the fault core of the rock will also record the influence of different rock types that will contribute to the chemical makeup of the fault core. The Punchbowl fault has over 44 km of right-lateral slip (Dibblee, 1968; Ehlig, 1981), involving a variety of rocks, from sandstones to schists, in the formation of the fault core. In addition, the Pelona Schist itself has a variable composition, from meta-greywackes to meta-basalts (Haxel et al., 1986). We attempt to examine the extent that local, which implies the rocks currently adjacent to the fault core, and regional, which includes the entire range of rocks that were adjacent to the fault core in the life of the fault, rock compositions influence the geochemical nature of the fault core.

Samples were collected for whole-rock geochemical analysis from each of the three traverses across the Punchbowl fault. The samples were ground to a fine-grained powder and sieved to less than 2 mm. Half of each sample was sent to XRAL Laboratories, Don Mills, Ontario, for whole-rock geochemical analysis and half was retained for x-ray diffraction. XRAL Laboratories measured the abundance of 11 major oxides by x-ray fluorescence. X-ray fluorescence analysis have a reported detection limit of 0.01 weight percent (wt. %; XRAL Laboratories, 1996). Data from the whole-rock geochemical analysis are presented in Appendix B.

Whole-rock geochemical samples are mostly from traverses 1 and 2. Eleven samples are from traverse 1, beginning 30 m north of the fault core and ending 7 m south of the fault core (Table B1 and B2). Thirty-four samples were analyzed from traverse 2 (Table B3), traversing the entire fault zone shown in Figure 5. Only seven geochemical samples were analyzed along traverse 3, mainly in the damage zone south of

the Punchbowl fault, due to the complexities associated with this location.

The sum of the measured oxides is low (lowest value is 97.7 wt. %), even including loss on ignition (LOI), for many of the samples from both traverse 1 and traverse 2. Jacobson (1980) also showed low sums for the major oxides (94.3 to 95.6 wt. %) for samples that he measured in both the Blue Ridge and East Fork areas. He did not include values for P_2O_5, Cr_2O_3, and LOI in his sum calculations and does not discuss the values that were calculated. The data in Haxel et al. (1986) have calculated sums that are between 99.4 and 99.8 wt. %, which are close to the desired value of 100 wt. %. The data in Haxel et al. measured both FeO and Fe_2O_3, whereas this study reports the total amount of iron as Fe_2O_3.

XRAL retested the samples from traverse 1 to determine if the low calculated sums are the result of a systematic measurement error. However, similar values were reported for the second set of analysis. To help determine what may account for the low sums, samples from traverse 1 were also tested for trace element abundance and percentage of carbon and sulfur. Carbon is present as graphite in portions of the Pelona Schist (Jacobson, 1980) as well as in calcite. The total carbon and sulfur adds up to less than 0.2 wt. % in all the samples measured. Neither of these two elements nor the trace-element abundances can account for the low calculated sums. The most likely reason for the low calculated sums is a low estimate of the loss on ignition value (XRAL Laboratories, 1996). The calculated sums were closest to 100 wt. % in the north branch fault core in both traverses. The core of the south branch of the Punchbowl fault also has a higher sum of oxides than the surrounding rocks, suggesting that the unanalyzed element(s) in the north branch of the Punchbowl fault is(are) not present in the south branch.

Figure 38 compares the whole-rock geochemistry of the protolith at all three traverses to geochemical data of the Pelona Schist in Dibblee (1961) and Haxel et al. (1986). The protolith north of the Punchbowl fault in traverse 1 is most similar in geochemistry to the meta-basalt reported by Dibblee (1961) from the Sierra Pelona which has a low a SiO_2 content with elevated CaO and MgO (Fig. 38a). The protolith from north of the Punchbowl fault at traverse 1 has a higher Fe_2O_3 abundance than the meta-basalt or any of the other rocks to which it was compared. The trace-element data from north of the Punchbowl fault at traverse 1 is less conclusive than the oxide analysis. The fault core haS similar Sr and Ba signatures to a meta-greywacke analyzed by Haxel et al. (1986), although the Zr and Rb data is similar to the meta-basalt (Fig. 38b). Yttrium was not reported by either Dibblee (1961) or Haxel et al. (1986). Based on the oxide analysis, mesoscopic textures, and mineral assemblages, the protolith north of the fault in traverse 1 is probably a meta-basalt, and the rocks south of the fault core at traverse 1 are likely to be metagreywackes.

The protoliths both north and south of the Punchbowl fault in traverse 2 are similar to the meta-greywacke in Jacobson (1980) and Haxel et al. (1986), especially in the SiO_2, CaO, and MgO content (Fig. 38a). There is also some aplite that is located between the two branches of the Punchbowl fault in traverse 2. The rocks samples south of the Punchbowl fault at traverse 3 are similar to the rocks south of the Punchbowl fault at traverse 2, and are therefore thought to be meta-greywackes as well (Fig. 38a).

Figure 39 shows spider diagrams comparing the geochemical abundances of oxides in the undeformed protolith and the damage zone with the fault core in all three traverses. For traverse 1, there is little variation in the chemical composition between

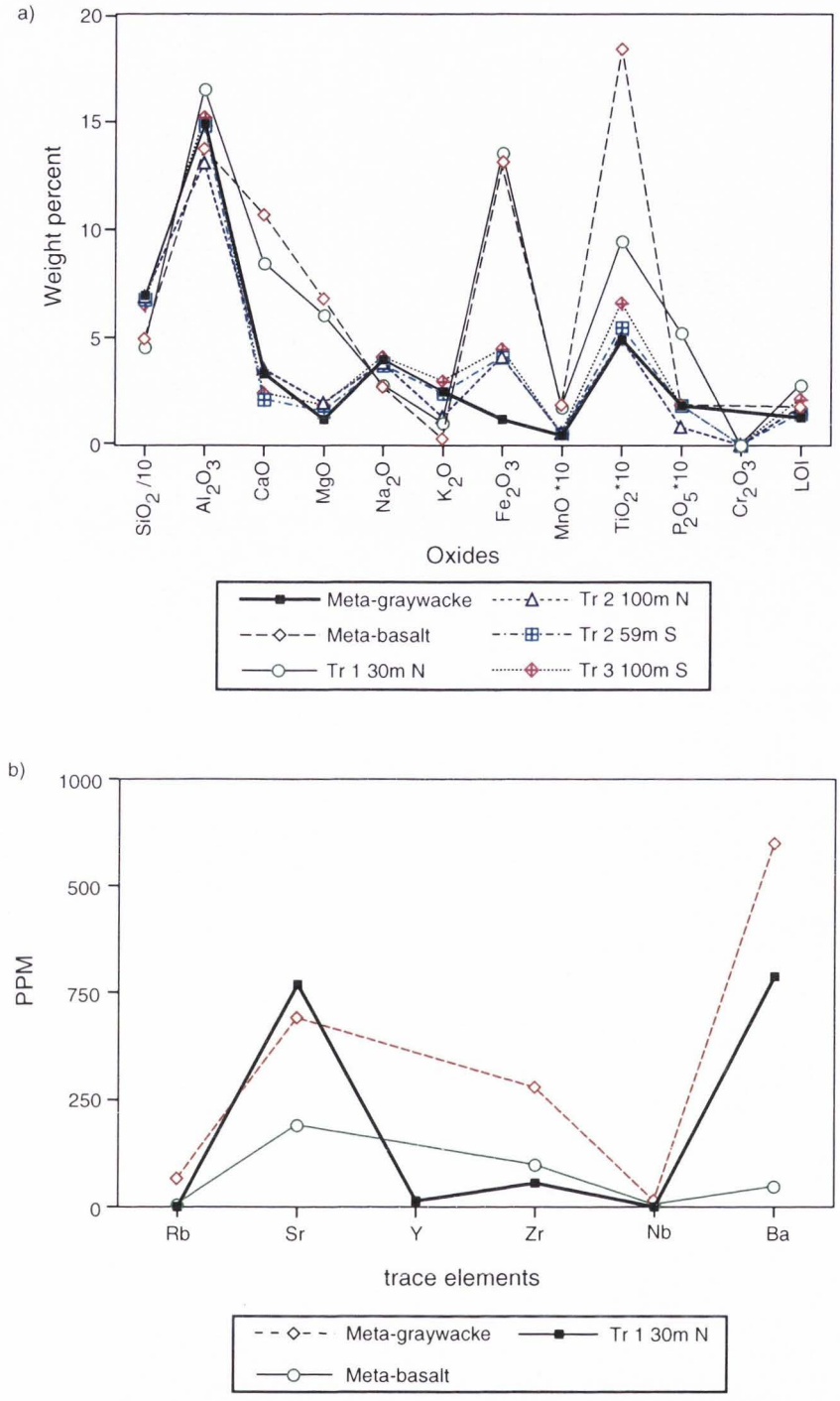

Fig. 38 Comparison of oxide and trace element abundances from the protolith at traverses 1, 2, and 3 with values previously reported by others. The meta-greywacke data are from the Gavilan Hills region (Haxel et al., 1986). The meta-basalt data are from the Sierra Pelona (Dibblee, 1961). Oxides with low values were multiplied by 10 and SiO_2 was divided by 10, which allows for a better comparison of data. a) Oxides and loss on ignition. b) Trace elements.

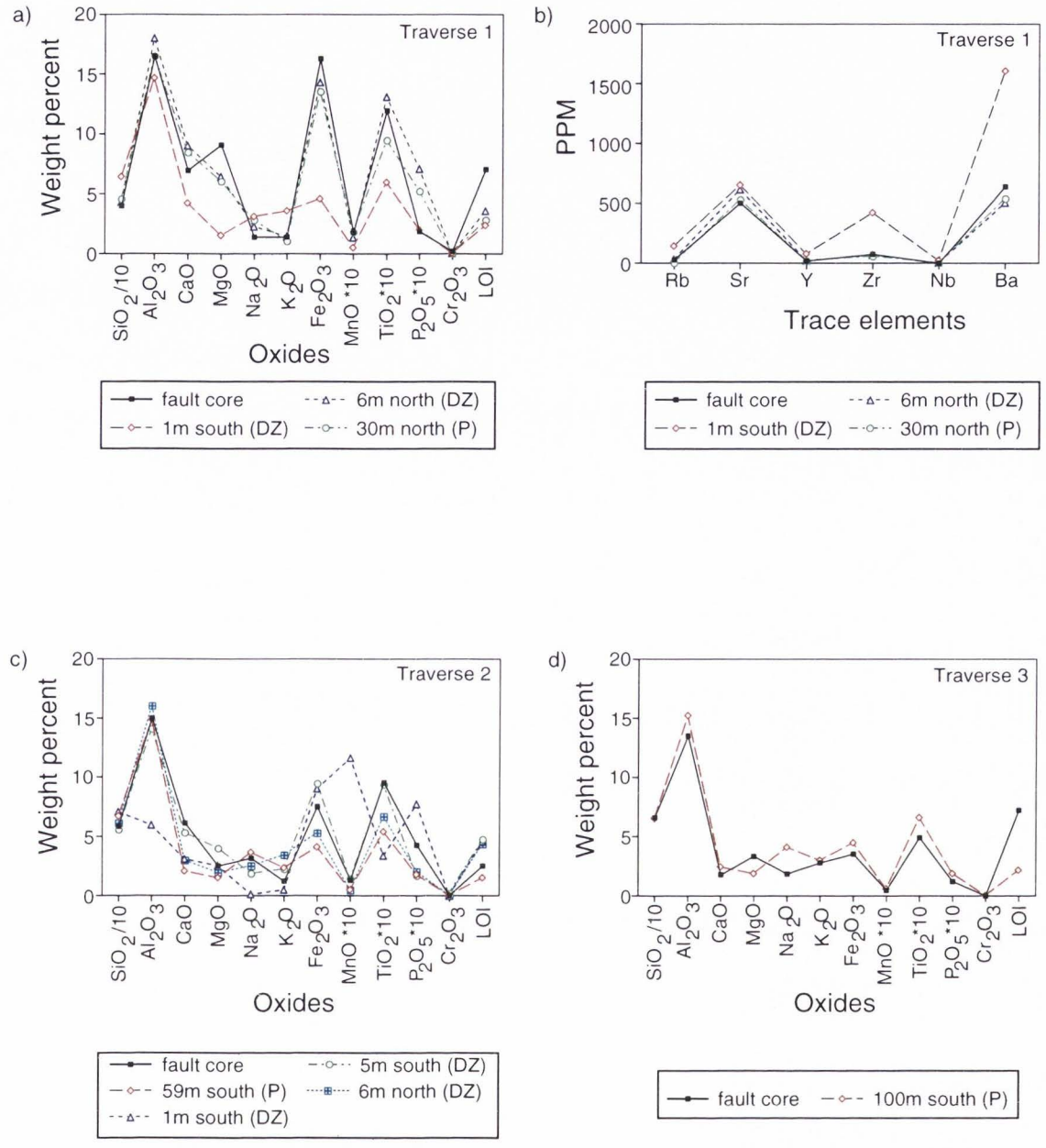

Fig. 39 Comparison of the geochemical composition of the fault cores with adjacent rocks and protolith. Trace elements and oxides with low values were multiplied by 10 and SiO_2 was divided by 10, which allows for a better comparison of data. Samples considered to be from the protolith are designated by (P) while those from the damage zone are designated by (DZ). a) Major oxides at traverse 1. b) Trace elements at traverse 1. c) Major oxides at traverse 2. d) Major oxides at traverse 3.

the protolith and fault core (Fig. 39a and b). There are no geochemical analysis for any samples farther than 30 m from the fault core, so these protolith samples may have experienced some fault-related deformation and alteration. The fault core is chemically similar to the damage zone, with the exception of an enrichment of MgO and a depletion in P_2O_5. The fault core also deviates from the protolith north of the fault core in the amount of loss on ignition (LOI), which is twice as high as any other rocks from traverse 1. Rock collected 1 m south of the fault core is enriched in SiO_2, Zr, and Ba, and depleted in Fe_2O_3 and MgO relative to the rocks in the fault core.

For traverse 2, only the fault core of the south branch of the Punchbowl fault was analyzed, as it was not possible to sample the northern fault core (Fig. 39c). The oxides in the damage zone samples south of the fault core show little variation from the protolith composition with proximity to the fault core. The sample 1 m south of the core is depleted in Al_2O_3 and TiO_2 but relatively enriched in MnO and P_2O_5. The fault core is geochemically different from the rocks on either side, although the fault core is more similar in geochemical characteristics to the rock that is located 6 m north of the core. Unlike the other fault cores studied, the southern fault core at traverse 2 was not enriched in hydrous components, which is measured as loss on ignition (LOI), relative to the adjacent rocks. This suggests a possible difference in the role of fluids during faulting between the two main branches of the Punchbowl fault. However, the rocks adjacent to the core do show an increase in LOI over the protolith values (Fig. 39c).

For traverse 3, the core and the protolith are similar, except for a small depletion in Al_2O_3, TiO_2, and Na_2O and an enrichment in MgO (Fig. 39d). The amount of LOI is also higher in the fault core, similar to traverse 1.

These comparisons of the geochemistry of the damage zone (or protolith) rocks to the fault core are given with the assumption that the local protolith, the rocks currently adjacent to the fault core, are all that contributed to the composition of the core. This is unlikely, as the Punchbowl fault has experienced over 44 km of slip, with much of that along the fault cores. Therefore, the rocks that encountered and interacted with the fault core are quite variable. Not only does the Pelona Schist have a wide range of compositions, but other units, such as the Punchbowl Formation, likely played a role in the creation and evolution of the fault core.

This regional variation in the fault core composition may be why the southern fault core at traverse 2 is dissimilar to the rocks on either side. However, the fault cores examined in traverses 1 and 3 are similar to the adjacent rocks. This may suggest that the fault cores of traverse 1 and 3 experienced less slip than the southern fault core at traverse 2. This smaller amount of slip would place rocks of less variation in contact with the fault core. It is also possible that the processes occurring in the fault cores of traverse 1 and 3 are such that the latest compositions of the adjacent rocks influence the fault core geochemistry, overprinting geochemical signatures of earlier rock interaction.

To examine how the geochemical character of the rock changes in spatial relationship to the fault core, the data for each oxide and trace element have been plotted with respect to the distance from the fault cores of traverse 1 and 2 (Figs. 40 and 41). The amount of SiO_2 in the rocks north of the fault core in traverse 1 is 40 to 45 wt.% (Fig. 40a), similar to the meta-basalts in Haxel et al. (1986). The silica content is nearly constant across the damage zone and in the fault core. South of the fault core, between the two branches of the Punchbowl fault, silica is more abundant, with values as high as 67.7 wt.%, suggesting that this rock is probably a meta-greywacke (Haxel et al., 1986).

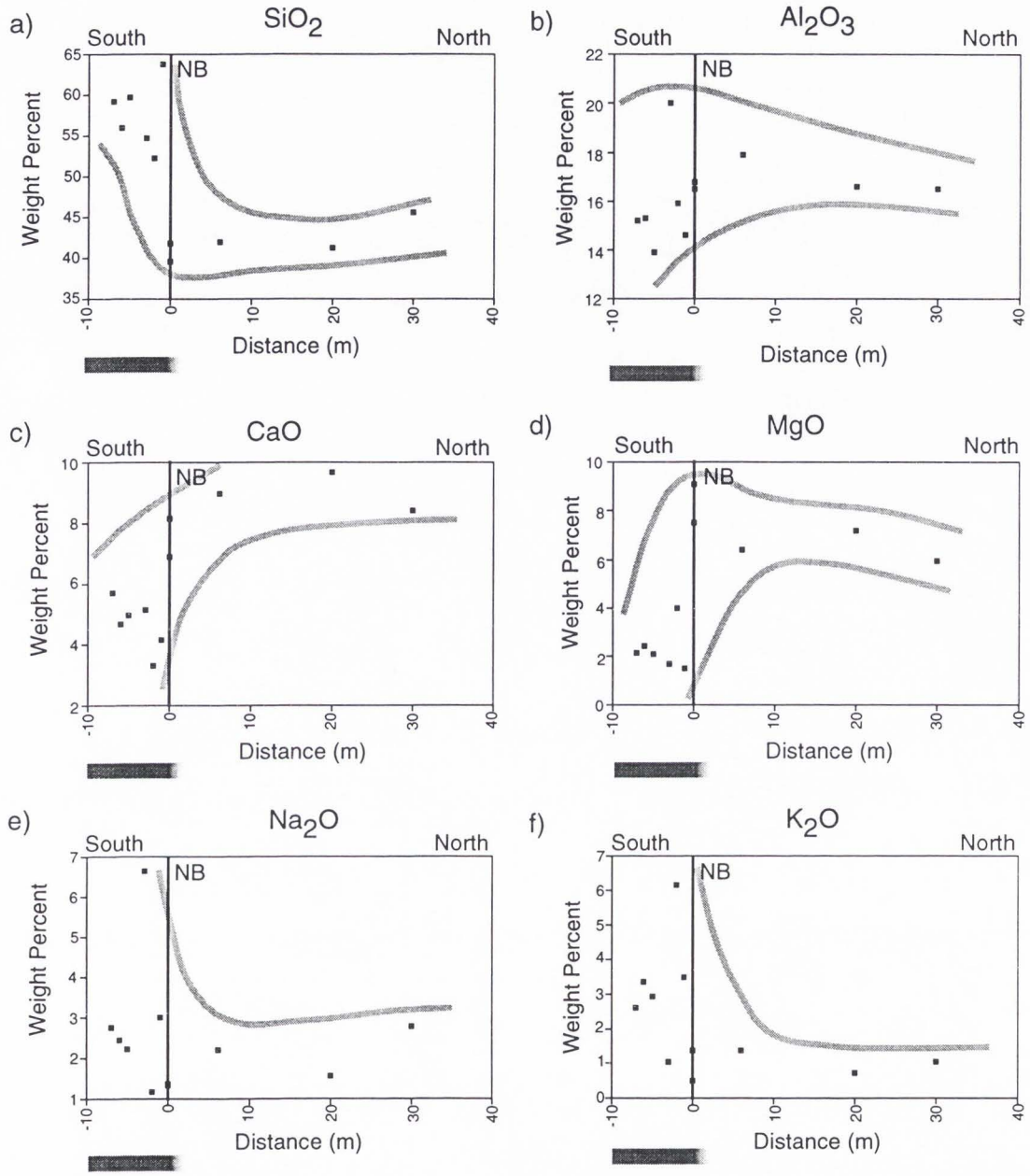

Fig. 40 Variation in the weight percent of the major oxides and the loss on ignition (LOI) across the fault zone at traverse 1. Values that are below the limit of detection have been graphed with a weight percent of 0. Line indicates the north branch (NB) of the Punchbowl fault. Grey lines outline the maximum and minimum deformation ranges measured. The bar beneath each graph shows the extent of the damage zone.

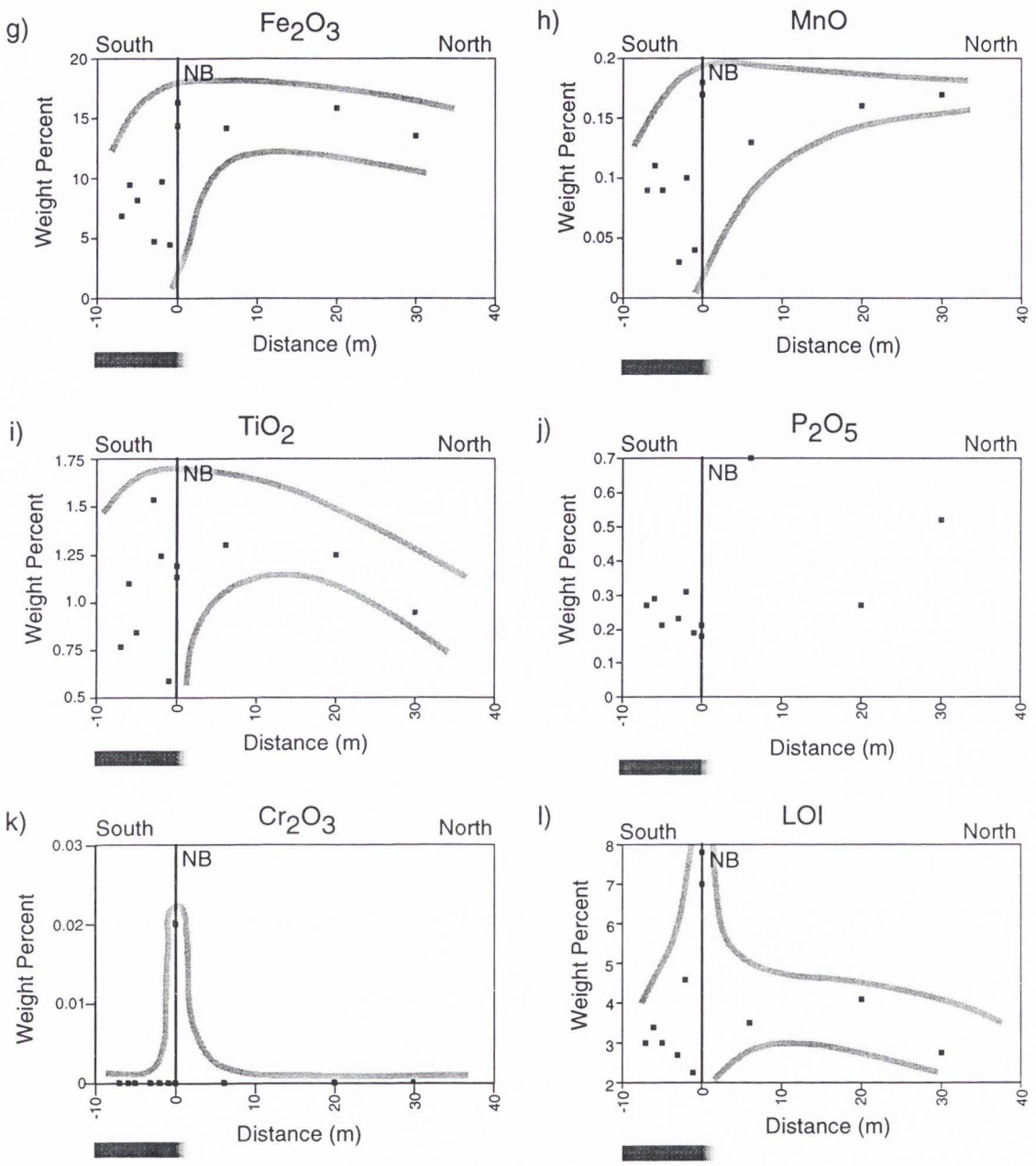

Fig. 40 Continued.

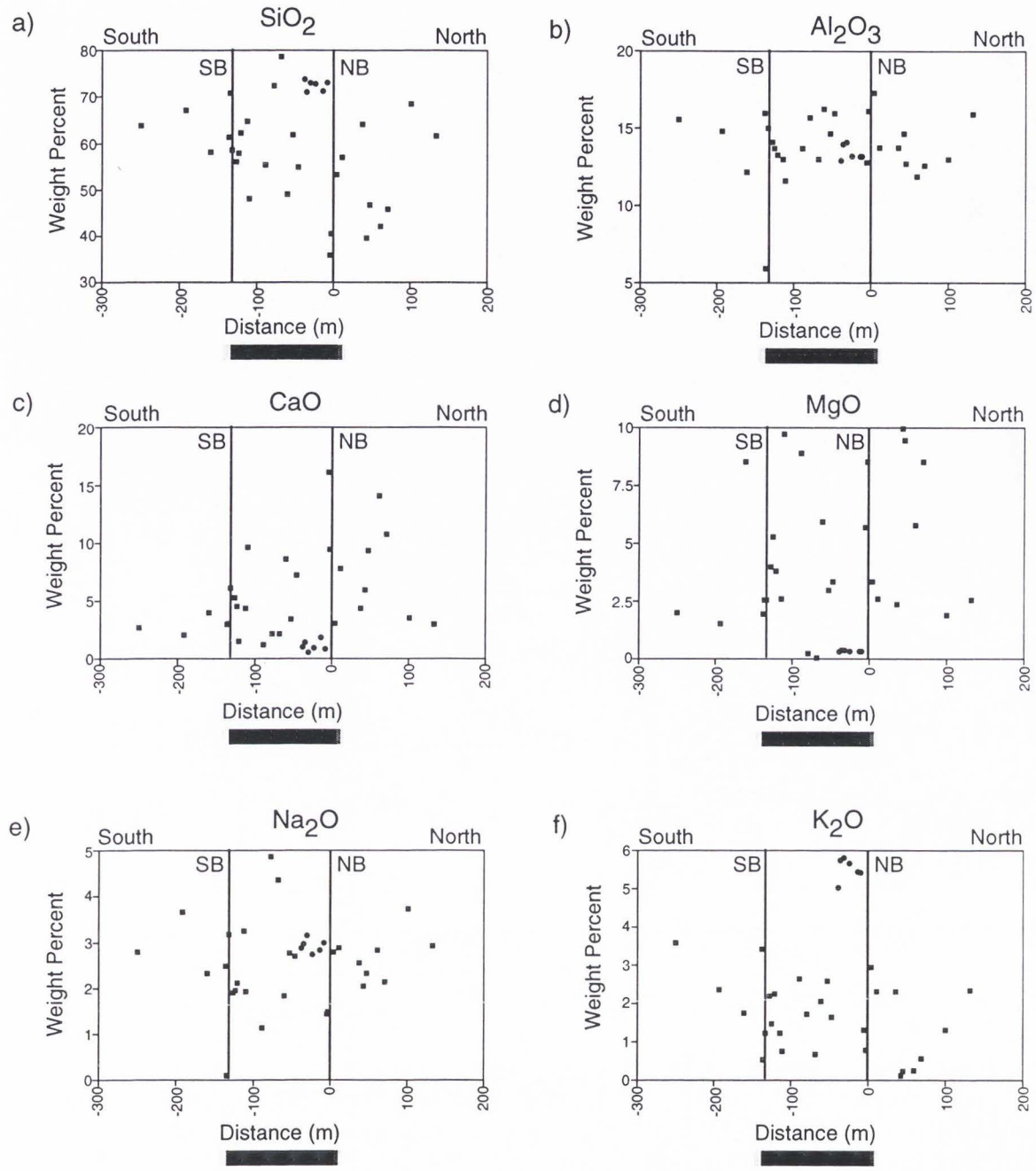

Fig. 41 Variation in the weight percent of the major oxides and the loss on ignition (LOI) across the fault zone at traverse 2. Values that are below the limit of detection have been graphed with a weight percent of 0. Lines indicate the north (NB) and south branches (SB) of the Punchbowl fault as marked. Grey lines outline the maximum and minimum deformation ranges measured. The bar beneath each graph shows the extent of the damage zone. Circles are from the aplite and squares are from the Pelona schist.

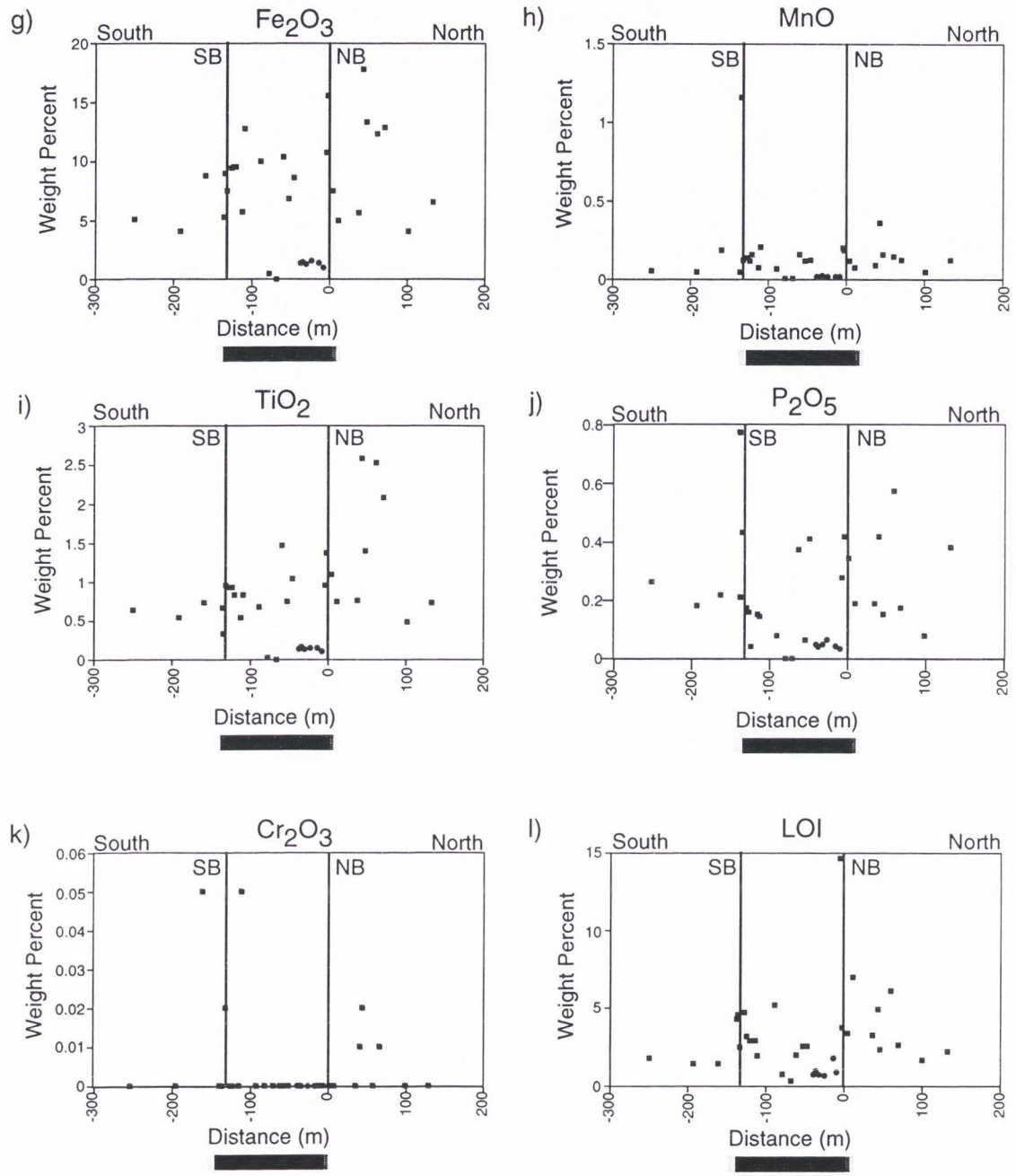

Fig. 41 Continued.

This change in SiO_2 across the fault core is probably due to a lithology change, and is not related to any fault driven geochemical changes. This is suggested by the lack of any intermediate values in the damage zone or the fault core which might reflect mixing of the metabasalt and the metagreywacke.

For traverse 2, the percentage of SiO_2 in the Pelona Schist is more variable and ranges from less than 40 wt.% to over 70 wt.% north of the Punchbowl fault (Fig. 41a). Between the two branches of the fault, the values are also variable, ranging from 48.1 to 78.6 wt.%.

The CaO abundance seems to increase in the damage zone relative to the protolith in traverses 1 and 2 (Figs. 40c and 41c). In traverse 1, the CaO is over 8 wt.% in the damage zone and drops to less than 6 wt.% in the rock south of the north strand. The data for traverse 2 show an increase in CaO from a low (<5 wt.%) in the protolith at 100 m north of the fault core, to greater than 15 wt.% in the damage zone 50 m north of the Punchbowl fault. The variability in CaO values may be due to localized calcite veining, which can be seen in the vein density plots (Fig. 16). Between the two branches of the Punchbowl fault, the values of CaO are lower than the maximum reached in the damage zone, but higher than the undeformed protolith. South of the Punchbowl fault, the values are less than 5 wt.%, similar to the protolith north of the fault. Haxel et al. (1986) reported that the meta-greywacke has a CaO value of 3.27 wt.%.

The values for MgO show a change similar to CaO across the fault zone. The amount of MgO is similar from the protolith through the damage zone in traverse 1 (Fig. 40d), but in traverse 2 the values for the protolith are low (<2.5 wt.%) with an increase in the damage zone at traverse 2 (Fig. 41d). In between the branches of the fault core, the MgO in the deformed schist is lower at traverse 1 than at traverse 2. Between the

two fault cores of traverse 2 there are some samples that have a low MgO content (< 0.5%) which are associated with samples from the intrusive rock. The igneous rock between the branches of the Punchbowl fault at traverse 2 also has low values of Fe_2O_3, MnO, TiO_2, and P_2O_5 (Fig. 41g, h, i, and j) and relatively high amounts of SiO_2 (Fig. 41a).

The fault core at traverse 1 shows increased amounts of MnO, Cr_2O_3, and LOI relative to either side of the fault core, as shown in Figure 40h,k, and l. However, this is a small increase, and may not be statistically significant. Traverse 2 does not display an increase in NaO and Cr_2O_3 (Fig. 41e and k). Although there is no elevated LOI in either of the fault cores of traverse 2, the rocks adjacent to both of the cores show an increase in LOI (Fig. 41l) as discussed earlier. There may be a depletion in K_2O in the fault core (Figs. 40f and 41f); however, the potassium is elevated in the rocks adjacent to the fault cores.

The fault core at traverse 1 is geochemically similar to the rocks on one side of the core, and does not appear to be a mix of the rocks on either side of the core (Fig. 40). This suggests that the core evolved preferentially from one side of the fault, and does not appear to indicate a large amount of mixing. The southern fault at traverse 2 seems to be more the result of a mixing of the rocks from either side on the fault core.

The abundance (in ppm) of rare earth elements (REE) and the weight percent of carbon and sulfur were measured for the samples from traverse 1 and data are shown in Figure 42. There is an increase in carbon, rubidium, yttrium, zirconium, niobium, and barium in the fault core and rocks between the two branches of the Punchbowl fault. The REE values for the protolith and the damage zone north of the Punchbowl all remain relatively constant. There is a decrease in strontium in the fault core and in the

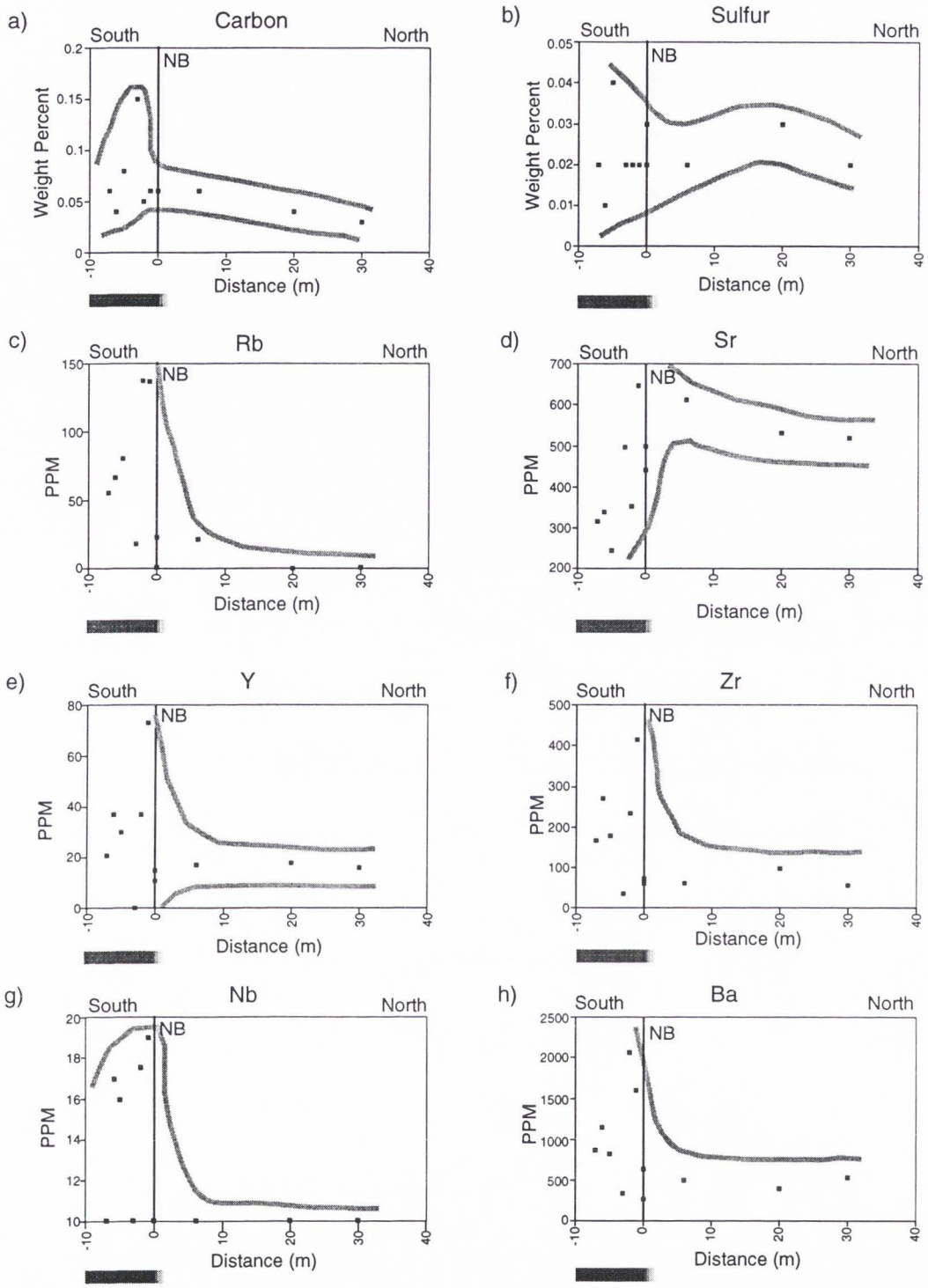

Fig. 42 Variation in trace element abundance across the fault zone at traverse 1. Values that are below the limit of detection have been graphed with a weight percent or concentration of 0. Line indicates the north branch of the Punchbowl fault. Grey lines outline the maximum and minimum deformation ranges measured. The bar beneath each graph shows the extent of the damage zone.

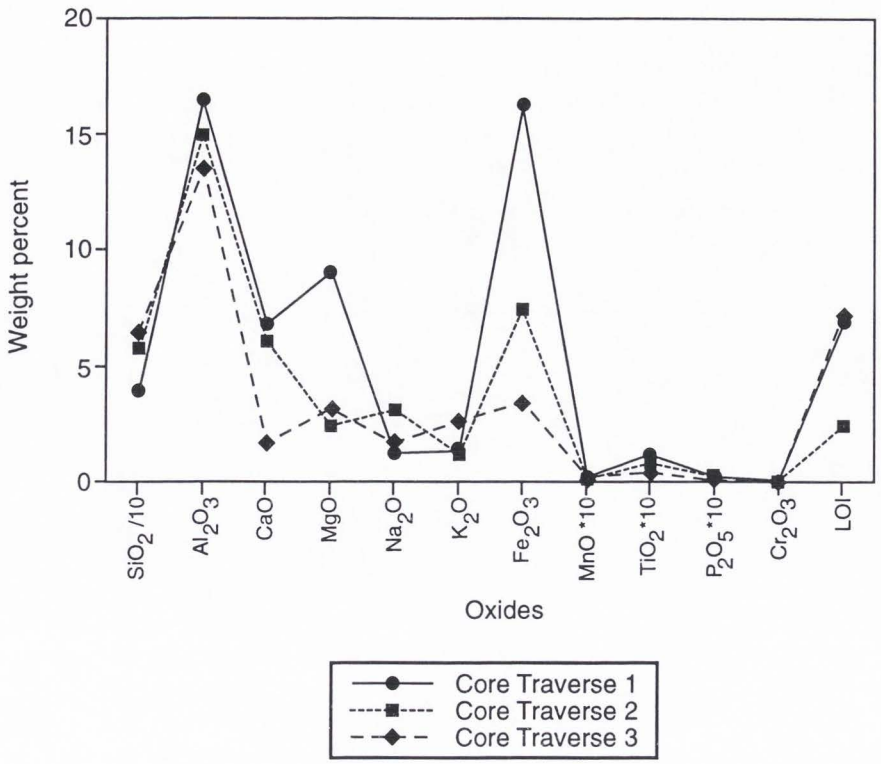

Fig 43 Along-strike variation in fault core composition. Samples are from the north branch of the Punchbowl fault at traverse 1 and the south branch at traverses 2 and 3.

rocks between the two branches of the fault. No correlation is apparent between the weight percent of sulfur and the distance from the fault core. The carbon is likely present as both graphite (Jacobson, 1980) and CO_2.

Along strike, the geochemical composition of the Punchbowl fault varies greatly (Fig. 43). Most of the variation is in the amount of CaO, MgO, Na_2O, and Fe_2O_3. The fault core is heterogeneous even though the Punchbowl fault has 44 km of slip. This suggests localized fault-related geochemical alteration occurred repeatedly during the life of the fault.

Following the method described by O'Hara (1988) and Evans and Chester (1995), the volume loss in the fault core was estimated by using the isocon technique of

Grant (1986). The percentages of oxides for the protolith are plotted against the percentages of oxides in the fault core for each traverse (Fig. 44). The diagonal line with a slope of 1 indicates the region of no volume change. Oxides that plot below the line indicate that they are enriched in the fault core relative to the protolith, whereas oxides that plot above the line are depleted. The percent volume loss is calculated by 1-m, where m is the slope of a best-fit line (dashed) through the data (Fig. 44b).

The data for traverse 1 indicate roughly 12% volume loss associated with the development of the fault core (m=0.875). The protolith is from geochemical analysis of rocks north of the Punchbowl fault and the fault core is from the northern strand. Modest enrichment in MgO, TiO_2, Fe_2O_3, and volatiles (LOI) are observed in the fault core (Fig. 44a). If these values represent enrichment due to volume loss, the slope of a best fit line through these analysis would suggest approximate 15% volume loss. However, other elements that would be expected to be enriched (MnO and P_2O_5; see Goddard and Evans, 1995) do not exhibit an enrichment. This suggests that the core at traverse 1 did not experience much volume loss.

The analytical data for traverse 2 suggest a more significant amount of volume loss (Fig. 44b). The protolith values were obtained from geochemical analysis of rocks south of the southern fault core. The fault core is enriched in MgO, TiO_2, Fe_2O_3, volatiles (LOI), CaO, MnO, and P_2O_5, which is a common group of elements to record volume loss (Goddard and Evans, 1995). The slope of the best-fit line through these oxides is m=0.526, which corresponds to approximately 47% volume loss relative to a modal volume of schist.

Altering the values of the protolith geochemistry can change the results of the volume loss calculations. It is difficult to determine the actual protolith that formed the

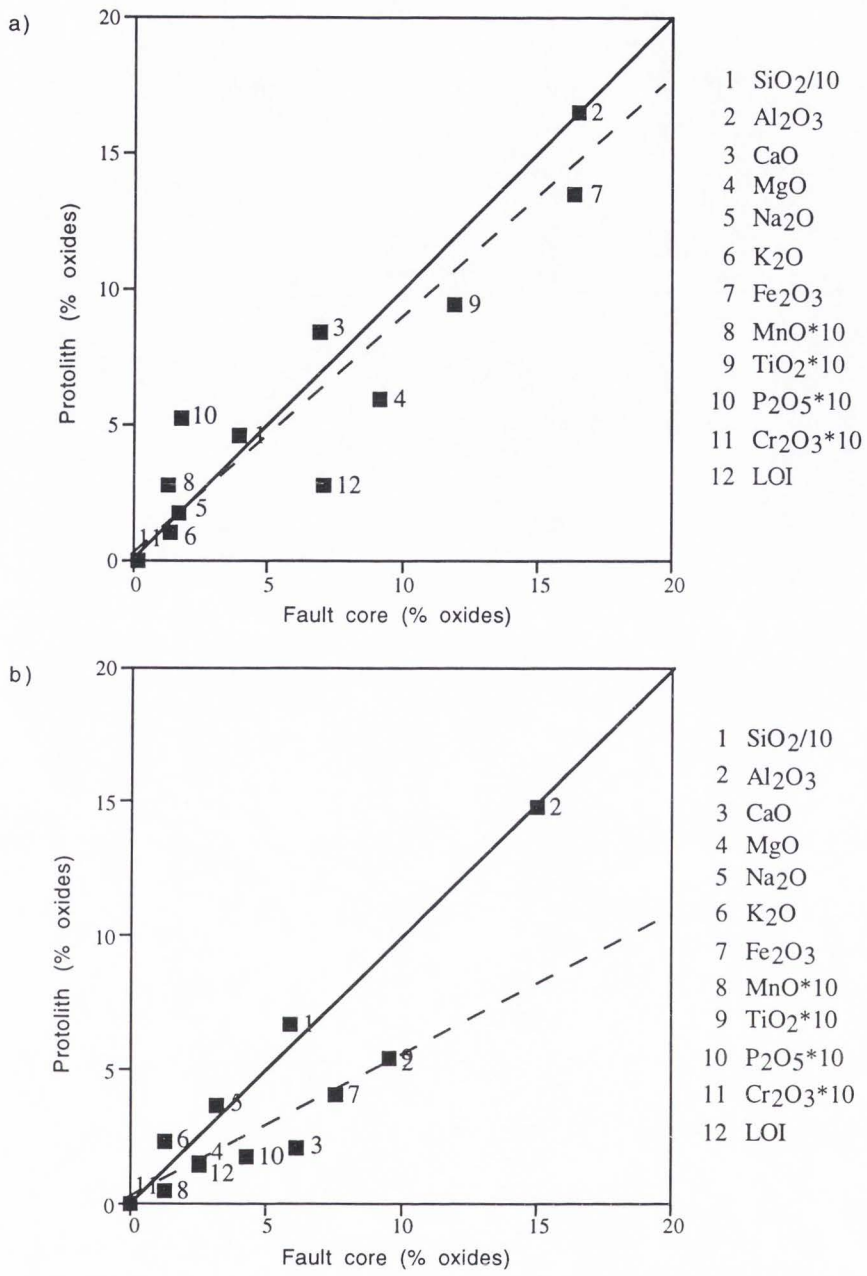

Fig. 44 Amount of volume loss within the fault core measured using the isocon technique of Grant (1986). Oxides that plot on the solid line (slope=1) show no volume loss. Oxides that plot below the line are concentrated in the fault core relative to the protolith and oxides above the line are depleted in the fault core. Slope of the line (dashed) through the oxides and forced through the origin can estimate volume loss, where % volume loss=(1-m). a) Oxides in traverse 1 plot around a line with a slope m=0.875, suggesting a volume change of 12% in the fault core relative to the protolith. b) Oxides in traverse 2 plot around a line with a slope m=.526 (dashed), indicating a volume loss of 47% in the fault core relative to the protolith.

fault core, as the fault experienced 44 km of slip. This allows for a wide variety of rocks to have contributed to the composition of the fault core.

It is not possible to examine all of the variations in protolith composition that are possible, so some average values will be examined, providing an analysis of how changing the protolith composition will affect the results of this volume loss analysis. The protolith values that Haxel et al. (1986) report can be used, as they will provide an average of the Pelona Schist composition, instead of the localized values that were obtained from the traverse data. If the metabasalt is used for the protolith at traverse 1, a volume loss of 5.8% is calculated (Fig. 45a). This is less than what was calculated using the measured protolith composition. Still, both suggest little volume loss in the fault core. If the metagreywacke is used for the protolith at traverse 2, a volume loss of 24.5% is calculated (Fig. 45b). This is less than the 47% obtained using the traverse protolith values, but still suggests a relatively large amount of volume loss in the fault core. Different results for volume loss are achieved if the geochemical values for the protolith are changed to reflect a host rock composition that is half metabasalt and half greywacke. Geochemical values for these different rock types are from Haxel et al. (1986). The volume loss in the core of traverse 1 is increased to 30% (Fig. 46a), while the core at traverse 2 has no change in volume (Fig. 46b).

Altering the protolith composition can have a large change in the volume loss when using the methods described by O'Hara (1988) and Evans and Chester (1995). This volume loss method is not appropriate for use in rocks where large variations in protolith geochemistry are likely over the displacement distance of the fault.

There are no well-defined correlations in the geochemical data; however, the distance from the fault core does influence the concentration of some elements in the rock

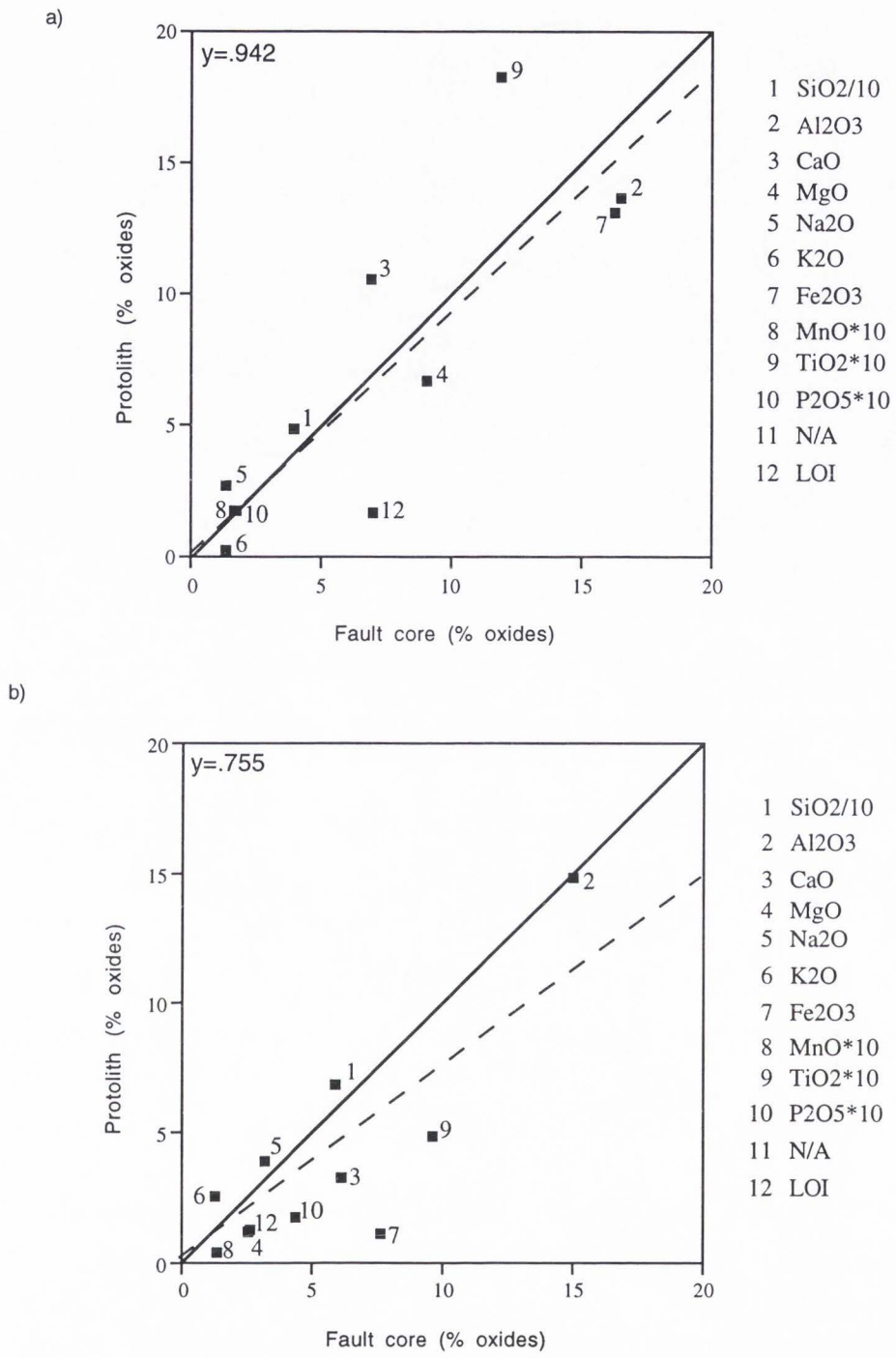

Fig. 45 Amount of volume loss using different values for the protolith composition. The value for Cr_2O_3 is not used because this value is not available for the protolith. a) Traverse 1, with a metabasalt protolith (Haxel et al., 1986), resulting in a volume change of 6% in the fault core relative to the protolith. b) Traverse 2, with a meta-greywacke protolith (Haxel et al., 1986), resulting in a volume change of 25% in the fault core relative to the protolith.

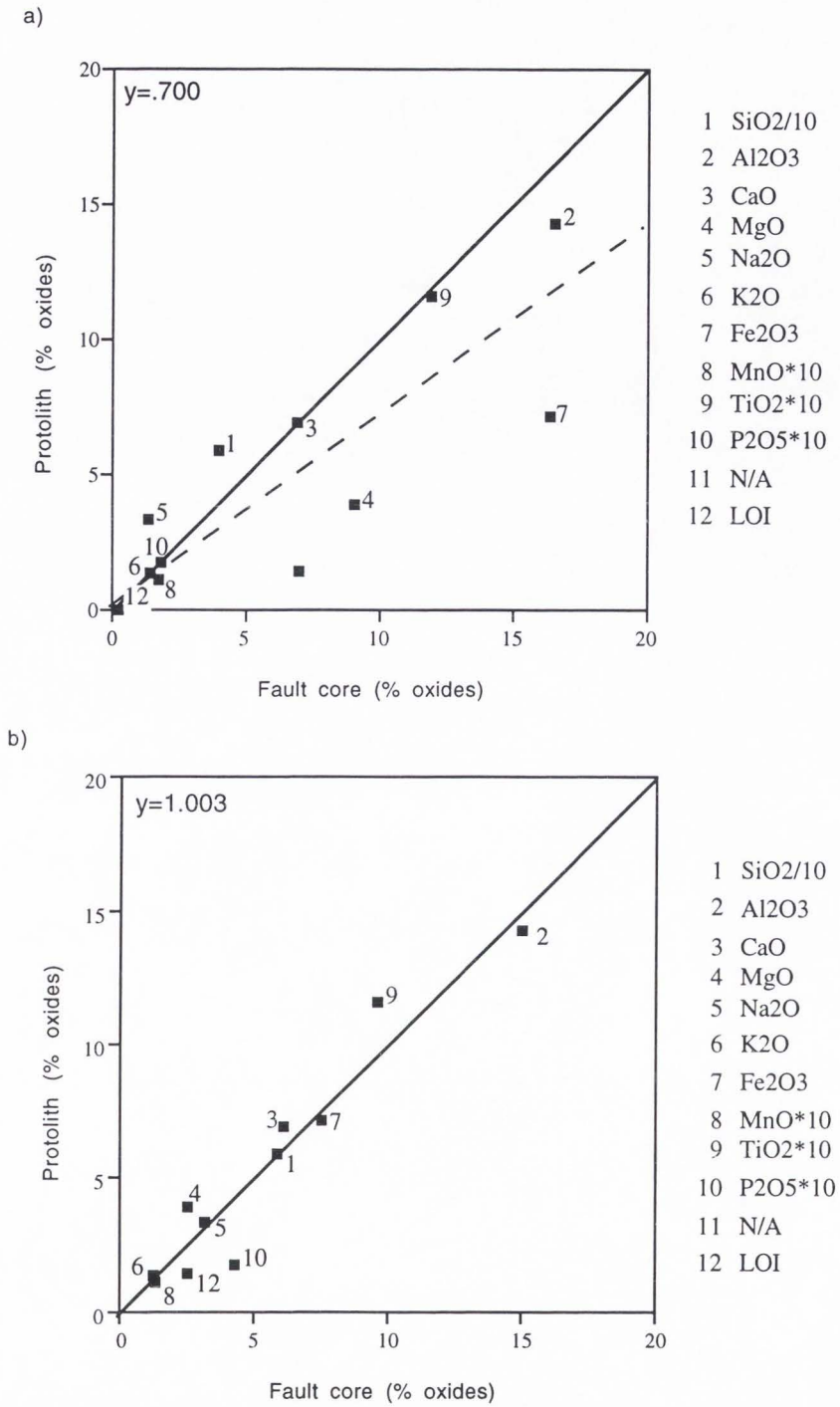

Fig. 46 Amount of volume loss using different values for the protolith composition. The value for Cr_2O_3 is not used because this value is not available for the protolith. a) Traverse 1, with a 50% metabasalt and 50% metagreywacke protolith (Haxel et al., 1986), resulting in a volume change of 30% in the fault core relative to the protolith. b) Traverse 2, with a 50% metabasalt and 50% metagreywacke protolith (Haxel et al., 1986), resulting in a volume change of 0% in the fault core relative to the protolith.

(Figs. 38 through 44). In general, the geochemical variations across the Punchbowl fault suggest a fault zone thickness of less than 10 m on either side of the fault core, with the majority of the fluid-rock interaction occurring in this region.

DISCUSSION

A fault zone is comprised of both the fault core and the surrounding damage zone, where the fault core is a region of slip localization within the damage zone. These two structural components can be distinguished by the amount and type of deformation and alteration present in the rock. The contact between the protolith and the damage zone is not distinct and is represented by a gradual increase in deformation, but the contact between the fault core and the damaged zone of the Punchbowl fault is sharp and nonplanar. These relationships were also noted at other locations along the Punchbowl (Chester and Logan, 1986) and other faults (Chester et al., 1993; Evans and Chester, 1995; Caine et al., 1996).

Although the fault core is surrounded by a damage zone, it does not have to be located in the center of a fault zone, because the thickness of a damage zone can be different on either side of the fault core. There can be, and often is, more than one fault core within a fault zone. This has been documented at other locations along the Punchbowl fault (Chester and Logan, 1987).

The fault core of the Punchbowl fault in the Pelona Schist appears to have macroscopic and petrographic textures similar to the fault core at other locations along the Punchbowl and San Gabriel faults (Chester and Logan, 1987; Chester et al., 1993; Evans and Chester, 1995). At the outcrop scale, the fault core of the Punchbowl fault in the Pelona Schist is a 10-cm-thick band of petrographically amorphous cataclasite that is typically foliated at the microscopic scale. In some locations the fault core is often an anastomosing collection of thin, fault-plane-bounded gouge zones. This agrees with what was found at other locations on the Punchbowl, San Andreas, and San Gabriel faults (Chester and Logan, 1987; Chester et al., 1993; Evans and Chester, 1995).

Anderson et al. (1983) found the fault core of the San Gabriel fault varied considerably in thickness, from a 70-m-thick gouge zone to thin cataclasite zones 1 to 10 cm thick. At a majority of locations, the gouge or cataclasite zones are less than 7 cm thick. The gouge layer of the Punchbowl fault in the sedimentary rock is dark, aphanitic, and typically 30±5 cm thick (Chester and Logan, 1986). In contrast, Evans and Chester (1995) found that the fault core of the San Gabriel fault is a foliated cataclasite several meters thick, with a central ultracataclasite layer that is 2-20 cm thick.

At the microscopic scale, the fault core is optically fine-grained and locally foliated parallel to the strike of the fault core. There is evidence that the fault core has undergone multiple periods of deformation, with varying types of deformation, primarily brittle grain-size reduction, cataclasis, and alteration. Disarticulated veinlets are also present throughout the core, suggesting that although the fault core may periodically experience fluid-derived emplacement of material within the core, subsequent slip in the fault core destroys the veins. This implies that although the deformation within the fault core repeats over time, the type of deformation is also variable. The core of the San Gabriel fault shows similar features (Chester et al., 1993; Evans and Chester, 1995).

Discrete cataclasite bands and slip surfaces indicating enhanced deformation are often located within the fault core, and are the result of slip localization. The rock surrounding the bands of slip localization within the core are also deformed, although to a lesser extent. Deformation within the fault core is probably a continuing process, with the location of maximum slip within the fault core changing throughout the life of the fault. Similarly, Chester and Logan (1986) found that the gouge layer of the Punchbowl fault contains an anastomosing network of shear bands interpreted as surfaces on which individual slip events were localized.

The fault core of the Punchbowl fault differs from that of the San Gabriel fault (Chester et al., 1993) when viewed under the scanning electron microscope. Although fine-grained amorphous materials are common in both of the fault cores, the Punchbowl fault has more distinct foliation structures at the SEM scale than the San Gabriel fault (Chester et al., 1993; Evans and Chester, 1995). This is probably due to the layered-silicate host rock that bounds the Punchbowl fault in this study region.

Three traverses across the Punchbowl fault show that the damage zone is present on both sides of the fault core, with an increase in meso- and microscopic damage element densities close to the fault core and the greatest intensity adjacent to the fault core. The damage zone is not the same on both sides of the fault core in either spatial extent or amount of deformation. Traverse 2 shows that the southern damage zone is not as thick and is less damaged than the damage zone on the north side of the Punchbowl fault.

The majority of the differences between the fault zone that I studied and those examined by others (Chester and Logan, 1987; Chester et al., 1993; Evans and Chester, 1995) appear to be within the damage zone. The damage zone of the Punchbowl fault in sedimentary rock is thinner (approximately 15 m) than that in the Pelona Schist, although the zone varies in thickness along strike (Chester and Logan, 1986). The damage zone of the San Gabriel fault is thicker, roughly 100 m thick, with the primary deformation being cataclasis (Chester et al., 1993). Thus it appears that weaker rocks produce a thinner damage zone.

Macroscopic and microscopic brittle deformation densities may show that the damage zone adjacent to the fault core in the Punchbowl fault is more deformed than the core itself (Figs. 15 and 33). This is an apparent signal caused by the type of deforma-

tion measured as the fault core is often too damaged to distinguish individual damage elements such as fractures or slip surfaces. The extreme deformation in the fault core is difficult to quantify, as it is mainly evidenced by a marked reduction in grain size, increased alteration, and cataclasis. This deformation, especially grain-size reduction, also masks other types of deformation, such as fractures.

Portions of the Punchbowl fault can have more than one fault core, similar to what is reported by Chester and Logan (1987) for the Punchbowl fault farther west. In much of the study region, these multiple cores are separated by as much as 1.2 km, although in the eastern portion, the multiple fault cores are closely spaced (<1 m), anastomosing features. Where the Punchbowl fault is composed of multiple fault cores, each of these main strands has its own damage zone associated with it. The rocks between these damage zones are more deformed and altered than the rocks outside the fault zone, implying that the damage zones overlap. This is evident in traverse 1 and traverse 2, where the amount of deformation that is present between the main fault branches is greater than in the undamaged protolith. There are also smaller faults present within the zone between the two major branches. These smaller faults are also locations of slip localization, and create their own concentrations of deformation.

The "intrafault" damage zone is similar to the damage zone outside of, but close to, the main branches, in both the type and amount of deformation present. Alteration of the host rock is prevalent throughout the entire "intrafault" damage zone at traverse 1 but not at traverse 2, showing that there is along-strike variation in the amount of "intrafault" alteration.

These data suggest that some portions of the San Andreas fault system may consist of multiple slip surface faults, with overlapping damaged zones that are regions of

enhanced microfracturing, alteration, and reorientation of primary structures (Chester et al., submitted).

Mesoscopically, the deformation in the Punchbowl fault is displayed as fractures, faults, veins, reorientation of primary fabrics, and alteration of the rocks. Fracturing is the dominant mode of deformation within the damage zone. Fractures begin roughly 50 to 70 m from the fault core, with its density increasing closer to the fault core, where it reaches a maximum value. There is little evidence for faulting within the damage zone, especially subparallel to the main fault. This may be due to the schistose foliation of the Pelona Schist, making identification of slip surfaces difficult in the field.

The schist has been reoriented subparallel to the Punchbowl fault within 10 to 50 m of the fault core. Slip will be accommodated along the planes of preexisting weakness produced by the alignment of phyllosilicate minerals within the schist. This can prevent the recognition of fault-parallel slip surfaces in the field, as it is difficult to determine if slip has occurred along schistose foliation.

Reorientation of schistose foliation close to the Punchbowl fault occurs at all three locations that were examined, and can be caused by two possible mechanisms. Frictional drag can reorient rocks close to a fault zone. However, the large spatial extent of the reoriented foliation makes this mechanism unlikely. Simple shear can also explain the foliation rotation. As the shearing brings the foliation subparallel to the fault core, the mechanically weak schistose foliation planes will slip further. Evans and Chester (1995) documented structures within the fault core of the San Gabriel fault that indicate it was a region of simple shear. Reorientation of primary fabric has not been documented elsewhere along the Punchbowl fault or the San Gabriel fault, although this may be due to granitic rocks lacking a primary fabric, which will exhibit rotation. The

reorientation of some dikes close to the San Gabriel fault by simple shear was noted by Chester et al. (1993).

Between the two strands of the Punchbowl fault, the fracture orientations are in a girdle pattern, suggesting that the blocks between the two fault strands also experienced rotation. This rotation will allow for an accommodation of slip along foliation between the branches of the fault. A rotating stress field is less likely, as the fracture orientations outside of the main branches of the fault do not show this girdle pattern, suggesting that the stress field had a relatively constant orientation.

Fault-block rotation between the two strands of the fault is likely, with the possibility of rotation of the rocks outside of the major fault strands likely as well. The timing of this rotation cannot be constrained, which has led to a reluctance to undertake an extensive kinematic analysis of the structural features at this location. This rotation of the rocks will make it difficult to try to determine the stress orientations that influenced the formation of the fractures and slip surfaces.

The fault-zone thickness determined from the microfracture density may record a narrow damaged zone that forms ahead and adjacent to the fault zone. There is deformation in the Pelona schist that is identifiable at over 100 m from the fault core. This deformation is predominantly intragranular fracturing and undulatory extinction in quartz grains, with local intergranular fracturing. However, it is unlikely that this deformation is due to processes associated with the Punchbowl fault, as there is an increase in the overall amount of cleavage dominated intergranular fracturing within 50 m of the fault core and an increase in the amount of strained quartz grains at roughly 20 m from the core. This suggests that although there may be some background level of deformation within the Pelona Schist, the fault-related microscopic deformation appears to be

concentrated to within 50 m of the fault core.

The microstructures documented here show a progression in deformation towards the fault core from intragranular fracture to intergranular fracture, and an increase in the amount of cataclasis, slip along layered silicates, development of foliation, veining, and the development of a very fine-grained fault core material. The fractures, veins and cataclasite formation begin to increase at roughly 40-50 m from the fault core, but are not pervasive until 10 m from the fault core. Grain-size reduction occurs only within 10 m of the fault core, suggesting that the zone of closely spaced microfracturing is not thick.

The recognizable fault-related microfractures define a zone of no more than approximately one half the thickness of similar zones along faults of similar or less displacements in granitic rocks (Chester et al., 1993), which suggests that the schists, and perhaps by extension, Franciscan rocks that comprise much of the protolith of the San Andreas fault may result in narrow damaged zones adjacent to the fault owing to their "softer" properties. Comparisons with other studies of naturally formed gouges in serpentinite (Hoogerduijn-Strating and Vissers, 1994) indicate that extreme slip localization and brittle processes in Fe/Mg-rich layered silicates, commonly with little fabric development, may be common.

Geochemical variation across the Punchbowl fault zone is mostly due to changes in lithology rather than to fault-related processes. The damage zone is very similar in chemical composition to the protolith. Also, instead of a fault core that differs geochemically from the host rock, the bulk compositions of the fault core closely match the composition of the damage zone on one side of the core, indicating that the principal slip surfaces examined here evolved preferentially from the one side of the fault. This is

contrary to work by Evans and Chester (1995), where the whole-rock geochemistry of the San Gabriel fault core reflects mixing of protoliths from both sides of the fault.

Most of the mineralogic variation within the Punchbowl fault zone is limited to the fault core. The mineralogy of the damage zone is similar to the protolith; it is in the fault core where the Punchbowl fault undergoes mineralogical changes. The fault core has an increase in the amount of clays over the damage zone at traverse 1 (Fig. 36). This is contrary to what was seen at traverse 2, which shows little clay in the core (Fig. 37), and in the San Andreas fault, where the gouge contains little (< 4 wt. %) clay, mostly kaolinite (Anderson et al., 1980). Evans and Chester (1995) showed that the abundance of clays in the core of the San Gabriel fault is variable as well. Thus, although clays are present in portions of these faults, they are not ubiquitous, and cannot account for the low fault strength alone. At both traverse 1 and traverse 2, clinochlore is present in the fault core (Figs. 36 and 37), and formed as a result of hydration of muscovite. This requires the addition of fluids into the core, probably during faulting.

Fluid-rock interactions, as indicated by geochemistry (Figs. 40 and 41) and x-ray diffraction (Figs. 36 and 37), resulted in local changes in composition across and along strike of the fault. Despite the relatively large amounts of slip, the fault core was not chemically homogenized along strike (Fig. 43). Fluid-rock interactions at traverse 1 resulted in an internal "shuffling" of components with little transport of elements into or out of the fault core, whereas at traverse 2, fluid-rock interactions may have resulted in volume loss accompanied by at least local transport of species out of the system. The volume loss along strike of the Punchbowl fault is also variable (Fig. 44). There is little or no volume loss at traverse 1; however, data from traverse 2 may support a volume loss of 47%. Evans and Chester (1995) found that the fault core of the San Gabriel fault

experienced roughly 37% volume loss in granitic rocks.

Absent from much of the Punchbowl fault zone examined here are pervasive veins in damage zone samples, as compared to the extremely vein-rich damaged zone documented by Chester et al. (1993). Veins associated with the Punchbowl fault are scattered throughout the damage zone with no apparent relationship to the distance from the fault core; they do not display the increase in density close to the fault core that has been documented along other large faults. This indicates a more limited fluid-rock interaction in portions of the fault zone and suggests that fluids were localized and are not necessarily concentrated close to the fault core. Alternately, this may also suggest that the composition of the fluids within the fault have different compositions.

This heterogeneity in the fault zone may mark the chemical influence of the different protoliths along the fault, or may also show the influence of local variations in the flow systems along and adjacent to the fault. Similar along-strike variations were found by Evans and Chester (1995), and thus, such chemical heterogeneity may be the rule for strike-slip faults of the San Andreas system. Such heterogeneity may have mechanical implications, because changes in fault composition and the associated fluid-rock interactions may result in different fault properties and behaviors. In contrast, Chester and Logan (1986) found the gouge layer of the Punchbowl fault to be mineralogically, geochemically, and texturally homogeneous along strike.

Chester et al. (1993), examining the San Gabriel fault, documented slip localization and particulate flow in the ultracataclasite zone in the fault core and suggested that elevated pore fluid pressures were present in the fault zone based on microstructures present in the fault core. Evans and Chester (1995) further examined the San Gabriel fault zone using whole-rock geochemistry and also determined that fluids were present

in the fault zone, although there are local and regional variations in the amount of fluids. This is similar to what is seen in the Punchbowl fault.

The fluid-rock interactions documented in this study may not have contributed greatly to a reaction-softening suggested for other fault zones (Janecke and Evans, 1988; Wintsch et al., 1995). The primary change that occurred in the Punchbowl fault rocks was the transformation of muscovite-rich rocks to chlinochlore-rich rocks, and it is unlikely that this made any significant change in frictional properties of the fault. The geochemical data also suggest that the fault core at traverse 1 is compositionally similar to the protolith found on one side of the fault zone. This agrees with experimental work on slip localization, in which slip often is focused along the interface between the gouge and the forcing blocks (Higgs, 1981; Yund et al., 1990). This may be due to the lithology of the host rock, which is already mechanically soft.

I suggest that the softer protolith in this study area results in a narrower damaged zone than is present in granitic rocks (Chester et al., 1993; Evans and Chester, 1995), and that principal slip surfaces in this case develop by comminution of quartz, albite, and muscovite. Alteration of the Fe/Mg phases and muscovite resulted in additional layered silicates developing in the damaged zone and fault core. This alteration requires the addition of water, suggesting that fluids were present in the fault core. Geochemical and vein data indicate the presence of fluids in the damage zone as well. The fluids within the Punchbowl fault zone were localized, as indicated by the variability in fluid-related deformation and alteration both across the fault zone and along strike.

CONCLUSIONS

The Punchbowl fault exhumed from a depth of 4 km is composed of two main regions, the fault core and the damage zone. The fault core is a region of slip localization, where deformation is dominated by grain-size reduction and alteration. Most of the 44 km of right-lateral slip on the Punchbowl fault has occurred on these thin zones (<10 cm) of localized slip. The fault cores are enveloped by damage zones, where deformation is dominantly brittle and semi-brittle, with layered silicates deforming by fracturing, cataclasis, and slip. Closer to the fault core, alteration of minerals becomes more prevalent. Transformation-enhanced softening was probably not a significant cause of slip localization in this portion of the Punchbowl fault.

The thickness of a fault zone depends upon the type of deformation used to describe the fault zone, as well as the scale of observation (Fig. 47), which agrees with previous studies done in this area (Chester et al., 1993; Evans and Chester, 1995). Mesoscopic fractures suggest that the fault zone begins 50 m from the fault core, whereas the onset of fault-related microfracturing occurs at approximately 41 m from the fault core. Geochemical data suggest a thickness of less than 10 m, grain-size reduction occurs over a 10-m-thick region, and significant mineralogic changes occur over a region 20-30 m thick. In addition, reorientation of preexisting foliation occurs over a zone 30 m thick.

The entire Punchbowl fault zone, which formed at a depth of roughly 4 km, as measured by the distribution of microstructures, geochemical alteration, and changes in preexisting structures, shows that the fault zone is narrower in the schist than in other strike-slip faults developed in granitic gneisses (Chester et al., 1993).

The narrowness of the fault zone may have implications for the San Andreas

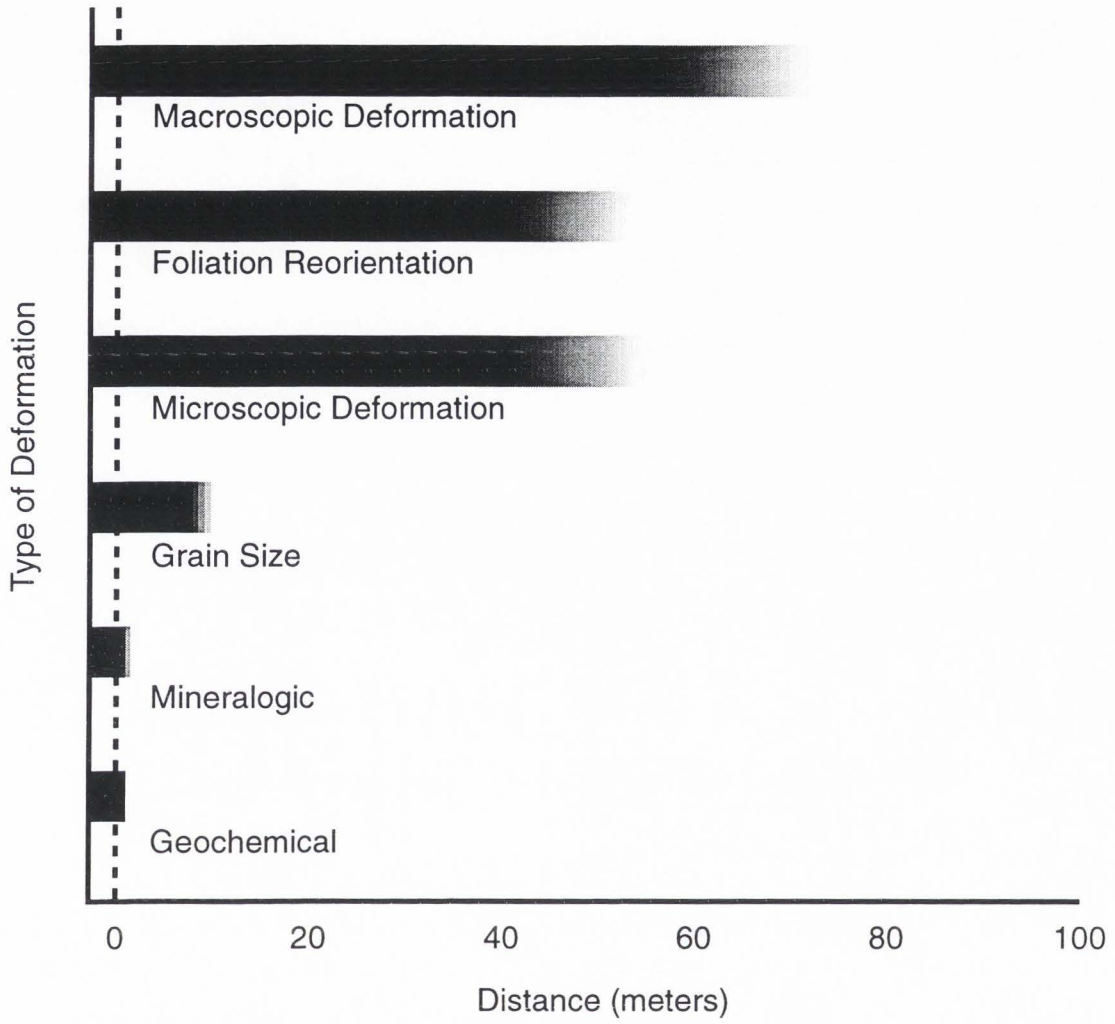

Fig. 47 Spatial variability in the extent of fault-related deformation and alteration. The bars indicate the half thickness of the fault zone, which is measured from the center of the fault core into the undeformed protolith. The ends of the bars fade out because it is difficult to determine the exact point that the fault zone begins.

fault zone drilling project. Zoback and Hickman (1996) proposed to drill an angled hole through the San Andreas fault near Parkfield, California, while recovering continuous core. The Punchbowl fault may be an analog for the San Andreas fault at depth, as they are being sampled from similar depths of formation and both have metamorphic host rocks.

The data from the Punchbowl fault show that the fault zone can be less than 200 m thick, with most of the deformation limited to an even thinner (20 m?) zone of intense deformation and slip localization. Another difficulty may be core recovery, because the fault core and adjacent rock are extremely fractured and friable. However, these portions of the San Andreas fault need to be examined, as it is the location of major deformation and it will provide insight into the fault-related processes and fluid-rock interactions that form the fault zone and influence its properties.

Variation in fault-zone thickness, structure, and composition between individual faults (and fault segments) is probably due to many factors. The lithology of the host rock appears to play an important role in determining the fault-zone characteristics. The mechanical nature of the host rock and how it responds to the fault-related stress are important in determining how the rock responds to fault movement. This appears to be especially important in controlling the deformation of the damage zone. The fault core is probably controlled by the geochemical reaction of the rocks and how they are affected by fluids that circulate within the fault system.

The fault core of the Punchbowl fault is similar in texture to other large displacement fault cores such as the San Gabriel fault (Chester et al., 1993; Evans and Chester, 1995), the Punchbowl fault to the northwest (Chester and Logan, 1987), and the White Rock thrust (Goddard and Evans, 1995). This suggests that the processes that occur in

the cores of large displacement faults are similar, resulting in a foliated, fine-grain, cataclasite-dominated region of slip localization. The composition of the fault core is variable along strike, with little geochemical or mineralogical homogenization, despite 44 km of displacement. So, although the processes that form fault cores are similar, localized interaction of fluids will cause compositional variability within the core.

Fault displacement may not be important in determining the thickness of a fault (Scholz, 1987; Evans, 1990). The Punchbowl fault has 44 km of slip accommodated upon two (possibly more in some locations) 10-cm-thick zones of slip. These thin fault cores accommodate the bulk of the deformation and strain. This means that the Punchbowl fault has a thickness that is $4.5 \times 10^{-5}\%$ the fault displacement, which is much narrower than data presented in Hull (1988). These thin zones of localized slip have a damage zone associated with them that adds to the faults' overall thickness. However, at traverse 2 the entire fault zone is considerably less than 200 meters thick. Even with the damage zone thickness, the Punchbowl fault is very thin, with a thickness that is less than 0.45% of the displacement at station 2. Ehlig (1987) mapped the two strands of the Punchbowl as converging east of traverse 2. This would most likely result in an even thinner fault zone, as much of the fault zone thickness measured at traverse 2 is found between the two main fault strands (Fig. 6).

The damage zone of the Punchbowl is defined as a region of deformation encompassing the fault core, and may represent a damaged zone that forms ahead and adjacent to the fault as it evolves (e.g., Scholz et al., 1993). Shipton and Cowie (1996) used a kinematic model, where continued slip along the fault results in a thickening fault zone, accompanied by increasing deformation in the damage zone. The predominance of reoccurring, slip-related deformation in the fault core, along with the narrow damage

zone associated with the Punchbowl fault, suggests that the damage zone is not evolving with fault growth. Thus, the damage zone does seem to indicate a region of initial deformation, with little thickening or overprinting by later deformation.

Fluids appear to be involved in the formation of the fault zone. This is shown by the emplacement of veins as well as mineralogical and geochemical alteration. Judging by the distribution of veins, however, the fluid interaction appears to be localized in portions of the damage zone. Most of the fluid-rock interaction is taking place in the fault core, where the majority of mineralogic changes occur. Geochemical data at traverse 1 indicates little fluid rock exchanges outside the core in the damaged zone. Although the fluids may assist in a reshuffling of the mineralogy, there is no evidence that elements are being lost or gained within the fault core system. At traverse 2, volume loss and fluid-rock exchange are supported by the data. While fluid interaction may be important in the formation of the fault core, there is variability in its effects.

It is not clear why slip localizes on the narrow faults. There is no significant microstructural or geochemical evidence in the data to suggest why slip localized along the narrow fault core(s). The mechanisms in the Pelona Schist involve "ordinary" brittle and semi-brittle deformation mechanisms common to phyllosilicate-rich rocks. The textures and geochemistry used to infer the fluid-rock interactions likewise point to "typical" reactions in and near the fault. Chester et al. (submitted) suggested that when a fault develops, it can be an extremely efficient wave/energy guide for subsequent seismic ruptures (Ben-Zion and Malin, 1991; Hough et al., 1994; Li et al., 1994; Eberhart-Phillips et al., 1995). Thus, large amounts of energy become concentrated in the fault core, creating the continual grain-size reduction, vein creation and destruction, and alteration that marks the fault cores. Energy dissipated into the damaged zones may result in

the more diffuse nature of the distribution of faults, fractures, and alteration patterns observed there. Chester (1995) suggested that only narrow faults may support the stress drops necessary for seismic slip to be propagated to depths of 10-15 km in wet granitic crust. Thus, thin fault cores observed here and by Chester et al. (1993) and Anderson (1983) may be the result of a global mechanical constraint placed by the rheology of the upper crust.

REFERENCES

Allmendinger, R.W., 1988, Stereonet. Version 4.9.6, copyrighted software, Cornell University, Ithaca, NY.

Anderson, E.M., 1951. The Dynamics of Faulting and Dyke Formation. Oliver and Boyd, Edinburgh, Scotland, 206 pp.

Anderson, J.L., Osborne, R.H. and Palmer, D.F.,1980. Petrogenesis of cataclastic rocks within the San Andreas fault zone of Southern California, USA. Tectonophysics, 67: 221-249.

Anderson, J. L., Osborne, R. H. and Palmer, D. F., 1983. Cataclastic rocks of the San Gabriel Fault--an expression of deformation at deeper crustal levels in the San Andreas fault zone. Tectonophysics, 98: 209-251.

Atwater, T., 1970. Implications of plate tectonics for the Cenozoic tectonic evolution of western North America. Bull. Geol. Soc. of Amer., 81: 3513-3536.

Ben-Zion, Y. and Malin, P., 1991. San Andreas fault zone head waves near Parkfield, California. Science, 251: 1592-1594.

Best, M.G., 1982. Igneous and Metamorphic Petrology. W.H. Freeman and Company, New York, NY, 630 pp.

Blanpied, M. L., Lockner, D. A. and Byerlee, J. D., 1992. An earthquake mechanism based on rapid sealing of faults. Nature, 358: 574-576.

Bruhn, R.L., 1994. Fracturing in normal fault zones: implications for fluid transport and fault stability. In: The Mechanical Involvement of Fluids in Faulting, U.S.G.S. Open File Report 94-228: 231-246.

Brune, J. N., Henyey, T. L. and Roy, R. F., 1969. Heat flow, stress, and rate of slip along the San Andreas Fault, California. J. Geophys. Res., 74: 3821-3827.

Byerlee, J. D., 1978. Friction of rocks. Pure Appl. Geophys., 116: 615-626.

Byerlee, J.D., 1993. Model for episodic flow of high-pressure water in fault zones before earthquakes. Geology, 21: 303-306.

Byerlee, J.D., 1990. Friction, overpressure and fault normal compression. Geophys. Res. Lett., 17: 2109-2112.

Caine, J.S., Evans, J.P. and Forster, C.B., 1996. Fault zone architecture and permeability

structure. Geology, 24: 1025-1028.

Chester, F. M., 1995. A rheological model for wet crust applied to strike-slip faults. J. Geophys. Res., 100: 13,033-13,045.

Chester, F. M., Evans, J. P. and Biegel, R. L., 1993. Internal structure and weakening mechanisms of the San Andreas fault. J. Geophys. Res., 98: 771-786.

Chester, F. M. and Logan, J. M., 1986. Implications for mechanical properties of brittle faults from observations of the Punchbowl Fault Zone, California. Pure Appl. Geophys., 124: 79-106.

Chester, F. M. and Logan, J. M., 1987. Composite planar fabric of gouge from the Punchbowl Fault, California. J. Struct. Geol., 9: 621-634.

Dibblee, T. W., Jr. , 1961. Geological Map of the Bouquet Reservoir Quadrangle, Los Angeles County, California 1 : 24,000. U. S. Geol. Surv. Map MF-79.

Dibblee, T. W. Jr., 1967. Areal geology of the western Mojave Desert, California. U.S.G.S. Prof. Paper 552.

Dibblee, T. W. Jr, 1968. Displacements on the San Andreas fault system in the San Gabriel, San Bernadino, and San Jacinto Mountains, Southern California. In: W. R. Dickinson and A. Grantz (Editors), Proc. Conf. on Geologic Problems of San Andreas Fault System. Stanford University Publications, Stanford, CA, pp. 260-278.

Dibblee, T. W., 1987, Geology of the Devil's Punchbowl, Los Angeles County, California. Geol. Soc. Am. Centennial Field Guide--Cordilleran Section: 207-210.

Eberhart-Phillips, D., Stanley, W. D., Rodriguez, B. D. and Lutter, W. J., 1995. Surface seismic and electrical methods to detect fluids related to faulting. J. Geophys. Res., 100: 12,919-12,936.

Ehlig, P. L., 1958. Geology of the Mt. Baldy region of the San Gabriel Mountains, California. PhD Dissertation, University of California, Los Angeles.

Ehlig, P. L., 1981. Origin and tectonic history of the basement terrain of the San Gabriel Mountains, central Transverse Ranges. In: W. G. Ernst (Editor), The Geotectonic Development of California. Prentice-Hall, Englewood Cliffs, NJ, pp. 253-283.

Ehlig, P.L., 1987. Geologic structure near the Cajon Pass scientific drill hole. Geophys. Res. Lett., 15: 953-956.

Engelder, J. T., 1974. Cataclasis and the generation of fault gouge. Geol. Soc. Am. Bull., 85: 1515-1522.

Evans, J. P., 1990. Thickness-displacement relationships for fault zones. J. Struct. Geol., 12: 1061-1065.

Evans, J. P. and Chester, F. M., 1995. Fluid-rock interaction in faults of the San Andreas system: Inference from San Gabriel fault-rock geochemistry and microstructures. J. Geophys. Res., 100: 13,007-13,020.

Feng, R. and McEvilly, T.V., 1983. Interpretation of seismic reflection profiling data for the structure of the San Andreas fault zone. Bull. Seis. Soc. Am., 73: 1701-1720.

Goddard, J. and Evans, J. P., 1995. Chemical changes and fluid-rock interaction in faults of crystalline thrust sheets, northwestern Wyoming, U.S.A. J. Struct. Geol., 17: 533-547.

Grant, J. A., 1986. The isocon diagram--A simple solution to Gresens' equation for metasomatic alteration. Econ. Geol., 81: 1976-1982.

Haxel, G. B., Budahn, J. R., Fries, T. L., King, B. W., Taggart, J. E. and White, L. D., 1986. Protolith geochemistry of the Orocopia and Pelona schists, southern California. Geol Soc Amer Abst., 18: 115.

Haxel, G. B., Budahn, J. R., Fries, T. L., King, B. W., White, L. D. and Aruscavage, P. J., 1987. Geochemistry of the Orocopia schist, southeastern California: summary. In: W. R. Dickinson and M.A. Klute (Editors), Mesoscopic Rocks of Southern Arizona and Adjacent Areas, Ariz. Geol. Soc. Dig. 18: 49-64.

Heaton, T. H., 1990. Evidence for and implication of self-healing pulses of slip in earthquake rupture. Phys Earth Plan. Int., 64: 1-20.

Henyey, T. L. and Wasserburg, G. J., 1971. Heat flow near major strike-slip faults in California. J. Geophys. Res., 76: 7924-7946.

Hickman, S. H., 1991. Stress in the lithosphere and the strength of active faults. Contr. Tectonophysics, Rev. Geophys., 29: 759-775.

Higgs, N. G., 1981. Mechanical properties of ultrafine quartz, chlorite, and bentonite in environments appropriate to upper-crustal earthquakes. PhD Dissertation, Texas A&M University, College Station.

Hippler, S.J. and Knipe, R.J., 1989. The evolution of cataclastic fault rocks from a pre existing mylonite. In: R. J. Knipe, and E. H. Rutter (Editors), Deformation Mechanisms, Rheology and Tectonics, Geol. Soc. Spec. Pub., 54, pp. 71-79.

Hoogerduijn-Strating, E. H. and Vissers, R. L M., 1994. Structures in natural serpentinite gouges. J. Struct. Geol., 16: 1205-1215.

Hough, S. E., Ben-Zion, Y. and Leary, P., 1994. Fault-zone waves observed at the southern Joshua Tree earthquake rupture zone. Bull. Seis. Soc. Am., 84: 761-767.

Hull, J., 1988. Thickness-displacement relationships for deformation zones. J. Struct. Geol., 10: 431-435.

Jacobson, C. E., 1980. Deformation and metamorphism of the Pelona Schist beneath the Vincent Thrust, San Gabriel Mountains, California. PhD Dissertation, University of California, Los Angeles.

Jacobson, C. E., Dawson, M. R. and Postlethwaite, C. E., 1988. Structure, metamorphism, and tectonic significance of the Pelona, Orocopia, and Rand Schists, southern California. In: W. G. Ernst (Editor), Metamorphism and Crustal Evolution of the Western United States, Rubey Volume. Prentice-Hall, Englewood Cliffs, NJ, pp. 976-987.

Janecke, S. J. and Evans, J. P., 1988. Feldspar-influenced rock rheologies. Geology, 16: 1064-1067.

Jones, L. M., 1988. Focal mechanisms and the state of stress on the San Andreas Fault in southern California. J. Geophys. Res., 93: 8869-8891.

Kamb, W.B., 1959, Ice petrofabric observations from Blue Glacier, Washington, in relation to theory and experiment. J. Geophys. Res., 64: 1891-1909.

Knipe, R.J., 1989. Deformation mechanisms--recognition from natural tectonites. J. Struct. Geol., 11: 127-146.

Lachenbruch, A. H. and Sass, J. H., 1980. Heat flow and energetics of the San Andreas fault zone. J. Geophys. Res., 85: 6185-6222.

Lachenbruch, A. H. and Sass, J. H., 1988. The stress heat-flow paradox and thermal results from Cajon Pass. Geophys. Res. Lett., 15: 981-984.

Laird, J., 1988. Chlorites-metamorphic petrology. In S. W. Bailey (Editor), Hydrous Phyllosilicates, Min. Soc. Am., Reviews of Mineralogy, 19, pp. 405-454.

Li, Y., Aki, K., Adams, D. and Hasemi, A., 1994. Seismic guided waves trapped in the fault zone of the Landers, California, earthquake of 1992. J. Geophys. Res., 99:11,705-11,722.

Logan, J. M., Higgs, N. G. and Friedman, M., 1981. Laboratory studies on natural

gouge from the U.S. Geological Survey Dry Lake Valley No. 1 well, San Andreas fault zone. In: N. L. Carter, M. Friedman, J. M. Logan, and D. W. Stearns (Editors), Mechanical Behavior of Crustal Rocks, The Handin Volume, Am. Geophys. Un., Monograph 24, pp. 121-134.

Moore, D. E., Lockner, D. A., Summers, R. and Byerlee, J., 1996. Can crysotile-rich serpentinite gouge explain a weak San Andreas fault? Geol. Soc. Am. Abstr., 28: 93.

Morton, D. M. and Baird, A. K., 1975. Tectonic setting of the San Gabriel Mountains. Calf. Div. Mines Geol. Bull., 196: 3-6.

Mount, S. and Suppe, J., 1987. State of stress near the San Andreas fault: implications for wrench tectonics. Geology, 15: 1143-1146.

Noble, L. F., 1954. The San Andreas fault zone from Soledad Pass to Cajon Pass, California. In: R. H. Jahns (Editor) Geology of Southern California, Calf. Dept. Res., Div. Mines Bull., 170, pp. 37-48.

O'Hara, K. 1988. Fluid flow and volume loss during mylonitization: an origin for phyllite in an overthrust setting, North Carolina. Tectonophysics, 156: 21-36.

O'Neil, J. R. and Hanks, T. C., 1980. Geochemical evidence for water-rock interaction along the San Andreas and Garlock faults of California. J. Geophys. Res., 85: 6286-6292.

Petit, J. P., 1987. Criteria for the sense of movement on fault surfaces in brittle rocks. J. Struct. Geol., 9: 597-608.

Powell, R.E. and Weldon II, R.J. Jr., 1992. Evolution of the San Andreas fault. Annual Rev. Earth Plan. Sci., 20: 431-468.

Rice, J. R., 1992. Fault stress states, pore pressure distributions, and the weakness of the San Andreas Fault. In: J.B. Evans and T.F. Wong (Editors), Fault Mechanics and the Transport Properties of Rocks, Academic Press, San Diego, CA, pp. 475-503.

Rutter, E.H., 1983. Pressure solution in nature, theory and experiment. J. Geol. Soc. London, 140: 725-740.

Scholz, C. H., 1987. Wear and gouge formation in brittle faulting. Geology, 15:493-495.

Scholz, C.H., Dawers, N.H., Yu, J.Z., Anders, M.H. and Cowie, P.A., 1993. Fault growth and fault scaling laws: preliminary results. J. Geophys. Res., 98: 21,951-21,961.

Shipton, Z.K. and Cowie, P.A., 1996. Displacement gradients at fault tips: the Chimney

Rock fault array, Utah. Faulting, fault sealing and fluid flow. Hydrocarbon Res.Abstr., University of Leeds, 29-30.

Sibson, R. H., 1977. Fault rocks and fault mechanisms. J. Geol. Soc. London, 133: 191-213.

Sibson, R. H., 1989. Earthquake faulting as a structural process. J. Struct. Geol., 11: 1-14.

Sieh, K. E., 1978. Slip along the San Andreas fault associated with the great 1857 earthquake. Seis. Soc. Am. Bull., 68: 1421-1448.

Sylvester, A. G., 1988. Strike-slip faults. Geol. Soc. Am. Bull., 100: 1666-1703.

Turcotte, D. L., Tag, P. H. and Cooper, R. F., 1980. A steady state model for the distribution of stress and temperature on the San Andreas Fault. J. Geophys. Res., 85: 6224-6230.

Walsh, J.J. and Watterson, J., 1988. Analysis of the relationship between the displacements and dimensions of faults. J. Struct. Geol., 10: 239-247.

Weldon, R. J., 1987. San Andreas fault, Cajon Pass, southern California. In: M. L. Hill (Editor), Centennial Field Guide -- Cordilleran Section, Geol. Soc. Am., Boulder, CO, pp. 193-198.

Wintsch, R. P., Christoffersen, R. and Kronenberg, A. K., 1995. Fluid-rock reaction weakening in fault zones. J. Geophys. Res., 100: 13,021-13,032.

XRAL Laboratories, 1996. Whole rock analysis: the dilemma of SUMS based on oxides. February Newsletter: 4 pp.

Yund, R. A., Blanpied, M. L., Tullis, T. E. and Weeks, J. D., 1990. Amorphous material in high strain experimental fault gouges. J. Geophys. Res., 95: 15,589 15,602.

Zoback, M. D., Zoback, M. L., Mount, S., Suppe, J., Eaton, J. P., Healy, J. H., Oppenhiemer, D., Reasenberg, P., Jones, L., Raleigh, C. B., Wong, I. G., Scotti, O. and Wentworth, C., 1987. New evidence on the state of stress of the San Andreas Fault System, Science, 238: 1105-1111.

Zoback, M.D. and Hickman, S., 1996. San Andreas fault zone drilling project: Scientific rationale and proposal for a pilot project at Parkfield, CA. Nat. Sci. Found. Report, June 1: 86 pp.

Zoback, M. D., Tsukahara, H. and Hickman, S., 1980. Stress measurements at depth in the vicinity of the San Andreas Fault: implications for magnitude of shear stress at depth. J. Geophys. Res., 85: 6157-6173.

APPENDICES

Appendix A

Stereograms

Stereograms

Figures A.1 through A.29 are equal area, lower hemispheric stereographic projections of fracture and slip surface orientations. These stereograms are enlarged versions of the stereograms shown in Figures 21 through 26.

The stereograms were constructed with Stereonet 4.6a (Allmendinger, 1988). In part (a), the poles to the planes of each structure (fracture or slip surface) is plotted. In (b), the density of the poles is contoured using the Kamb method (Kamb, 1959). The contour interval is 2.0 sigma and the significance level is 3.0 sigma. The statistics in part (c) were calculated using Stereonet 4.6a (Allmendinger, 1988). The number of objects plotted in each stereogram is given by the value N. The Bingham Axial Distribution of each stereogram was determined to provide the three eigenvectors and eigenvalues of the data.

a) b)

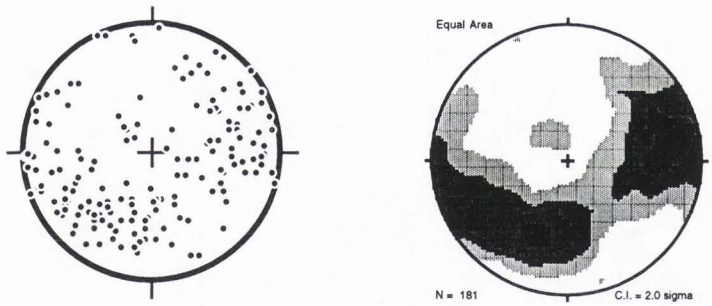

c) N= 181

	Eigenvalues	Eigenvectors
1.	0.4604	239°, 12°
2.	0.3731	131°, 54°
3.	0.1665	337°, 33°

Figure A.1 Lower hemispheric stereographic projections which show the orientations of fractures at traverse 1, group a. This is an enlargement of the stereogram shown in Figure 21a. a) Plot of the poles to the planes. b) Kamb contour of the poles. Contour interval is 2.0 sigma with a significance level of 3.0 sigma. c) Statistical data.

a) b)

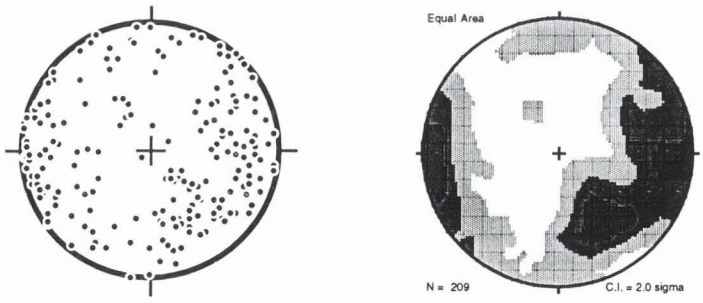

c) N= 209

	Eigenvalues	Eigenvectors
1.	0.4766	097°, 19°
2.	0.3220	195°, 23°
3.	0.2014	332°, 60°

Figure A.2 Lower hemispheric stereographic projections which show the orientations of fractures at traverse 1, group b. This is an enlargement of the stereogram shown in Figure 21b. a) Plot of the poles to the planes. b) Kamb contour of the poles. Contour interval is 2.0 sigma with a significance level of 3.0 sigma. c) Statistical data.

a) b)

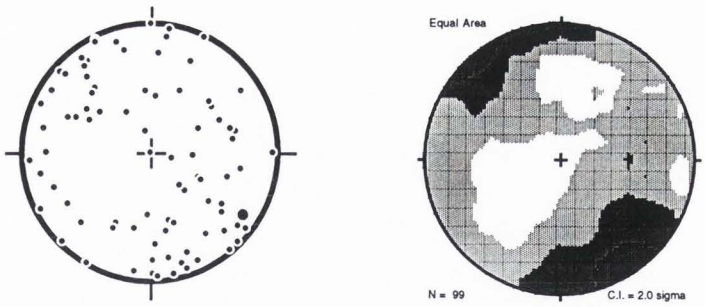

c) N= 99

	Eigenvalues	Eigenvectors
1.	0.4771	147°,09°
2.	0.2941	053°,23°
3.	0.2288	258°,65°

Figure A.3 Lower hemispheric stereographic projections which show the orientations of fractures at traverse 1, group c. This is an enlargement of the stereogram shown in Figure 21c. a) Plot of the poles to the planes. b) Kamb contour of the poles. Contour interval is 2.0 sigma with a significance level of 3.0 sigma. c) Statistical data.

a) b)

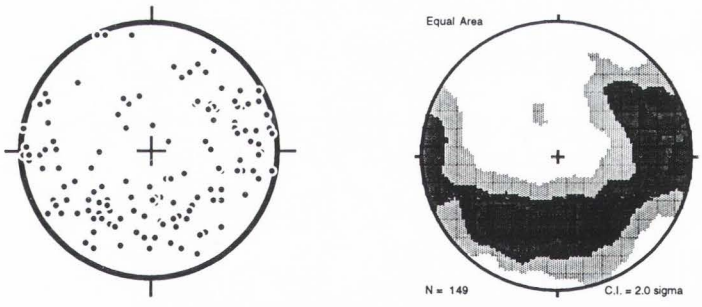

c) N= 149

	Eigenvalues	Eigenvectors
1.	0.4292	081°, 14°
2.	0.3993	187°, 47°
3.	0.1716	339°, 40°

Figure A.4 Lower hemispheric stereographic projections which show the orientations of fractures at traverse 1, group d. This is an enlargement of the stereogram shown in Figure 21d. a) Plot of the poles to the planes. b) Kamb contour of the poles. Contour interval is 2.0 sigma with a significance level of 3.0 sigma. c) Statistical data.

a) b)

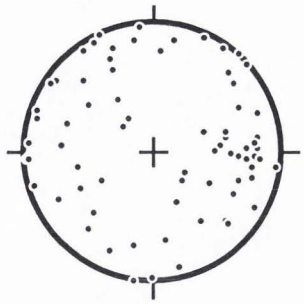

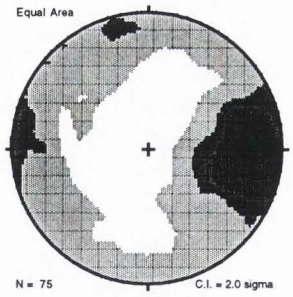

c) N= 75

	Eigenvalues	Eigenvectors
1.	0.4931	099°, 16°
2.	0.2991	008°, 04°
3.	0.2079	263°, 74°

Figure A.5 Lower hemispheric stereographic projections which show the orientations of fractures at traverse 1, group e. This is an enlargement of the stereogram shown in Figure 21e. a) Plot of the poles to the planes. b) Kamb contour of the poles. Contour interval is 2.0 sigma with a significance level of 3.0 sigma. c) Statistical data.

a) b)

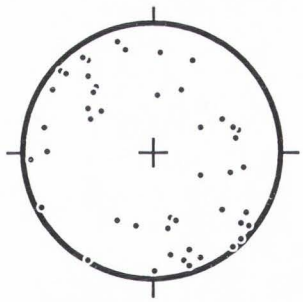

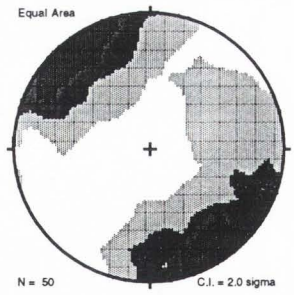

c) N= 50

	Eigenvalues	Eigenvectors
1.	0.5467	141°, 03°
2.	0.2675	049°, 36°
3.	0.1857	234°, 54°

Figure A.6. Lower hemispheric stereographic projections which show the orientations of fractures at traverse 1, group f. This is an enlargement of the stereogram shown in Figure 21f. a) Plot of the poles to the planes. b) Kamb contour of the poles. Contour interval is 2.0 sigma with a significance level of 3.0 sigma. c) Statistical data.

a) b)

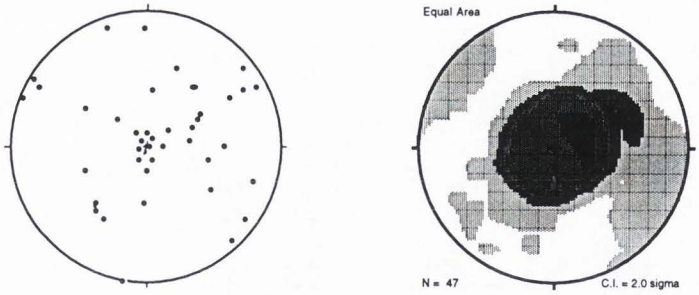

c) N= 47

	Eigenvalues	Eigenvectors
1.	0.5408	073°, 80°
2.	0.2544	274°, 09°
3.	0.2049	184°, 03°

Figure A.7 Lower hemispheric stereographic projections which show the orientations of fractures at traverse 2, group a. This is an enlargement of the stereogram shown in Figure 22a. a) Plot of the poles to the planes. b) Kamb contour of the poles. Contour interval is 2.0 sigma with a significance level of 3.0 sigma. c) Statistical data.

a) b)

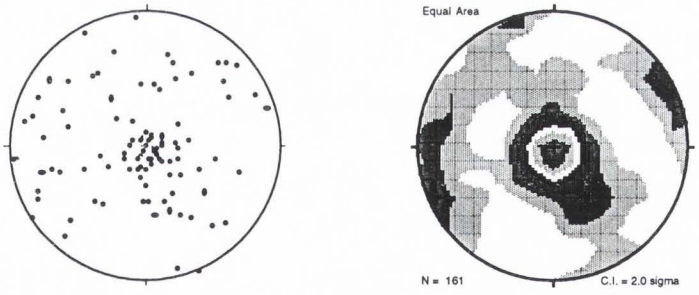

c) N= 161

	Eigenvalues	Eigenvectors
1.	0.4897	197°, 84°
2.	0.2930	097°, 01°
3.	0.2173	007°, 06°

Figure A.8 Lower hemispheric stereographic projections which show the orientations of fractures at traverse 2, group b. This is an enlargement of the stereogram shown in Figure 22b. a) Plot of the poles to the planes. b) Kamb contour of the poles. Contour interval is 2.0 sigma with a significance level of 3.0 sigma. c) Statistical data.

a) b)

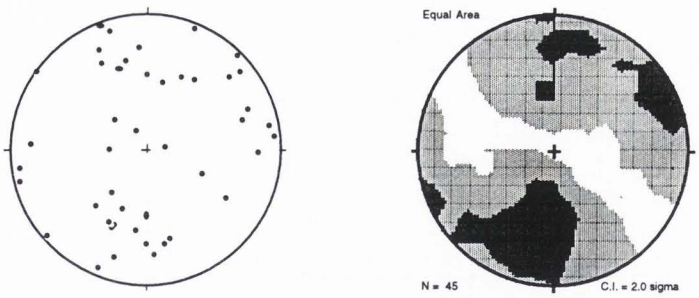

c) N= 45

	Eigenvalues	Eigenvectors
1.	0.4407	203°, 07°
2.	0.2924	083°, 76°
3.	0.2669	295°, 12°

Figure A.9 Lower hemispheric stereographic projections which show the orientations of fractures at traverse 2, group c. This is an enlargement of the stereogram shown in Figure 22c. a) Plot of the poles to the planes. b) Kamb contour of the poles. Contour interval is 2.0 sigma with a significance level of 3.0 sigma. c) Statistical data.

a) b)

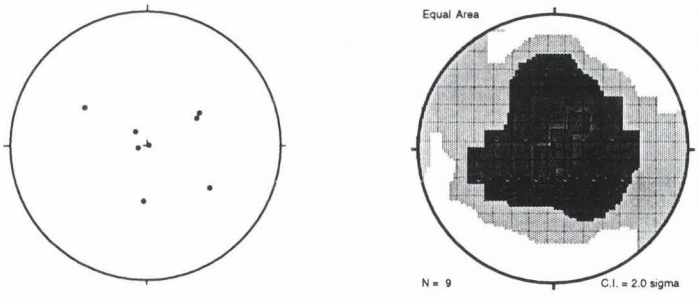

c) N= 9

	Eigenvalues	Eigenvectors
1.	0.7147	031°, 86°
2.	0.2010	292°, 01°
3.	0.0842	202°, 04°

Figure A.10 Lower hemispheric stereographic projections which show the orientations of fractures at traverse 2, group d. This is an enlargement of the stereogram shown in Figure 22d. a) Plot of the poles to the planes. b) Kamb contour of the poles. Contour interval is 2.0 sigma with a significance level of 3.0 sigma. c) Statistical data.

a) b)

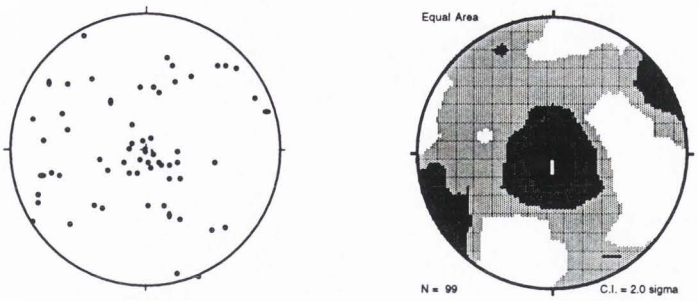

c) N= 99

	Eigenvalues	Eigenvectors
1.	0.4647	263°, 74°
2.	0.2890	060°, 15°
3.	0.2463	152°, 06°

Figure A.11 Lower hemispheric stereographic projections which show the orientations of fractures at traverse 2, group e. This is an enlargement of the stereogram shown in Figure 22e. a) Plot of the poles to the planes. b) Kamb contour of the poles. Contour interval is 2.0 sigma with a significance level of 3.0 sigma. c) Statistical data.

a) b)

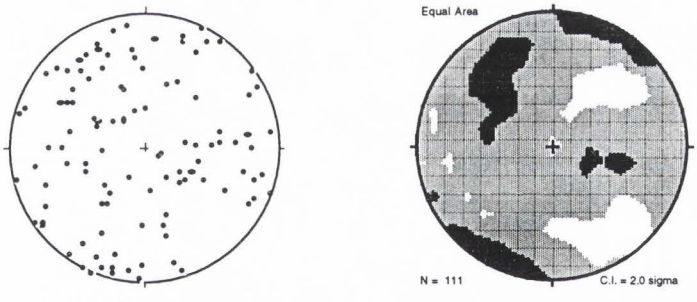

c) N= 111

	Eigenvalues	Eigenvectors
1.	0.3654	005°, 19°
2.	0.3470	261°, 36°
3.	0.2877	117°, 48°

Figure A.12 Lower hemispheric stereographic projections which show the orientations of fractures at traverse 2, group f. This is an enlargement of the stereogram shown in Figure 22f. a) Plot of the poles to the planes. b) Kamb contour of the poles. Contour interval is 2.0 sigma with a significance level of 3.0 sigma. c) Statistical data.

a) b)

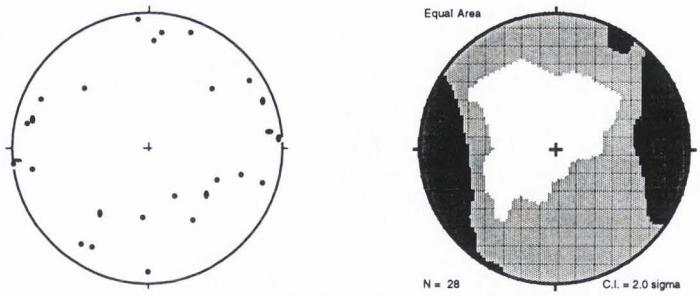

c) N= 28

	Eigenvalues	Eigenvectors
1.	0.5133	081°, 04°
2.	0.3370	173°, 15°
3.	0.1497	335°, 75°

Figure A.13 Lower hemispheric stereographic projections which show the orientations of fractures at traverse 2, group g. This is an enlargement of the stereogram shown in Figure 22g. a) Plot of the poles to the planes. b) Kamb contour of the poles. Contour interval is 2.0 sigma with a significance level of 3.0 sigma. c) Statistical data.

a) b)

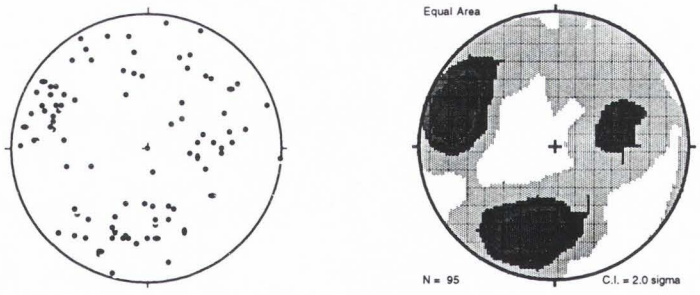

c) N= 95

	Eigenvalues	Eigenvectors
1.	0.3661	219°, 26°
2.	0.3445	310°, 02°
3.	0.2894	045°, 64°

Figure A.14 Lower hemispheric stereographic projections which show the orientations of fractures at traverse 3, group a. This is an enlargement of the stereogram shown in Figure 23a. a) Plot of the poles to the planes. b) Kamb contour of the poles. Contour interval is 2.0 sigma with a significance level of 3.0 sigma. c) Statistical data.

a) b)

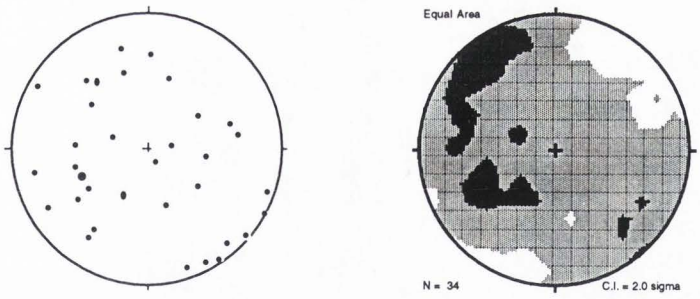

c) N= 34

	Eigenvalues	Eigenvectors
1.	0.4206	296°, 40°
2.	0.3359	149°, 46°
3.	0.2435	040°, 17°

Figure A.15 Lower hemispheric stereographic projections which show the orientations of fractures at traverse 3, group b. This is an enlargement of the stereogram shown in Figure 23b. a) Plot of the poles to the planes. b) Kamb contour of the poles. Contour interval is 2.0 sigma with a significance level of 3.0 sigma. c) Statistical data.

a) b)

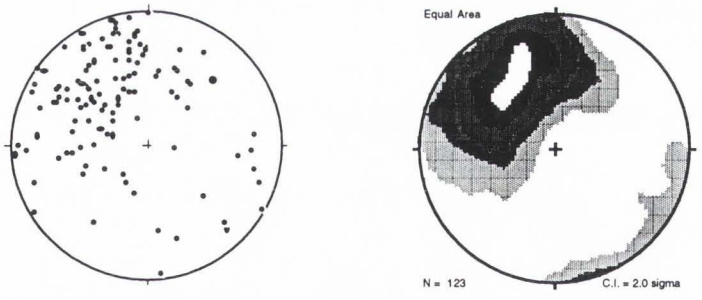

c) N= 123

	Eigenvalues	Eigenvectors
1.	0.6260	323°, 37°
2.	0.2059	233°, 01°
3.	0.1680	142°, 53°

Figure A.16 Lower hemispheric stereographic projections which show the orientations of slip surfaces at traverse 1, group a. This is an enlargement of the stereogram shown in Figure 24a. a) Plot of the poles to the planes. b) Kamb contour of the poles. Contour interval is 2.0 sigma with a significance level of 3.0 sigma. c) Statistical data.

a) b)

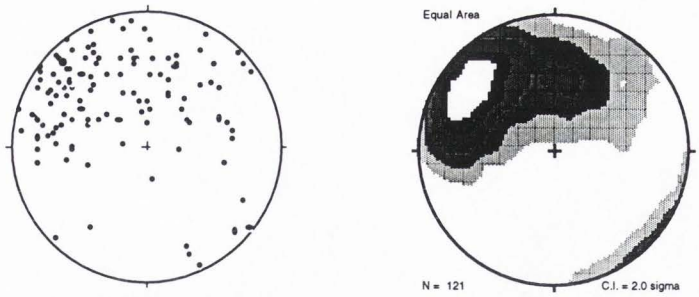

c) N= 121

	Eigenvalues	Eigenvectors
1.	0.6016	319°, 34°
2.	0.2663	066°, 24°
3.	0.1320	184°, 47°

Figure A.17 Lower hemispheric stereographic projections which show the orientations of slip surfaces at traverse 1, group b. This is an enlargement of the stereogram shown in Figure 24b. a) Plot of the poles to the planes. b) Kamb contour of the poles. Contour interval is 2.0 sigma with a significance level of 3.0 sigma. c) Statistical data.

a) b)

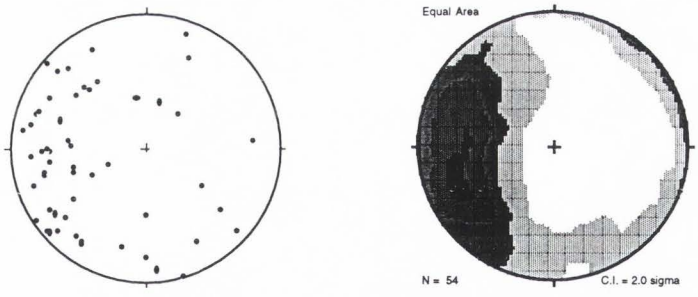

c) N= 54

	Eigenvalues	Eigenvectors
1.	0.5549	265°, 28°
2.	0.3031	355°, 01°
3.	0.1420	086°, 63°

Figure A.18 Lower hemispheric stereographic projections which show the orientations of slip surfaces at traverse 1, group c. This is an enlargement of the stereogram shown in Figure 24c. a) Plot of the poles to the planes. b) Kamb contour of the poles. Contour interval is 2.0 sigma with a significance level of 3.0 sigma. c) Statistical data.

a) b)

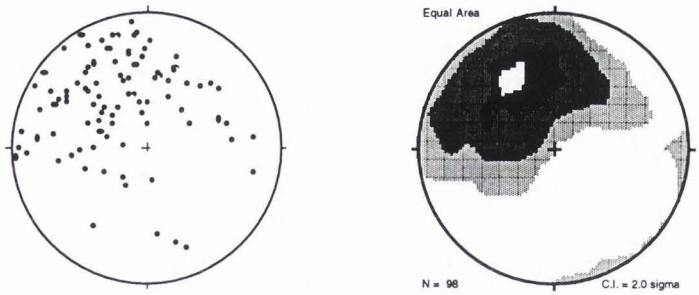

c) N= 98

	Eigenvalues	Eigenvectors
1.	0.6280	327°, 44°
2.	0.2164	070°, 13°
3.	0.1556	172°, 43°

Figure A.19 Lower hemispheric stereographic projections which show the orientations of slip surfaces at traverse 1, group d. This is an enlargement of the stereogram shown in Figure 24d. a) Plot of the poles to the planes. b) Kamb contour of the poles. Contour interval is 2.0 sigma with a significance level of 3.0 sigma. c) Statistical data.

a) b)

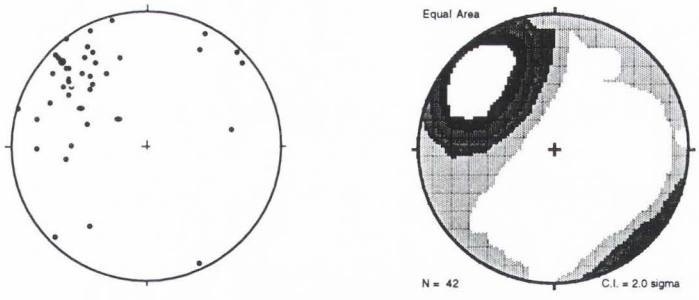

c) N= 42

	Eigenvalues	Eigenvectors
1.	0.7061	312°, 26°
2.	0.2176	220°, 04°
3.	0.0763	123°, 64°

Figure A.20 Lower hemispheric stereographic projections which show the orientations of slip surfaces at traverse 1, group e. This is an enlargement of the stereogram shown in Figure 24e. a) Plot of the poles to the planes. b) Kamb contour of the poles. Contour interval is 2.0 sigma with a significance level of 3.0 sigma. c) Statistical data.

a) b)

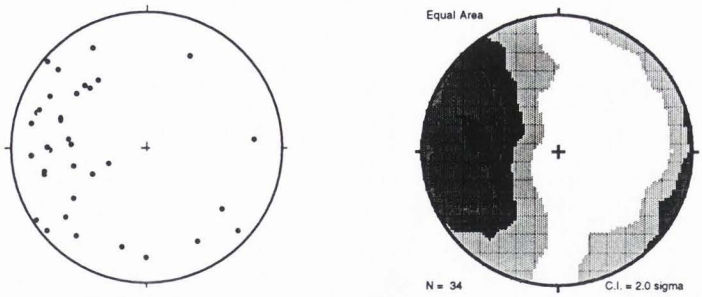

c) N= 34

	Eigenvalues	Eigenvectors
1.	0.6242	278°, 27°
2.	0.2686	182°, 12°
3.	0.1072	071°, 60°

Figure A.21 Lower hemispheric stereographic projections which show the orientations of slip surfaces at traverse 1, group f. This is an enlargement of the stereogram shown in Figure 24f. a) Plot of the poles to the planes. b) Kamb contour of the poles. Contour interval is 2.0 sigma with a significance level of 3.0 sigma. c) Statistical data.

a) b)

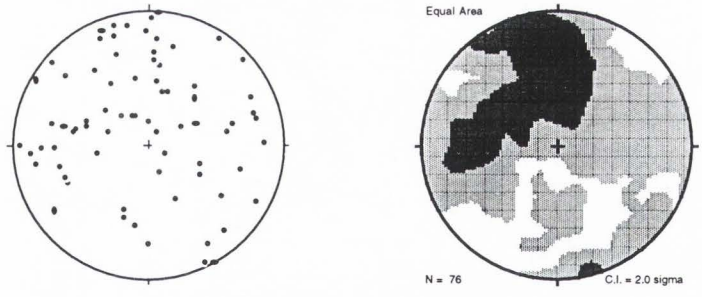

c) N= 76

	Eigenvalues	Eigenvectors
1.	0.4426	333°, 47°
2.	0.2928	082°, 17°
3.	0.2646	186°, 38°

Figure A.22 Lower hemispheric stereographic projections which show the orientations of slip surfaces at traverse 2, group a. This is an enlargement of the stereogram shown in Figure 25a. a) Plot of the poles to the planes. b) Kamb contour of the poles. Contour interval is 2.0 sigma with a significance level of 3.0 sigma. c) Statistical data.

a) b)

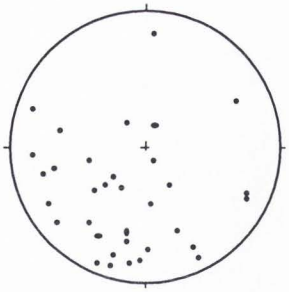

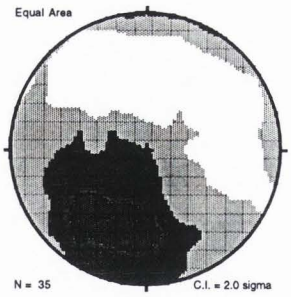

c) N= 35

	Eigenvalues	Eigenvectors
1.	0.5661	206°, 41°
2.	0.2453	302°, 07°
3.	0.1887	039°, 48°

Figure A.23 Lower hemispheric stereographic projections which show the orientations of slip surfaces at traverse 2, group b. This is an enlargement of the stereogram shown in Figure 25b. a) Plot of the poles to the planes. b) Kamb contour of the poles. Contour interval is 2.0 sigma with a significance level of 3.0 sigma. c) Statistical data.

a) b)

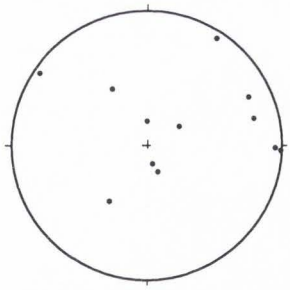

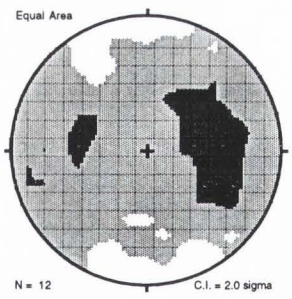

c) N= 12

	Eigenvalues	Eigenvectors
1.	0.4715	076°, 45°
2.	0.3661	264°, 45°
3.	0.1624	170°, 04°

Figure A.24 Lower hemispheric stereographic projections which show the orientations of slip surfaces at traverse 2, group c. This is an enlargement of the stereogram shown in Figure 25c. a) Plot of the poles to the planes. b) Kamb contour of the poles. Contour interval is 2.0 sigma with a significance level of 3.0 sigma. c) Statistical data.

a) b)

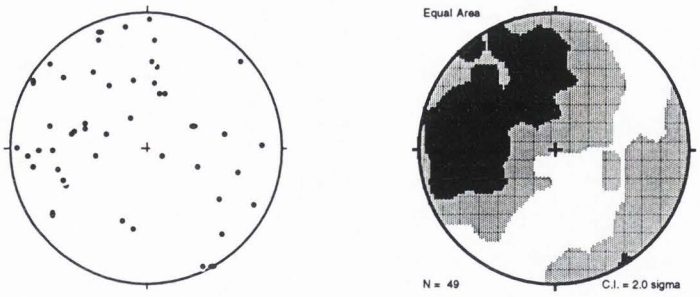

c) N= 49

	Eigenvalues	Eigenvectors
1.	0.4807	305°, 37°
2.	0.2755	049°, 18°
3.	0.2438	160°, 48°

Figure A.25 Lower hemispheric stereographic projections which show the orientations of slip surfaces at traverse 2, group d. This is an enlargement of the stereogram shown in Figure 25d. a) Plot of the poles to the planes. b) Kamb contour of the poles. Contour interval is 2.0 sigma with a significance level of 3.0 sigma. c) Statistical data.

a) b)

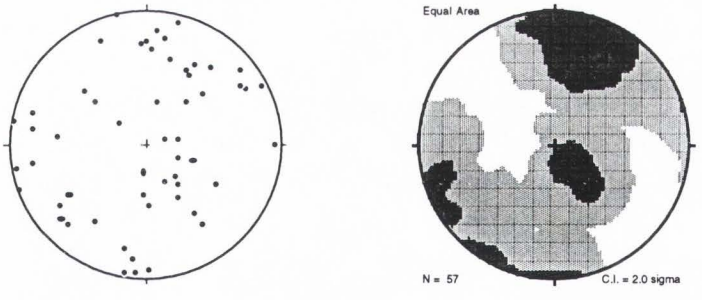

c) N= 57

	Eigenvalues	Eigenvectors
1.	0.4346	031°, 14°
2.	0.3201	166°, 70°
3.	0.2453	297°, 14°

Figure A.26 Lower hemispheric stereographic projections which show the orientations of slip surfaces at traverse 2, group e. This is an enlargement of the stereogram shown in Figure 25e. a) Plot of the poles to the planes. b) Kamb contour of the poles. Contour interval is 2.0 sigma with a significance level of 3.0 sigma. c) Statistical data.

a) b)

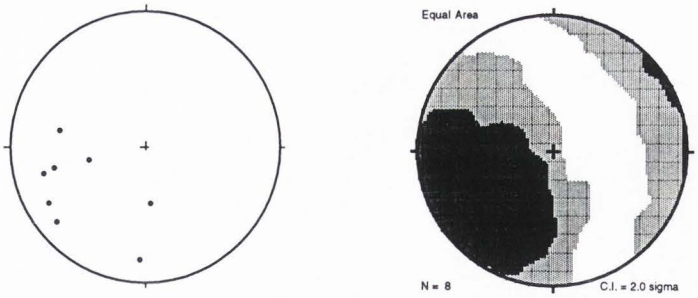

c) N= 8

	Eigenvalues	Eigenvectors
1.	0.7464	241°, 34°
2.	0.1749	145°, 08°
3.	0.0792	044°, 54°

Figure A.27 Lower hemispheric stereographic projections which show the orientations of slip surfaces at traverse 2, group f. This is an enlargement of the stereogram shown in Figure 25f. a) Plot of the poles to the planes. b) Kamb contour of the poles. Contour interval is 2.0 sigma with a significance level of 3.0 sigma. c) Statistical data.

a) b)

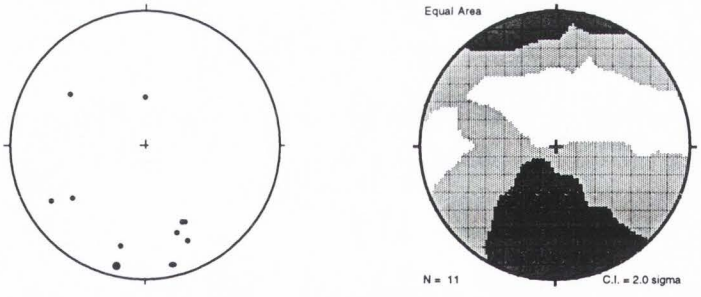

c) N= 11

	Eigenvalues	Eigenvectors
1.	0.6353	177°, 25°
2.	0.2367	285°, 33°
3.	0.1280	057°, 46°

Figure A.28 Lower hemispheric stereographic projections which show the orientations of slip surfaces at traverse 3, group a. This is an enlargement of the stereogram shown in Figure 26a. a) Plot of the poles to the planes. b) Kamb contour of the poles. Contour interval is 2.0 sigma with a significance level of 3.0 sigma. c) Statistical data.

a) b)

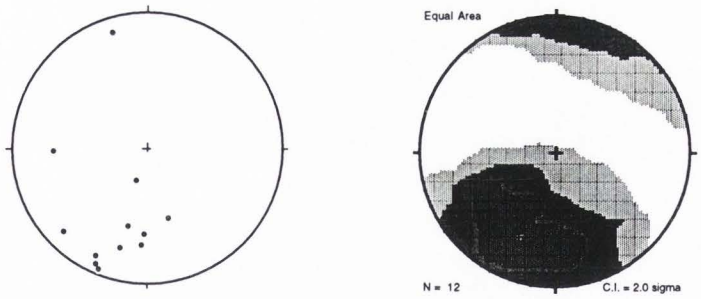

c) N= 12

	Eigenvalues	Eigenvectors
1.	0.7600	197°, 27°
2.	0.1373	309°, 36°
3.	0.1027	080°, 42°

Figure A.29 Lower hemispheric stereographic projections which show the orientations of slip surfaces at traverse 3, group b. This is an enlargement of the stereogram shown in Figure 26b. a) Plot of the poles to the planes. b) Kamb contour of the poles. Contour interval is 2.0 sigma with a significance level of 3.0 sigma. c) Statistical data.

Appendix B

Geochemical Analysis

Table B1
Geochemical results of oxide analysis[1] of rocks from traverse 1.

Sample number	Dist. from Flt. (m)[2]	Rock Type[3]	SiO_2	Al_2O_3	CaO	MgO	Na_2O	K_2O	Fe_2O_3	MnO	TiO_2	P_2O_5	Cr_2O_3	LOI	SUM
5.40	-7	A-MG	59.2	15.2	5.72	2.12	2.75	2.60	6.92	0.09	0.769	0.27	<.01	3.00	98.6
5.39	-6	A-MG	56.0	15.3	4.66	2.43	2.46	3.34	9.43	0.11	1.100	0.29	<.01	3.40	98.5
5.38	-5	A-MG	59.8	13.9	4.98	2.09	2.23	2.93	8.16	0.09	0.843	0.21	<.01	3.00	98.2
5.36	-3	A-MG	62.2	21.0	3.04	0.33	8.58	1.13	0.60	<.01	0.085	0.02	<.01	1.25	98.2
5.35	-2	A-MG	52.3	15.9	3.29	4.01	1.16	6.17	9.76	0.10	1.240	0.31	<.01	4.60	98.8
5.34	-1	A-MG	63.8	14.6	4.15	1.50	3.02	3.49	4.51	0.04	0.590	0.19	<.01	2.25	98.1
5.B1	0	C-MB	39.6	16.5	6.89	9.07	1.34	1.38	16.30	0.17	1.190	0.18	0.02	7.00	99.6
5.B2	0	C-MB	41.8	16.8	8.17	7.50	1.36	0.50	14.40	0.18	1.130	0.21	<.01	7.80	99.9
5.21	6	A-MB	42.0	17.9	8.99	6.38	2.21	1.37	14.20	0.13	1.300	0.70	<.01	3.50	98.7
5.28	20	P-MB	41.3	16.6	9.69	7.21	1.55	0.71	15.90	0.16	1.250	0.27	<.01	4.10	98.7
5.29	30	P-MB	45.6	16.5	8.42	5.96	2.79	1.04	13.50	0.17	0.946	0.52	<.01	2.75	98.2

1 Geochemical results are from x-ray defraction analysis and are expressed in weight percent with a detection limit of 0.01.
2 Distance in measured from the north branch of the Punchbowl fault. Distances increase northward.
3 Rock Type: Pr - Protolith, has a recognizable fabric; A - Altered, with little recognizable primary fabric; C - Cataclasite; MB - Metabasalt; MG - Metagraywacke; AP - Aplite

Table B2
Geochamical results of analysis[1] for rare-earth minerals, carbon and sulfer from traverse 1

Sample number	Dist. from Flt. (m)[2]	Rock Type[3]	C	S	Rb	Sr	Y	Zr	Nb	Ba
5.40	-7	A-MG	0.06	0.02	56	317	21	167	<10	872
5.39	-6	A-MG	0.04	0.01	67	339	37	271	14	1150
5.38	-5	A-MG	0.08	0.04	81	244	30	178	12	819
5.36	-3	A-MG	0.16	0.02	26	598	<10	20	<10	324
5.35	-2	A-MG	0.05	0.02	138	353	37	234	15	2060
5.34	-1	A-MG	0.06	0.02	137	648	73	416	18	1600
5.B1	0	C-MB	0.06	0.03	23	500	15	73	<10	636
5.B2	0	C-MB	0.06	0.02	<10	442	11	61	<10	268
5.21	6	A-MB	0.06	0.02	22	612	17	60	<10	495
5.28	20	P-MB	0.05	0.01	90	247	25	49	<10	1210
5.29	30	P-MB	0.03	0.02	<10	521	16	56	<10	538

1 Rare earth minerals results are from LECO analysis and are expressed in PPM with a detection limit of 1.0.
2 Distance in measured from the north branch of the Punchbowl fault. Distances increase northward.
3 Rock Type: Pr - Protolith, has a recognizable fabric; A - Altered, with little recognizable primary fabric; C - Cataclasite; MB - Metabasalt; MG - Metagraywacke; AP - Aplite

Table B3
Geochemical results of oxide analysis[1] of rocks from traverse 2.

Sample number	Dist. from Flt. (m)[2]	Rock Type[3]	SiO_2	Al_2O_3	CaO	MgO	Na_2O	K_2O	Fe_2O_3	MnO	TiO_2	P_2O_5	Cr_2O_3	LOI	SUM
14.01	-36	A-AP	71.10	14.00	1.42	0.38	2.97	5.77	1.53	0.02	0.168	0.04	<.01	1.00	98.4
14.02	-38	A-AP	73.90	12.90	1.01	0.34	2.87	5.04	1.37	0.02	0.139	0.05	<.01	0.80	98.4
14.03	-9	A-AP	73.10	13.20	0.88	0.35	2.99	5.41	1.06	0.02	0.117	0.03	<.01	0.95	98.1
14.04	-14	A-AP	71.20	13.20	1.91	0.32	2.84	5.46	1.43	0.02	0.150	0.04	<.01	1.85	98.4
14.05	-24	A-AP	72.90	13.20	0.93	0.34	2.74	5.67	1.64	0.02	0.160	0.06	<.01	0.70	98.4
14.06	-3	A-AP	40.40	16.10	9.49	8.55	1.49	0.78	15.60	0.19	1.380	0.42	<.01	3.80	98.2
14.07	-5	A-AP	35.80	12.80	16.10	5.70	1.45	1.32	10.80	0.20	0.956	0.28	<.01	14.70	100.1
14.08	-31	A-AP	73.10	14.10	0.57	0.36	3.15	5.81	1.35	0.03	0.140	0.05	<.01	0.75	99.4
14.09	4	A-MG	53.20	17.30	3.08	3.36	2.79	2.96	7.50	0.12	1.100	0.34	<.01	3.40	95.2
14.10	11	A-MG	56.90	13.80	7.78	2.62	2.87	2.32	5.05	0.08	0.750	0.19	<.01	7.05	99.4
14.12	37	P -MG	64.20	13.80	4.33	2.38	2.56	2.30	5.67	0.09	0.766	0.19	<.01	3.25	99.5
14.13	46	P -MB	46.70	12.70	9.40	9.45	2.31	0.24	13.40	0.16	1.400	0.15	0.02	2.35	98.3
14.14	43	P -MB	39.60	14.70	5.95	9.97	2.05	0.13	17.80	0.36	2.580	0.42	<.01	4.95	98.5
14.15	60	P -MB	42.10	11.90	14.10	5.80	2.83	0.26	12.30	0.15	2.530	0.57	<.01	6.15	98.7
14.16	70	P -MB	45.80	12.60	10.80	8.51	2.14	0.56	12.90	0.13	2.080	0.17	0.01	2.65	98.4
14.17	101	P -MG	68.50	13.00	3.53	1.91	3.73	1.30	4.07	0.05	0.491	0.08	<.01	1.70	98.4
14.18	133	P -MG	61.60	15.90	2.95	2.55	2.92	2.35	6.61	0.13	0.733	0.38	<.01	2.25	98.4
14.19	-133	C-MG	58.60	15.00	6.11	2.54	3.17	1.24	7.56	0.13	0.956	0.43	<.01	2.55	98.3
14.20	-127	A-MG	56.00	14.10	5.31	3.99	1.91	2.20	9.50	0.14	0.939	0.17	0.02	4.75	99.0
14.21	-124	A-MG	57.80	13.70	4.59	5.28	1.96	1.49	9.60	0.12	0.936	0.16	<.01	3.20	98.8
14.22	-121	A -MG	62.20	13.30	1.49	3.83	2.11	2.26	9.56	0.16	0.831	0.04	<.01	2.95	98.7
14.23	-113	A -MG	64.80	13.00	4.39	2.62	3.24	1.24	5.78	0.08	0.547	0.15	<.01	2.95	98.8
14.24	-110	A-MB	48.10	11.60	9.62	9.75	1.93	0.75	12.80	0.21	0.838	0.14	0.05	1.95	97.7
14.25	-89	A-MB	55.40	13.70	1.22	8.89	1.14	2.64	10.00	0.07	0.684	0.08	<.01	5.20	99.0
14.26	-79	A -MG	72.50	15.70	2.11	0.25	4.87	1.74	0.52	<0.01	0.035	<.01	<.01	0.80	98.5
14.27	-68	A-MG	78.60	13.00	2.12	0.08	4.35	0.68	0.05	<.01	<.001	<.01	<.01	0.35	99.2
14.28	-60	A-MB	49.00	16.30	8.67	5.93	1.83	2.05	10.40	0.16	1.470	0.37	<.01	2.05	98.2
14.29	-53	A-MG	61.80	14.70	3.43	2.96	2.75	2.58	6.89	0.12	0.747	0.06	<.01	2.60	98.6
14.30	-47	A-MG	54.80	16.00	7.26	3.36	2.68	1.64	8.60	0.13	1.050	0.41	<.01	2.60	98.5
14.31	-135	A -MG	70.90	5.95	3.08	2.54	0.10	0.53	8.96	1.16	0.336	0.77	<.01	4.60	98.9
14.32	-137	A-MG	61.40	16.00	3.03	1.97	2.49	3.41	5.34	0.05	0.672	0.21	<.01	4.35	98.9
14.33	-160	P -MG	58.00	12.20	3.98	8.54	2.31	1.75	8.78	0.19	0.740	0.22	0.05	1.45	98.2
14.34	-192	P -MG	67.20	14.80	2.08	1.52	3.66	2.38	4.06	0.05	0.543	0.18	<.01	1.50	98.0
14.35	-250	P -MG	63.80	15.60	2.72	1.98	2.79	3.58	5.15	0.06	0.638	0.26	<.01	1.85	98.4

[1] Geochemical results are from x-ray defraction analysis and are expressed in weight percent with a detection limit of 0.01.
[2] Distance in measured from the north branch of the Punchbowl fault. Distances increase northward.
[3] Rock Type: Pr - Protolith, has a recognizable fabric; A - Altered, with little recognizable primary fabric; C - Cataclasite; MB - Metabasalt; MG - Metagraywacke; AP - Aplite